Doctoral Dissertation

Design of Novel Fluoroanions Aiming at Systematical Functionalization for Ionic Liquids

Kazuki Iwasaki

January 2018

Department of Applied Chemistry

Graduate School of Engineering

Osaka University

Design of Novel Fluoroanions Aiming at Systematical Functionalization for Ionic Liquids

（イオン液体の系統的機能化を目指した新規フッ化物アニオンの設計）

Kazuki Iwasaki

岩﨑 和紀

January 2018

Department of Applied Chemistry

Graduate School of Engineering

Osaka University

Preface

The work of this thesis has been performed during 2013–2018 under the guidance of Professor Susumu Kuwabata at Department of Applied Chemistry, Graduate School of Engineering, Osaka University.

The objective in this thesis is to reveal the structural and electronic effects of anionic structure on the physicochemical properties of alkali metal salts and room temperature ionic liquids. Employing aryltrifluoroborate anions which can be systematically modified the structures, the author found the crucial factors, information for design of salts based on materials informatics, involved in the property expression of salts and ionic liquids.

The author wishes that the findings obtained in this work will provide valuable information to further development and progress of science and technology in the field of ionic liquid.

Kazuki Iwasaki

Department of Applied Chemistry
Graduate School of Engineering
Osaka University
2-1 Yamada-oka, Suita,
Osaka 565-0871, Japan

List of Publications

1. Alkali Metal Salts with Designable Aryltrifluoroborate Anions
   Kazuki Iwasaki, Kazuki Yoshii, Seiji Tsuzuki, Hajime Matsumoto, Tetsuya Tsuda, and Susumu Kuwabata
   The Journal of Physical Chemistry B, **2016**, *120*, 9468–9476.
2. Physicochemical Properties of Phenyltrifluoroborate-Based Room Temperature Ionic Liquids
   Kazuki Iwasaki, Kazuki Yoshii, Tetsuya Tsuda, and Susumu Kuwabata
   Journal of Molecular Liquids, **2017**, *246*, 236–243.
3. Physicochemical Properties and Electrochemical Behavior of Systematically Functionalized Aryltrifluoroborate-Based Room-Temperature Ionic Liquids
   Kazuki Iwasaki, Seiji Tsuzuki, Tetsuya Tsuda, and Susumu Kuwabata
   The Journal of Physical Chemistry C, in press
4. Aryltrifluoroborate-Based Ionic Liquids Used as Specific Electrolyte for Electric Double Layer Capacitor
   Kazuki Iwasaki, Hiroaki Gofuku, Naoya Nishi, Tetsuo Sakka, Tetsuya Tsuda, and Susumu Kuwabata
   in preparation

List of Supplementary Publications

1. SEM Observation of Hydrous Superabsorbent Polymer Pretreated with Room-Temperature Ionic Liquid
   Tetsuya Tsuda, Eiko Mochizuki, Shoko Kishida, Kazuki Iwasaki, Katsuhiko Tsunashima, and Susumu Kuwabata
   PLOS ONE, **2014**, *9*, e91193/1–7.
2. Synthesis of Novel Ionic Liquids with Aromatic Trifluoroborate Anions
   Kazuki Iwasaki, Kazuki Yoshii, Seiji Tsuzuki, Tetsuya Tsuda, and Susumu Kuwabata
   ECS Transactions, **2014**, *64*, 83–93.
3. Physical and Electrochemical Properties of Ionic Liquids Based on Quaternary Phosphonium Cations and Carboxylate Anions as Electrolytes
   Jin Shimada, Katsuhiko Tsunashima, Mayu Ue, Kazuki Iwasaki, Tetsuya Tsuda, Susumu Kuwabata, Hideyuki Kanematsu, Nobumitsu Hirai, Takeshi Kogo, and Akiko Ogawa
   ECS Transactions, **2017**, *75*, 105–111.
4. Chemical Reactions in Ionic Liquid with an Epoxy Group
   Tetsuya Tsuda, Kazuki Iwasaki, Kohei Kumagai, and Susumu Kuwabata
   in preparation

Contents

General introduction

Salts are chemical compounds with Coulomb interaction. Most inorganic salts such as LiCl, NaCl, KBr and $CaCl_2$ have high melting points of 900 ~ 1500 K due to the strong Coulomb interaction. If the salts transform to the liquid state at the temperature over melting points, they are generally called "molten salts" which have unique features, e.g., reasonable vapor pressure, incombustibility, a wide electrochemical window, and high ionic conductivity.[1] Therefore, molten salts are very important nonaqueous solvents for electrochemical technologies.[2-5] However, not everyone can use molten salts, since special skills for handling the molten salts and knowledge of high temperature chemistry are required. Surprisingly, in 1914, Paul Walden reported the first room-temperature molten salt (melting point < 298 K), ethylammonium nitrate, in his article about the conductivity of molten salt systems.[6] This discovery enabled us to employ molten salts like aqueous solution. Now room-temperature molten salt is generally known as room-temperature ionic liquid (RTIL) or simply ionic liquid (IL). But, why does ethylammonium nitrate show such a low melting point? The answer is in its low lattice energy dominated by surface charge densities and molecular motion of ions. After moving into the 21st century, a great number of cations and anions for creating RTILs and low-temperature molten salts (melting point < 473 K) are proposed. Typical cations and anions are given in Figure I.[7, 8] Their common features are the large ionic volume and flexible ionic structure leading to lower lattice energy. However, even if RTIL is composed of the ions listed in Figure I, it is not always true that the RTIL shows favorable features. To design the RTIL is still a challenging and rewarding research.

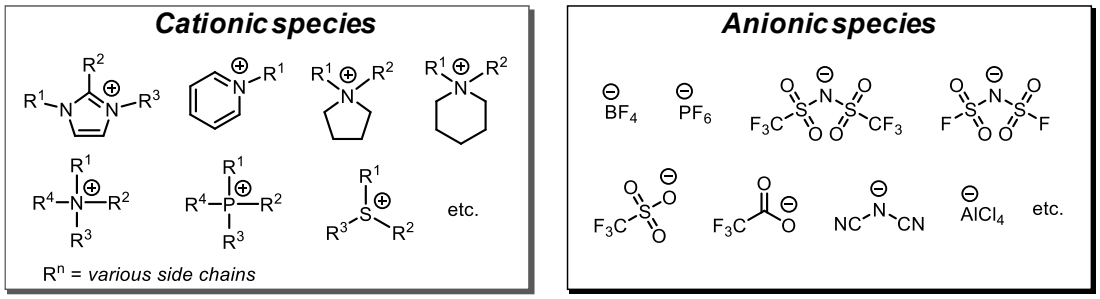

Figure I. Common cations and anions for room temperature ionic liquids.

General preparation method for RTIL is described elsewhere.[9-11] Most RTILs are synthesized by a metathesis reaction using organic halide with target cation, [Cation]X (X: Cl or Br), and metal salt with target anion, M[Anion] (M: Ag, Li, Na etc.). Acetonitrile, dichloromethane, and water are commonly used as a reaction solvent.

$$[\text{Cation}]X + M[\text{Anion}] \rightarrow [\text{Cation}][\text{Anion}]\ (\text{RTIL}) + MX\downarrow$$

For example, 1-butyl-3-methylimidazolium bis(trifluoromethanesulfonyl)amide ([C_4mim][$N(SO_2CF_3)_2$]) is obtained using 1-butyl-3-methylimidazolium chloride ([C_4mim]Cl) and lithium bis(trifluoromethanesulfonyl)amide (Li[$N(SO_2CF_3)_2$]). The most advantageous feature of RTILs is that their ionic structures can be readily designed by a synthetic chemistry technique, suggesting that the physicochemical properties can be also controlled.[12-16] For the [Cation]X, it is usually prepared from organic bases and alkyl halides.[17] As an example, Scheme I shows a chemical reaction process for synthesizing the [C_4mim]Cl by a simple nucleophilic substitution reaction of 1-methylimidazole and 1-chlorobutane.[18, 19] Not only alkyl chain but

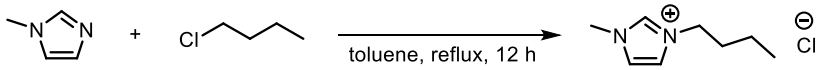

Scheme I. Reaction scheme for 1-butyl-3-methylimidazolium chloride.

also a wide variety of side chains can be introduced to the cation structure without difficulty. In the case of anion, it is not easy to create metal salts with novel anionic species although several interesting polyatomic anions, e.g., $[BF_4]^-$, $[PF_6]^-$, $[OSO_2CF_3]^-$, $[N(SO_2CF_3)_2]^-$, are commonly used, because the chemically stable structure with some electron withdrawing groups are needed to decrease the surface charge density. As given in Scheme II, Li[$N(SO_2CF_3)_2$] that is one of typical anion components in RTIL is synthesized via more than four step processes including the usage of an unstable gaseous CF_3SO_2F intermediate.[20-22] The process requires hazardous reagents and severe reaction conditions. Therefore, the approach for introducing target groups in the anion structure is inevitably restricted and there is almost no systematical study on the effect of introducing substituent to anion's framework.

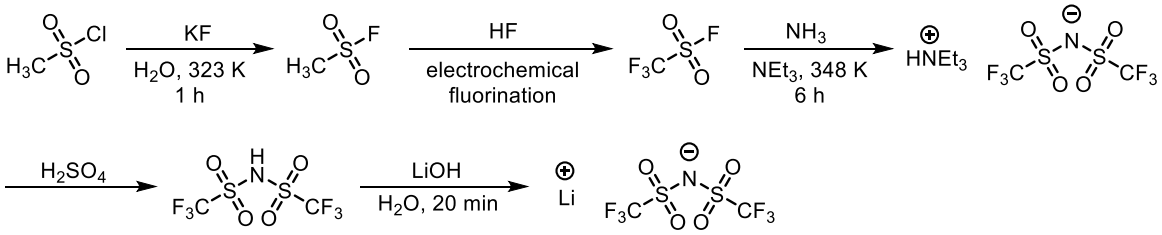

Scheme II. Reaction schemes for lithium bis(trifluoromethanesulfonyl)amide.

In order to design and synthesize metal salts with novel anions that become the RTIL component, I focused on aryltrifluoroborate anion ($[ArBF_3]^-$) depicted in Figure II, since Lennox, et al. recently reported an easy and safe preparation method for $[ArBF_3]^-$-based alkali metal salts (M[$ArBF_3$] (M: K or Cs)) on a large scale without any corrosive reagents as shown

in Scheme III.[23] The $[ArBF_3]^-$ has an analog structure of $[BF_4]^-$, that is, one fluorine in $[BF_4]^-$ is replaced with an aromatic ring. Because the BF_3^- group considerably decreases the negative charge on the aromatic ring, the decreased surface charge density may result in the low cation-anion interaction energy. In addition, different functional moieties can be introduced to the aromatic ring of $[ArBF_3]^-$ by a common chemical synthesis approach as with organic cations.

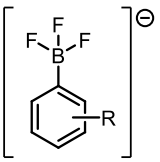

Figure II. Chemical structure of aryltrifluoroborate anion.

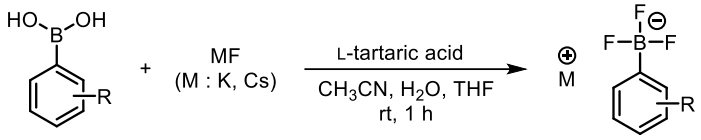

Scheme III. Reaction scheme for alkali metal aryltrifluoroborate.

In the present study, the author establishes the synthetic method for novel alkali metal salts with the $[ArBF_3]^-$, which are precursors for preparing RTILs. The objective of this work is to systematically reveal the influence of anionic structure on the physicochemical properties of the $[ArBF_3]^-$-based molten salts and RTILs leading to physicochemical property control by their molecular design. Chapter 1 covers the synthesis process for the alkali metal salts with various $[ArBF_3]^-$ anions. The influence of the substituents on the anions to thermal properties is discussed in detail. The electrochemistry of $[ArBF_3]^-$-based molten salt system is remarked. Chapter 2 describes that transport properties of the RTILs composed of phenyltrifluoroborate and different onium cations highly correlate with the molecular volume of the RTILs, which was estimated using the appropriate quantum chemical calculations. In Chapter 3, the equivalent conductivity and the electrochemical stability for some $[C_4mim][ArBF_3]$ RTILs are qualitatively discussed from the results of quantum chemical calculations of the cation-anion interaction and the HOMO energy level of the anion. In addition, $[C_4mim][ArBF_3]$ RTILs with an electron withdrawing group on the phenyl moiety electrochemically form an ion-selective membrane on a Pt electrode is presented.

Chapter 1 Synthesis and Evaluation of Alkali Metal Aryltrifluoroborate

1.1. Introduction

Molten salts which have particular features have been employed in various scientific field such as smelting, fuel cells, and chemical production.[1-5] Alkali metal salts are suitable material of room temperature ionic liquids (RTILs) as well as molten salts. The thermal and physicochemical properties of alkali metal salts can give an important information of the studies on RTILs. Alkali metal halides show much high melting point over 894 K. There are some approaches to develop the salts with low melting point. One is addition of other salt to an original salt expecting the increase of entropy with mixing, for example, LiCl–KCl binary systems[24-29] or NaCl–KCl–CsCl ternary systems.[30-35] Another is creation of ionic species with lower surface charge densities and flexible moieties such as bis(trifluoromethane-sulfonyl)amide ($[N(SO_2CF_3)_2]^-$). The latter approach is much efficient to handle molten salts at low temperature in single salt system. Therefore, the anion with the feature described above was required to develop the alkali metal salts which melt with lower temperature. However, few articles on the design and synthesis of alkali metal cation-based low-temperature molten salt systems with polyatomic anions are available[24-28, 30] because introducing target substituent(s) to a polyatomic anion is typically difficult because of the simple basic structure. Thus, the only limited number of anions can form the low-temperature-melting salt with alkali metal cations. Aryltrifluoroborate anions ($[ArBF_3]^-$), which are easily and safely prepared on a large scale using commercially available reagents,[23] can be applicable to the creation of alkali metal salts with relatively low melting temperatures and to the preparation of novel RTILs. In this chapter, the thermal and physicochemical properties of the nearly 40 kinds of novel alkali metal salts with $[ArBF_3]^-$ were revealed. In the case of the salts showing the lowest melting point, the author evaluated the electrochemical properties.

1.2. Experimental

1.2.1. Preparation of alkali metal aryltrifluoroborate

Aryltrifluoroborate alkali metal salts ($M[ArBF_3]$ (M: K or Cs)) were synthesized using appropriate arylboronic acids ($ArB(OH)_2$) (Wako Pure Chemical Co., Japan; Tokyo Chemical Co., Japan; and others), alkali metal fluorides (KF or CsF) (Wako Pure Chemical), and L-tartaric acid (Wako Pure Chemical), according to the following protocol.[23] An alkali metal fluoride

aqueous solution (4 equiv, 2 mL) containing the target cationic species was added to a solution of arylboronic acid (5 mmol) in acetonitrile (20 mL), and the mixture was stirred for 5 min at ambient temperature. L-Tartaric acid (2.05 equiv) dissolved in tetrahydrofuran (THF) (10 mL) was slowly added to the mixture, and then a white byproduct precipitated immediately. The reaction mixture was agitated for 1 h at ambient temperature and filtered to remove the precipitate. The resultant filtrate was concentrated in vacuo, and the crude alkali metal salt was obtained as a solid. The crude product was purified by recrystallization to give a pure aryltrifluoroborate alkali metal salt. The obtained salt was dried at 353 K under vacuum for 4 h. The final product was confirmed by nuclear magnetic resonance, mass spectrometry, and elemental analysis.

1.2.2. Thermal property measurements for alkali metal aryltrifluoroborate

Differential scanning calorimetry (DSC) was conducted using a Bruker DSC3100SA instrument. The sample was sealed in an aluminum pan with an aluminum top. The sealed pan was heated and cooled at a rate of 5 K min^{-1}. The glass-transition temperature and melting point were obtained from the DSC curve of the second heating process. These values were estimated by the tangential intersection method near the temperature at which a phase transformation occurred. Thermogravimetric (TG) analysis was performed using a Bruker TG-DTA2000SA instrument. The sample was placed on an aluminum pan, and the pan was heated from room temperature to 773 K at a rate of 5 K min^{-1} under flowing dry nitrogen gas. The thermal degradation temperature was determined as the 5 wt % loss point of the TG curve. These two instruments were controlled with a Bruker MTC1000SA workstation utilizing the Bruker WS003 software. All specimens for these measurements were prepared in an argon-gas-filled glove box (Vacuum Atmospheres Co., Omni-Lab, O_2 and H_2O < 1 ppm).

1.2.3. Electrochemical measurements for low temperature molten salt electrolyte

Electrochemical measurements were conducted using an IVIUM Technologies CompactStat portable electrochemical analyzer. All electrochemical experiments were performed in a three-electrode cell. The working electrode was a platinum disk (diameter of 1.6 mm), which was polished with an alumina suspension (diameter of 0.06 μm) before use. Platinum wire (diameter of 0.5 mm) was used as the counter electrode. Platinum and silver wires (diameters of 1.0 mm) were employed for the quasireference electrode. The measurement was conducted at 433 or 453 K in an argon-gas-filled glove box to prevent any contamination. When a potassium electrodeposition experiment was performed, a tin plate (5 mm × 5 mm) was used as the working electrode. Electrodeposition was conducted at 433 K in an argon-gas-filled glove box. The electrodeposits were observed by a Hitachi S-3400N scanning electron microscope (SEM) system. The composition was determined by an EDAX Octane Prime energy-dispersive X-ray spectroscopy (EDX) instrument mounted on the SEM system. The

crystal structure of the electrodeposit was identified by a Rigaku Ultima IV X-ray diffractometer (XRD) with Cu Kα radiation. This measurement was performed in the $2\theta/\theta$ scan mode with a scan rate of 1° min^{-1}. The electrochemical measurements were carried out in the abovementioned argon-filled-glove box.

1.2.4. Computational methods

The Gaussian 09 program[36] was used for the *ab initio* molecular orbital calculations. The basis sets implemented in the Gaussian program were used. Electron correlation was accounted for by the second-order Møller–Plesset perturbation (MP2) method.[37, 38] The geometries of complexes were fully optimized at the HF/6-311G(d,p) level. The intermolecular interaction energies (E_{int}) were calculated at the MP2/6-311G(d,p) level by the supermolecule method. The calculations of the $[C_2mim][BF_4]$ and $Li[N(SO_2CF_3)_2]$ complexes[39, 40] show that the effects of the basis sets on the calculated interaction energies of the complexes are very small, if basis sets including polarization functions are used, and that the effects of electron correlation beyond MP2 are negligible. Therefore, the author calculated the interaction energies of the complexes at the MP2/6-311G(d,p) level in this work. The basis set superposition error[41] was corrected for all of the interaction energy calculations using the counterpoise method.[42] The stabilization energy resulting from the formation of the complex from isolated ions (E_{form}) was calculated as the sum of Eint and deformation energy (E_{def}), which is the increase in the energy of the aryltrifluoroborate anion resulting from the deformation of the geometry associated with the complex formation.[39, 43] The E_{def} was calculated at the MP2/6-311G(d,p) level.

1.3. Results and discussion

1.3.1. Thermal behavior of alkali metal aryltrifluoroborate

A large number of aryltrifluoroborate alkali metal salts were prepared according to Scheme I, and their thermal properties were examined by DSC and TG analyses. The melting point (T_m) and thermal degradation temperature (T_d) of $M[ArBF_3]$ (M: K or Cs) with different substituents are given in Tables 1-1 to 1-4. Nonsubstitutive potassium phenyltrifluoroborate ($K[PhBF_3]$), which is the simplest aryltrifluoroborate potassium salt, had a melting point of 568 K (Table 1-1). The aromatic potassium salts with substituents, R, at the meta position of the phenyl group, $K[m\text{-}RC_6H_4BF_3]$, showed lower melting points than those of nonsubstitutive $K[PhBF_3]$, except for the *tert*-butyl, bromomethyl, and carbamoyl groups. Specifically, potassium (meta-ethoxyphenyl)trifluoroborate ($K[m\text{-}OEtC_6H_4BF_3]$) with an ethoxy group at the meta position on the aromatic ring melted at 390 K; thus, introducing the ethoxy group substantially decreased the melting point. As shown in Table 1-5, this value was considerably lower than those of other common potassium salts[24, 44-47] likely because of the increased interionic distances and entropies of the salts obtained. From these data, the author can also discuss the effects of the substituents

in a little more detail. For example, there is an obvious difference between the melting points of K[*m*-OMeC$_6$H$_4$BF$_3$] and K[*m*-OCF$_3$C$_6$H$_4$BF$_3$]. The OCF$_3$ group works as a strong electron withdrawing group because of the electronegativity of the three fluorine atoms. Consequently, the charge density of the anion decreases in the presence of the OCF$_3$ group compared to that in the presence of the OMe group without the fluorine atom. The resulting weak ionic interaction between the K^+ and [*m*-OCF$_3$C$_6$H$_4$BF$_3$]$^-$ would cause a lower melting point. As described later, quantum chemical calculations support this idea.

Table 1-1. Thermal properties of K[ArBF$_3$] salts with a substituent at the meta position

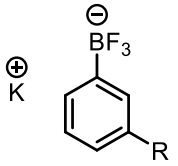

R	T_m[a] / K	T_d[b] / K	R	T_m[a] / K	T_d[b] / K
H	568	590	NO_2	525	566
CH_3	518	561	OCH_3 (ester)	516	576
$C(CH_3)_3$	—[c]	574	NH_2 (amide)	—[c]	445
CF_3	501	568	OCH_3	430	592
F	467	538	OCH_3	390	521
OCF_3	405	539	OCH_3	425	568
SCH_3	409	507	$OCH(CH_3)_2$	437	539
SO_2CH_3	514	600	OCH_3	439	548
Br	—[c]	410	OCH_3	388	549
CN	465	594	OCH_3	419	571

[a]Melting point. [b]Thermal degradation temperature at 5 wt% loss. [c]Decomposition before melting.

Table 1-2. Thermal properties of Cs[$ArBF_3$] salts with a substituent at the meta position

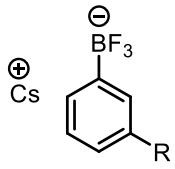

R	T_m [a] / K	T_d [b] / K
H	445	566
CF_3	403	549
F	409	611
OCF_3	398	534
SCH_3	413	565
OCH_3	433	572
OCH_2CH_3	409	567

[a]Melting point. [b]Thermal degradation temperature at 5 wt% loss.

Table 1-3. Thermal properties of K[$ArBF_3$] salts with a substituent at the ortho position

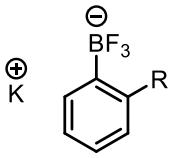

R	T_m [a] / K	T_d [b] / K
F	—[c]	587
OCF_3	—[c]	555
SCH_3	549	564
OCH_3	554	579
OCH_2CH_3	—[c]	565
NO_2	—[c]	492
$COCH_3$	—[c]	482

[a]Melting point. [b]Thermal degradation temperature at 5 wt% loss.
[c]Decomposition before melting.

A similar approach was also applied to Cs salt preparation. The thermal properties of Cs salts are summarized in Table 1-2. Cesium phenyltrifluoroborate (Cs[$PhBF_3$]) exhibited a melting point of 445 K, lower than that of its potassium counterpart. The same was true for other Cs salts with the following substituents at the meta position: CF_3, F, OCF_3, and O^{n}Pr. The larger ionic radius of the cesium ion compared to that of the potassium ion is commonly believed to decrease the Cs salt lattice energy.[24, 25, 27, 28] In contrast, the T_m of Cs salts with a methylthio or ethoxy group clearly increased compared to that of potassium salts with the same anions. These Cs salts should have a favorable ion packing structure. A similar exception regarding the melting temperatures derived from the differences in the cation and anion radii in inorganic alkali metal halides has been reported.[48, 49] The thermal properties of the ortho-substituted potassium aryltrifluoroborate (K[*o*-$RC_6H_4BF_3$]) are summarized in Table 1-3. Most salts showed only a thermal degradation temperature without a melting point. Furthermore, for these salts, it was much higher than those of the meta-substituted ones. To determine the underlying reason, the author carried out quantum chemical calculations for evaluating the

interactions of K^+ with substituted phenyltrifluoroborate anions. The optimized structures of the ion pairs of K^+ and meta- and ortho-substituted phenyltrifluoroborate anions are depicted in Figure 1-1. Whereas the K^+ has contact with three fluorine atoms of -BF_3^- in all of the ion pairs of meta-substituted phenyltrifluoroborates, in all of the ion pairs of ortho-substituted ones, the K^+ has contact with two fluorine atoms of -BF_3 and one negatively charged atom in the substituent. The stabilization energies resulting from the formation of the complexes from isolated species (E_{form}) calculated for the ion pairs and the difference between the E_{form} for the ion pair of meta-substituted phenyltrifluoroborate and the ion pair of ortho-substituted phenyltrifluoroborate (ΔE) are given in Figure 1-1. For example, the E_{form} calculated for the optimized structure of K[*m*-$OMeC_6H_4BF_3$] (−456.7 kJ mol^{-1}) was 34.4 kJ mol^{-1} smaller (less negative) than that for K[*o*-$OMeC_6H_4BF_3$] (−491.1 kJ mol^{-1}). The E_{form} calculated for the ion

Table 1-4. Thermal properties of other K[$ArBF_3$] salts

Potassium salts	T_m [a] / K	T_d [b] / K
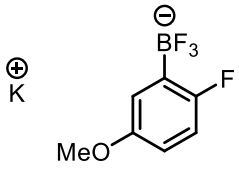	—[c]	481
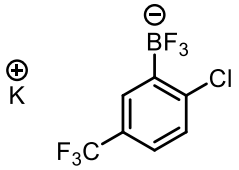	—[c]	404
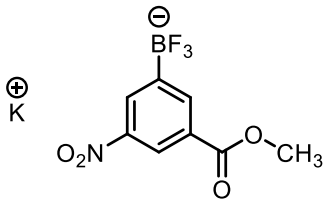	—[c]	495
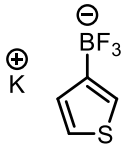	—[c]	550
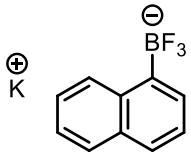	461	534

[a]Melting point. [b]Thermal degradation temperature at 5 wt% loss.
[c]Decomposition before melting.

pair of meta-substituted phenyltrifluoroborates is always smaller than that for the ion pair of corresponding ortho-substituted phenyltrifluoroborates. These calculations show that the dissociation of the ion pair of meta-substituted phenyltrifluoroborate can occur more easily than the dissociation of the ion pair of corresponding ortho-substituted phenyltrifluoroborates.[50, 51] The computational results suggest that the K^+ salts with meta-substituted phenyltrifluoroborates have lower melting temperatures compared to those of the salts of corresponding ortho-substituted phenyltrifluoroborates, owing to weaker attraction between the cation and anion. In addition to the aforementioned salts, the K^+ salts with three disubstituted phenyltrifluoroborate anions and two other aryltrifluoroborate anions were also synthesized (Table 1-4). These salts had no melting point except for a potassium 1-naphthyltrifluoroborate (K[1-NaphBF_3]). The thermal degradation temperatures of alkali salts with aryltrifluoroborate anions prepared in this study scatter over wide temperature ranges from 404–611 K. Different thermal stabilities of the substituents in aryltrifluoroborate anions would be the major source of difference of the thermal degradation temperatures.

Table 1-5. Melting points of common potassium salts

Salts	T_m[a] / K	Ref.
KF	1131	45
KCl	1043	46
KBr	1006	46
KI	952	46
KBF_4	803	44
K[$PhBF_3$]	568	this work
K[OSO_2CF_3]	503	47
K[$N(SO_2CF_3)_2$]	472	24
K[*m*-$OEtC_6H_4BF_3$]	390	this work

[a]Melting point.

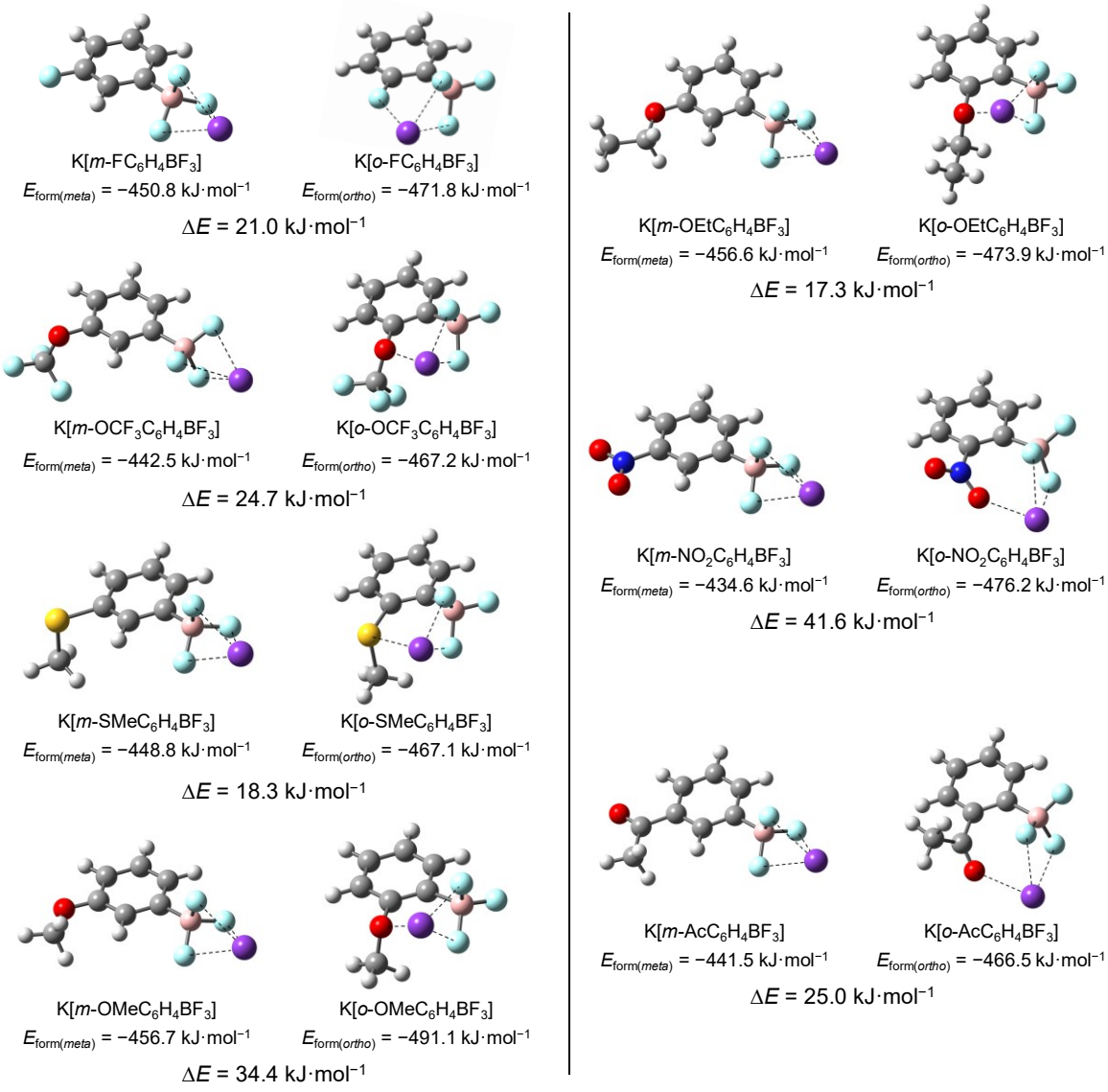

Figure 1-1. Optimized structures of ion pairs consisting of K^+ and meta- and ortho-substituted phenytrifluoroborate anions and their stabilization energies by the formation of ion pairs (E_{form}). ΔE (= $E_{form(meta)} - E_{form(ortho)}$) is the difference between the E_{form} for the ion pair of meta-substituted phenytrifluoroborate anion ($E_{form(meta)}$) and the E_{form} for the ion pair of ortho-substituted phenytrifluoroborate anion ($E_{form(ortho)}$).

1.3.2. Electrochemical analyses

As shown in Tables 1-1 to 1-4, K[*m*-OEtC$_6$H$_4$BF$_3$] had the lowest melting point, that is, 390 K, among the studied salts. Cyclic voltammograms recorded using a Pt disk electrode in the K[*m*-OEtC$_6$H$_4$BF$_3$] molten salt are shown in Figure 1-2. The electrochemical window was determined on the basis of the anodic and cathodic limiting potentials at which the current densities reached ±0.3 mA cm^{-2} in a forward scan. The current increment initiated at ca. 1.36 V (vs. quasi-Pt wire reference electrode) and ca. 0.71 V (vs. quasi-Ag wire reference electrode) in the anodic region (blue line) was attributable to the decomposition of the [*m*-OEtC$_6$H$_4$BF$_3$]$^-$ anion. In the cathodic region (red line), the negative limiting potential was ca. −2.48 V (vs. Pt wire) and ca. −3.13 V (vs. Ag wire). Hence, the electrochemical window was 3.84 V at 453 K. This range is comparable to those of typical alkali metal molten salt systems, such as LiCl–KCl (3.8 V).[52-54] Therefore, this K[*m*-OEtC$_6$H$_4$BF$_3$] molten salt shows great promise as a low-temperature molten salt. Further electrochemical analyses were conducted to elucidate the unknown electrochemical redox reactions observed at the negative limiting potential. As shown in Figure 1-2, a small oxidation peak appeared at −2.3 V (vs. Pt wire) in the reverse scan of the cathodic region. The author speculated that the oxidation wave was related to the dissolution of metal potassium deposited in the potential range of −2.4 to −2.5 V (vs. Pt wire). However, the Coulombic efficiency of the redox reaction estimated based on the cyclic voltammogram was only 4%. Given metallic potassium's low melting point (337 K), it is highly likely that the metal potassium electrodeposited on the electrode floats or precipitated in the K[*m*-OEtC$_6$H$_4$BF$_3$] molten salt at 453 K soon after deposition. These processes would lead to the observed significantly low Coulombic efficiency. In fact, the author could not identify any deposits on the Pt electrode after electrolysis at the limiting potential. The author collected more accurate

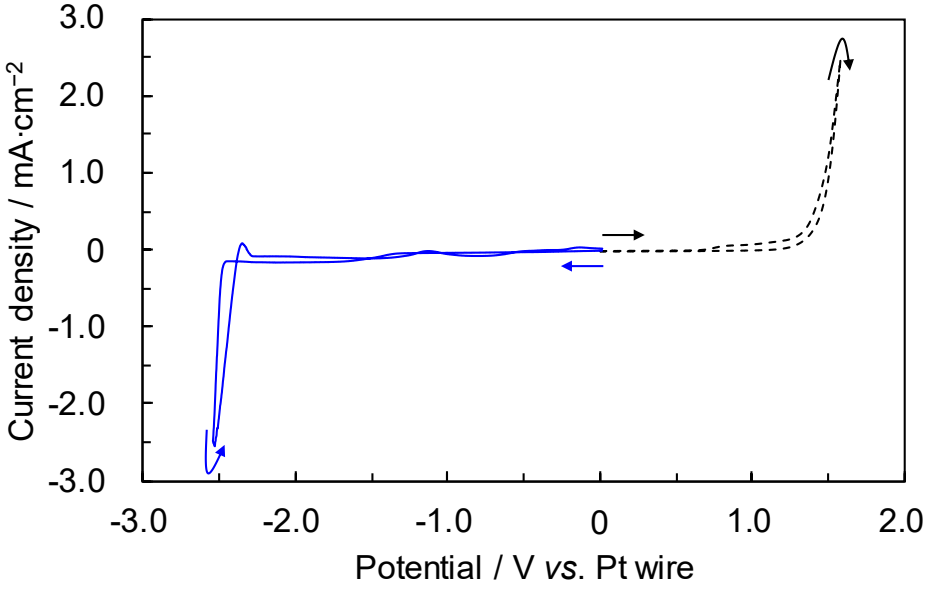

Figure 1-2. Cyclic voltammograms recorded at a Pt disk electrode in (—) the cathodic region and (---) the anodic region in the K[*m*-OEtC$_6$H$_4$BF$_3$] low-temperature molten salt at 453 K. The scan rate was 10 mV s^{-1}.

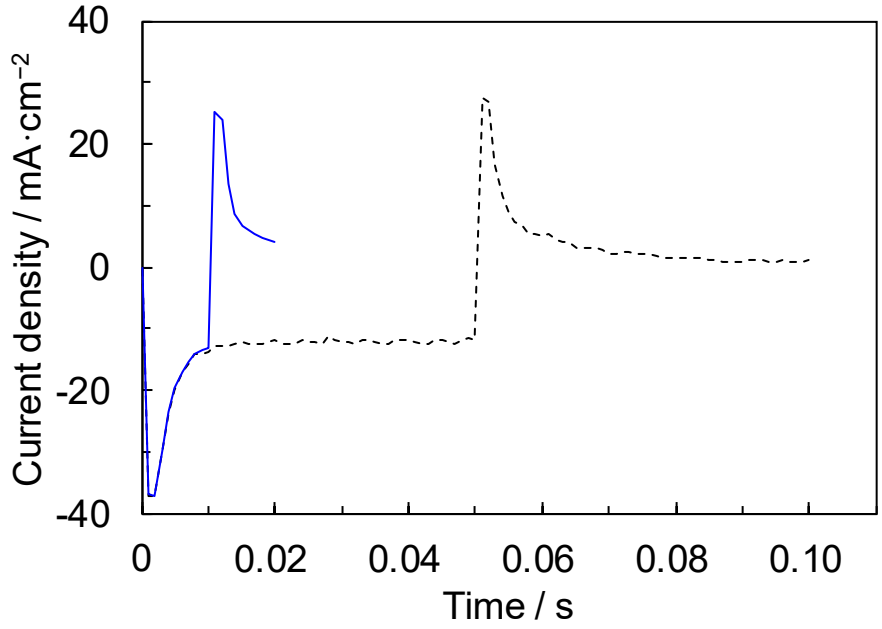

Figure 1-3. Double-step chronoamperograms recorded at a Pt disk electrode in the K[*m*-OEtC$_6$H$_4$BF$_3$] low-temperature molten salt at 433 K with a potential step of −2.6 V (vs. Pt wire) followed by 0 V (vs. Pt wire). The potential step times were (—) 0.01 s and (---) 0.05 s.

information on the relevant electrochemical reaction via two approaches: double-step chronoamperometry using short potential step times and alloying with a tin electrode that can readily form a K–Sn binary alloy.[55] Figure 1-3 shows the double-step chronoamperograms recorded using a Pt disk electrode in the K[*m*-OEtC$_6$H$_4$BF$_3$] molten salt at 433 K. On the basis of these chronoamperograms, the author can discuss the kinetic complications involved in the electrode reaction. When a certain type of ionic species is oxidized or reduced ideally on the electrode surface during double-step chronoamperometry, the kinetic complications are determined by the following equation[56]

$$-\frac{i_\mathrm{r}}{i_\mathrm{f}} = 1 - \left(1 - \frac{\tau}{t_\mathrm{r}}\right)^{1/2} \tag{1-1}$$

where i_f is the forward current in the first potential step, i_r is the reversal current in the second potential step, t_r is the time at any current in the second potential step, and τ is the retention time of the first potential step. Figure 1-4a depicts an ideal current response in double-step chronoamperometry when the first step is the cathodic reaction. The data shown in Figure 1-3 were converted into $-i_\mathrm{r}/i_\mathrm{f}$ and t_r/τ by eq 1-1 and are presented graphically in Figure 1-4b. The solid line in the figure represents an ideal line calculated using this equation. At a longer step time, that is, 0.05 s, a large deviation from the ideal line occurred. Conversely, the plots were very similar to the ideal line when a shorter time step of 0.01 s was used. Therefore, the electrode reaction proceeded reversibly at only very short reduction potential step times. Direct

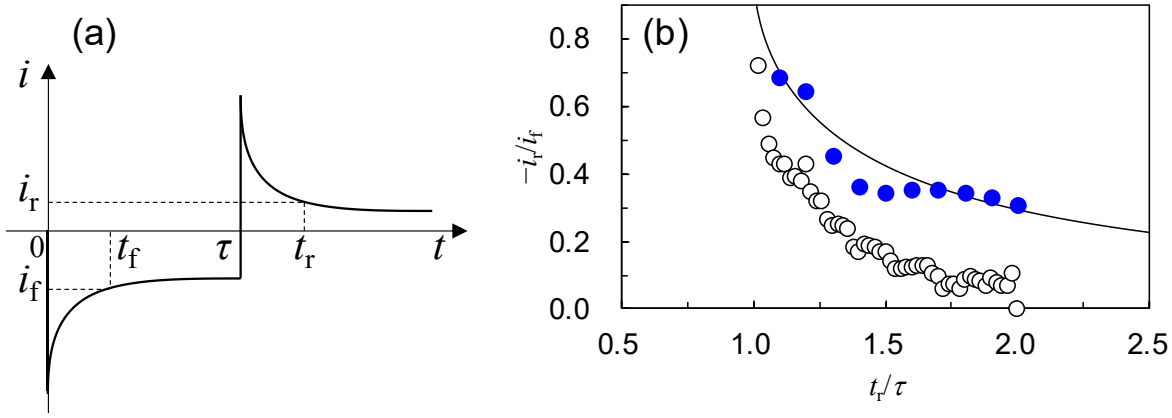

Figure 1-4. (a) Ideal current response in typical double-step chronoamperometry. i_f is the forward current in the first potential step, i_r is the reversal current in the second potential step, t_f is the time at any current in the first potential step, and τ is the potential step time for the first potential step. (b) $-i_r/i_f$ vs. t_r/τ plot derived from the chronoamperograms shown in Fig. 1-3. The potential step times were (○) 0.05 s and (●) 0.01 s. The solid line in the figure represents the ideal line calculated using eq. 1-1.

evidence of potassium electrodeposition was obtained by constant-potential electrolysis at −2.6 V (vs. Pt wire) for 3600 s on a Pt electrode. No deposits were identified. However, when a tin plate with metallic luster was used as the working electrode (Figure 1-5a), the surface became covered with a dark gray deposit under the same electrolysis conditions (Figure 1-5b). SEM

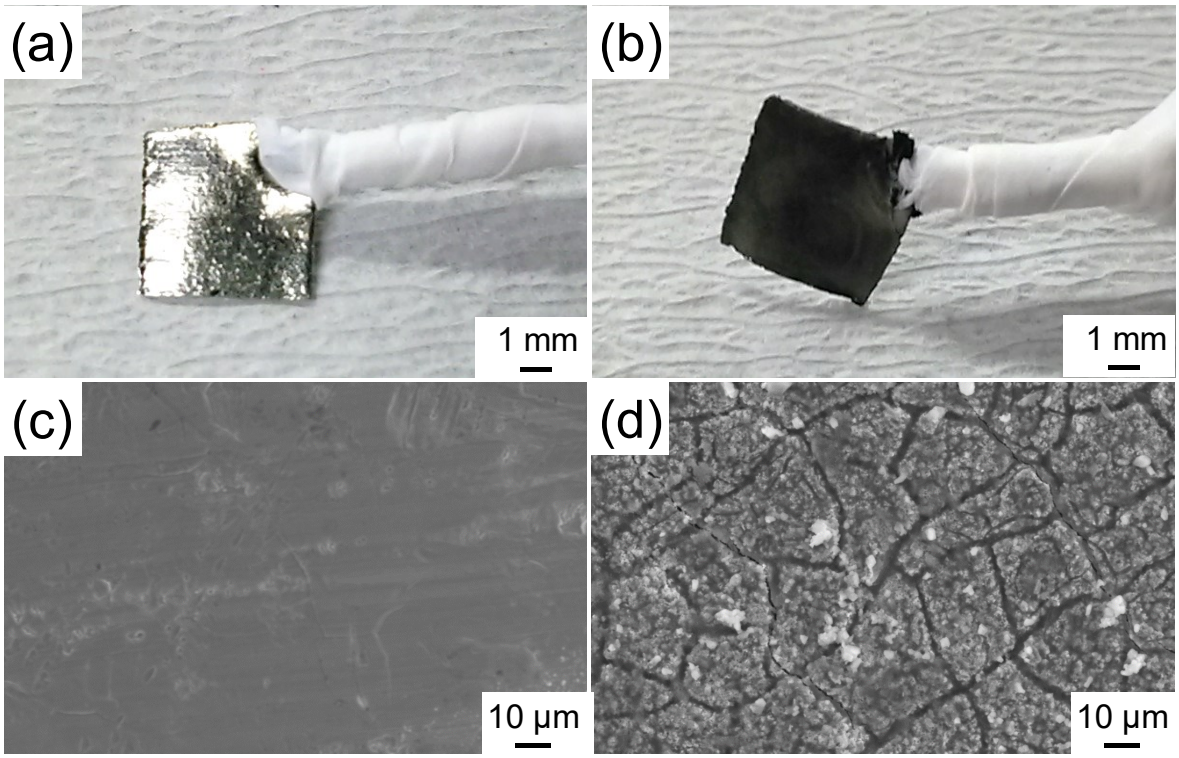

Figure 1-5. Optical microscope and SEM images of the tin electrode (a and c) before and (b and d) after electrolysis at −2.6 V (vs. Pt wire) in the K[*m*-OEtC$_6$H$_4$BF$_3$] low-temperature molten salt at 433 K. The SEM images are shown in (c) and (d).

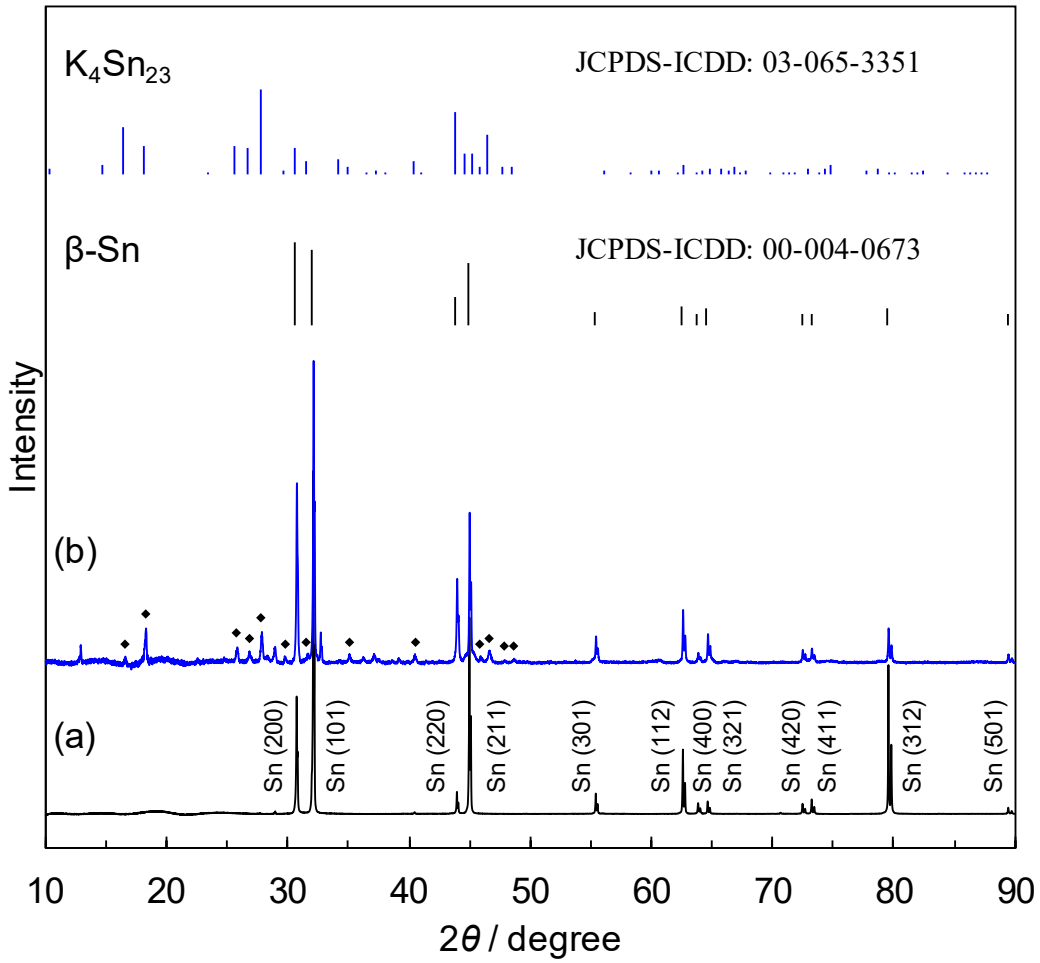

Figure 1-6. XRD patterns (Cu-Kα) of the tin electrode before and after electrolysis at −2.6 V (vs. Pt wire) in the K[*m*-$OEtC_6H_4BF_3$] low-temperature molten salt at 433 K. As references, the diffraction patterns of β-Sn (JCPDS-ICDD, file 00-004-0673) and K_4Sn_{23} (JCPDS-ICDD, file 03-065-3351) are also shown.

images of the electrode surface before and after electrolysis are shown in Figure 1-5c and d, respectively. The original tin electrode had a smooth surface, but after electrolysis, the surface exhibited a dramatic change, becoming rough with many cracks.[57-59] The tin electrode was characterized by XRD, and the results obtained before and after electrolysis are shown in Figure 1-6. The specimen after electrolysis had a unique XRD pattern. In addition to that of metallic tin, the pattern for the K_4Sn_{23} binary alloy was also evident; thus, the K–Sn binary alloy was formed on the Sn electrode surface. The K–Sn alloy probably formed immediately after K(I) reduction on the Sn electrode. EDX analysis of the specimen indicated that the major components were potassium and tin. On the basis of these results, the redox reaction observed at the negative limiting potential in the K[*m*-$OEtC_6H_4BF_3$] molten salt was identified as the electrode reaction for K(I), which is in agreement with the results of the few papers available that address metal potassium deposition in ILs and organic solvents.[60-62]

1.4. Summary

Nearly 40 aryltrifluoroborate alkali metal salts with various substituents were designed and successfully obtained via a simple and safe preparation process. The author revealed that the choice of substituents and their positions strongly affected the thermal properties of the resulting salts. The alkali metal salts clearly had lower melting points than those of common inorganic alkali halides, for example, LiCl, KCl, and KF. The author used a structure-designed potassium aryltrifluoroborate, K[*m*-OEt$C_6H_4BF_3$] as a low temperature molten salt electrolyte for the electrodeposition of metal potassium.

1.5. Characterization data

^{1}H, ^{13}C, ^{19}F, and ^{11}B NMR spectra were recorded on a JEOL JNM-ECS400 spectrometer operating at 400, 100, 376, and 128 MHz, respectively. $CDCl_3$ was used as the solvent for the samples in this study. The ^{1}H and ^{13}C NMR spectra were referenced to the residual solvent signal as the internal standard: $CDCl_3$ δ = 7.26 ppm (^{1}H) and δ = 77.0 ppm (^{13}C). The chemical shift values in the ^{19}F and ^{11}B NMR were reported relative to the external references, $C_6H_5CF_3$ δ = −63.7 ppm (^{19}F) and $BF_3{\cdot}OEt_2$ δ = 0.0 ppm (^{11}B). The signal for the ^{13}C binding ^{11}B atom was too broad due to the quadrupolar relaxation mechanism of the ^{11}B nucleus.[63] High-resolution mass spectrometry (HRMS) was performed on a JEOL JMS-700 MStation mass spectrometer using fast atom bombardment (FAB) ionization. HRMS and elemental analysis (C, H, and N) were performed at the Analytical Instrumentation Facility, Graduate School of Engineering, Osaka University.

Potassium phenyltrifluoroborate (K[$PhBF_3$]):

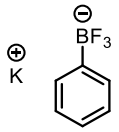

Yield: 90 %, white solid. ^{1}H NMR (400 MHz, CD_3CN): σ 7.07 (m, 1H, arom. H), 7.14 (t, 2H, J = 7.2 Hz, arom. H), 7.40 (d, 2H, $^{3}J_{HH}$ = 7.2 Hz, arom. H). ^{13}C NMR (100 MHz, CD_3CN): σ 126.5 (s), 127.6 (s), 132.3 (s). ^{19}F NMR (376 MHz, CD_3CN): σ −141.6 (q, 3F, $^{1}J_{BF}$ = 51.7 Hz, BF_3). ^{11}B NMR (128 MHz, CD_3CN): σ 3.84 (q, $^{1}J_{BF}$ = 56.4 Hz). HRMS (FAB), *m*/*z*: calcd. for $C_6H_5BF_3K_2^+$ 222.9705 $[M + K]^+$; found 222.9709. Elemental analysis calcd. for $C_6H_5BF_3K$: C, 39.16; H, 2.74; found: C, 39.19; H, 2.97.

Potassium (meta-methylphenyl)trifluoroborate (K[*m*-MeC$_6$H$_4$BF$_3$]):

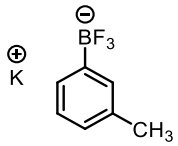

Yield: 97 %, white solid. ^{1}H NMR (400 MHz, CD$_3$CN): σ 2.25 (s, 3H, C*H$_3$*), 6.92 (t, 1H, J = 8.8 Hz, arom. H), 7.04 (q, 1H, J = 7.8 Hz, arom. H), 7.18–7.27 (m, 2H, arom. H). ^{13}C NMR (100 MHz, CD$_3$CN): σ 21.7 (s, *C*H$_3$), 127.3 (d, J = 23.8 Hz), 127.6 (d, J = 9.5 Hz), 129.3 (s), 133.1 (s), 136.5 (d, J = 11.6 Hz). ^{19}F NMR (376 MHz, CD$_3$CN): σ −140.7 (d, 3F, $^1J_{BF}$ = 62.4 Hz, B*F$_3$*). ^{11}B NMR (128 MHz, CD$_3$CN): σ 3.91 (d, $^1J_{BF}$ = 56.3 Hz). HRMS (FAB), *m*/*z*: calcd. for C$_7$H$_7$BF$_3$K$_2^+$ 236.9862 [M + K]$^+$; found 236.9869. Elemental analysis calcd. for C$_7$H$_7$BF$_3$K: C, 42.46; H, 3.56; found: C, 42.17; H, 3.72.

Potassium (meta-*tert*-butylphenyl)trifluoroborate (K[*m*-^{t}BuC$_6$H$_4$BF$_3$]):

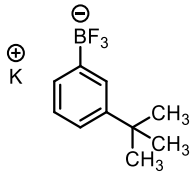

Yield: 99 %, white solid. ^{1}H NMR (400 MHz, CD$_3$CN): σ 1.27 (s, 9H, C(CH$_3$)$_3$), 7.06–7.23 (m, 3H, arom. H), 7.49 (s, 1H, arom. H). ^{13}C NMR (100 MHz, CD$_3$CN): σ 31.9 (s), 35.0 (s), 123.5 (s), 127.3 (s), 128.9 (s), 129.5 (s), 149.6 (s). ^{19}F NMR (376 MHz, CD$_3$CN): σ −142.4 (d, 3F, $^1J_{BF}$ = 57.5 Hz, B*F$_3$*). ^{11}B NMR (128 MHz, CD$_3$CN): σ 4.03 (d, $^1J_{BF}$ = 55.0 Hz). HRMS (FAB), *m*/*z*: calcd. for C$_{10}$H$_{13}$BF$_3$K$_2^+$ 279.0331 [M + K]$^+$; found 279.0343. Elemental analysis calcd. for C$_{10}$H$_{13}$BF$_3$K: C, 50.02; H, 5.46; found: C, 49.70; H, 5.55.

Potassium (meta-trifluoromethylphenyl)trifluoroborate (K[*m*-CF$_3$C$_6$H$_4$BF$_3$]):

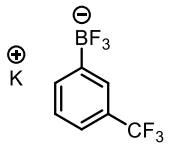

Yield: 93 %, white solid. ^{1}H NMR (400 MHz, CD$_3$CN): σ 7.33 (t, 1H, J = 7.6 Hz, arom. H), 7.41 (d, 1H, $^3J_{HH}$ = 7.6 Hz, arom. H), 7.67–7.71 (m, 2H, arom. H). ^{13}C NMR (100 MHz, CD$_3$CN): σ 123.2 (q, $^3J_{CF}$ = 3.8 Hz), 126.4 (q, $^1J_{CF}$ = 272.6 Hz, *C*F$_3$), 128.1 (s), 128.5 (s), 129.0 (q, $^2J_{CF}$ = 30.6 Hz), 136.1 (s). ^{19}F NMR (376 MHz, CD$_3$CN): σ −143.6 (d, 3F, $^1J_{BF}$ = 57.5 Hz, B*F$_3$*), −63.1 (s, 3F, C*F$_3$*). ^{11}B NMR (128 MHz, CD$_3$CN): σ 3.51 (q, $^1J_{BF}$ = 50.1 Hz). HRMS (FAB), *m*/*z*: calcd. for C$_7$H$_4$BF$_6$K$_2^+$ 290.9579 [M + K]$^+$; found 290.9579. Elemental analysis calcd. for C$_7$H$_4$BF$_6$K: C, 33.36; H, 1.60; found: C, 33.48; H, 1.93.

Potassium (meta-fluorophenyl)trifluoroborate (K[*m*-FC$_6$H$_4$BF$_3$]):

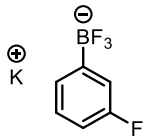

Yield: 82 %, white solid. ^{1}H NMR (400 MHz, CD$_3$CN): σ 6.79 (t, 1H, J = 8.9 Hz, arom. H), 7.09 (d, 1H, $^3J_{HH}$ = 10.0 Hz, arom. H), 7.12–7.21 (m, 2H, arom. H). ^{13}C NMR (100 MHz, CD$_3$CN): σ 113.0 (d, $^2J_{CF}$ = 21.1 Hz), 118.1 (d, $^2J_{CF}$ = 17.3 Hz), 128.0 (s), 129.5 (s), 163.5 (d, $^1J_{CF}$ = 233.3 Hz). ^{19}F NMR (376 MHz, CD$_3$CN): σ −143.3 (q, 3F, $^1J_{BF}$ = 51.7 Hz, B*F$_3$*), −117.8 (s, 1F, 3-*F*). ^{11}B NMR (128 MHz, CD$_3$CN): σ 3.35 (q, $^1J_{BF}$ = 53.3 Hz). HRMS (FAB), *m*/*z*: calcd. for $C_6H_4BF_4K_2^+$ 240.9611 $[M + K]^+$; found 240.9627. Elemental analysis calcd. for $C_6H_4BF_4K$: C, 35.68; H, 2.00; found: C, 35.66; H, 2.06.

Potassium (meta-trifluoromethoxyphenyl)trifluoroborate (K[*m*-OCF$_3$C$_6$H$_4$BF$_3$]):

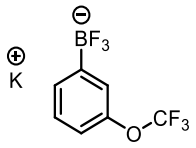

Yield: 52 %, pale yellow solid. ^{1}H NMR (400 MHz, CD$_3$CN): σ 7.02 (d, 1H, $^3J_{HH}$ = 8.2 Hz, arom. H), 7.25 (t, 1H, J = 7.8 Hz, arom. H), 7.30 (s, 1H, arom. H), 7.42 (d, 1H, $^3J_{HH}$ = 7.3 Hz, arom. H). ^{13}C NMR (100 MHz, CD$_3$CN): σ 119.2 (s), 121.4 (q, $^1J_{CF}$ = 235.7 Hz, O*C*F$_3$), 124.2 (s), 129.4 (s), 131.1 (s), 149.5 (s). ^{19}F NMR (376 MHz, CD$_3$CN): σ −143.4 (d, 3F, $^1J_{BF}$ = 58.4 Hz, B*F$_3$*), −58.6 (s, 3F, OC*F$_3$*). ^{11}B NMR (128 MHz, CD$_3$CN): σ 3.47 (q, $^1J_{BF}$ = 48.1 Hz). HRMS (FAB), *m*/*z*: calcd. for $C_7H_4OBF_6K_2^+$ 306.9528 $[M + K]^+$; found 306.9533. Elemental analysis calcd. for $C_7H_4OBF_6K$: C, 31.37; H, 1.50; found: C, 30.70; H, 1.86.

Potassium (meta-methylthiophenyl)trifluoroborate (K[*m*-SMeC$_6$H$_4$BF$_3$]):

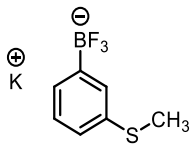

Yield: 72 %, pale yellow solid. ^{1}H NMR (400 MHz, CD$_3$CN): σ 2.41 (s, 3H, SC*H$_3$*), 7.04 (d, 1H, $^3J_{HH}$ = 7.8 Hz, arom. H), 7.11 (t, 1H, J = 7.6 Hz, arom. H), 7.22 (d, 1H, $^3J_{HH}$ = 7.3 Hz, arom. H), 7.36 (s, 1H, arom. H). ^{13}C NMR (100 MHz, CD$_3$CN): σ 16.0 (s, S*C*H$_3$), 125.1 (s), 128.4 (s), 129.3 (s), 130.7 (s), 136.9 (s). ^{19}F NMR (376 MHz, CD$_3$CN): σ −142.9 (d, 3F, $^1J_{BF}$ = 49.7 Hz, B*F$_3$*). ^{11}B NMR (128 MHz, CD$_3$CN): σ 3.76 (d, $^1J_{BF}$ = 44.9 Hz). HRMS (FAB), *m*/*z*: calcd. for $C_7H_7SBF_3K_2^+$ 268.9582 $[M + K]^+$; found 268.9591. Elemental analysis calcd. for $C_7H_7SBF_3K$:

C, 36.54; H, 3.07; found: C, 35.93; H, 3.21.

Potassium (meta-methylsulfonylphenyl)trifluoroborate (K[*m*-$SO_2MeC_6H_4BF_3$]):

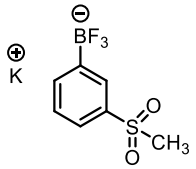

Yield: 86 %, white solid. ^{1}H NMR (400 MHz, CD_3CN): σ 2.98 (s, 3H, SO_2CH_3), 7.38 (t, 1H, J = 7.8 Hz, arom. H), 7.64 (d, 1H, $^3J_{HH}$ = 7.7 Hz, arom. H), 7.74 (d, 1H, $^3J_{HH}$ = 7.3 Hz, arom. H), 7.92 (s, 1H, arom. H). ^{13}C NMR (100 MHz, CD_3CN): σ 44.6 (s, SO_2CH_3), 125.2 (s), 128.5 (s), 130.4 (s), 137.6 (s), 140.0 (s). ^{19}F NMR (376 MHz, CD_3CN): σ −143.6 (q, 3F, $^1J_{BF}$ = 52.6 Hz, BF_3). ^{11}B NMR (128 MHz, CD_3CN): σ 3.31 (d, $^1J_{BF}$ = 50.8 Hz). HRMS (FAB), *m*/*z*: calcd. for $C_7H_7O_2SBF_3K_2^+$ 300.9481 $[M + K]^+$; found 300.9492. Elemental analysis calcd. for $C_7H_7O_2SBF_3K$: C, 32.08; H, 2.69; found: C, 32.08; H, 2.87.

Potassium (meta-bromomethylphenyl)trifluoroborate (K[*m*-$CH_2BrC_6H_4BF_3$]):

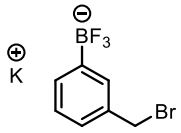

Yield: 81 %, white solid. ^{1}H NMR (400 MHz, CD_3CN): σ 4.64 (s, 2H, CH_2Br), 7.06–7.13 (m, 2H, arom. H), 7.26 (d, 1H, $^3J_{HH}$ = 6.4 Hz, arom. H), 7.38 (s, 1H, arom. H). ^{13}C NMR (100 MHz, DMSO-d^6): σ 36.6 (s, CH_2Br), 126.1 (s), 126.6 (s), 131.5 (s), 132.5 (s), 135.3 (s). ^{19}F NMR (376 MHz, DMSO-d^6): σ −141.7 (br, 3F, BF_3). ^{11}B NMR (128 MHz, DMSO-d^6): σ 3.66 (br). HRMS (FAB), *m*/*z*: calcd. for $C_7H_6BrBF_3K_2^+$ 314.8967 $[M + K]^+$; found 314.8979.

Potassium (meta-cyanophenyl)trifluoroborate (K[*m*-$CNC_6H_4BF_3$]):

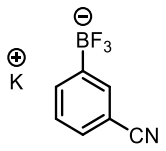

Yield: 99 %, white solid. ^{1}H NMR (400 MHz, CD_3CN): σ 7.29 (t, 1H, J = 11.5 Hz, arom. H), 7.44 (dt, 1H, J = 7.6 Hz, ^4J = 1.6 Hz, arom. H), 7.69 (d, 1H, $^3J_{HH}$ = 7.3 Hz, arom. H), 7.72 (s, 1H, arom. H). ^{13}C NMR (100 MHz, CD_3CN): σ 111.2 (s), 121.2 (s), 128.4 (s), 130.2 (s), 135.9 (s), 136.9 (s). ^{19}F NMR (376 MHz, CD_3CN): σ −143.8 (q, 3F, $^1J_{BF}$ = 48.7 Hz, BF_3). ^{11}B NMR (128 MHz, CD_3CN): σ 3.16 (q, $^1J_{BF}$ = 49.4 Hz). HRMS (FAB), *m*/*z*: calcd. for $C_7H_4NBF_3K_2^+$ 247.9658 $[M + K]^+$; found 247.9661. Elemental analysis calcd. for $C_7H_4NBF_3K$: C, 40.22; H,

1.93; N, 6.70; found: C, 38.94; H, 2.16; N, 6.60.

Potassium (meta-nitrophenyl)trifluoroborate (K[*m*-$NO_2C_6H_4BF_3$]):

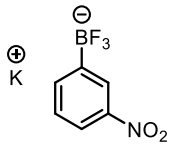

Yield: 85 %, yellow solid. ^{1}H NMR (400 MHz, CD_3CN): σ 7.37 (t, 1H, J = 7.8 Hz, arom. H), 7.80 (d, 1H, $^{3}J_{HH}$ = 7.2 Hz, arom. H), 7.94 (d, 1H, $^{3}J_{HH}$ = 8.0 Hz, arom. H), 8.21 (s, 1H, arom. H). ^{13}C NMR (100 MHz, CD_3CN): σ 121.6 (s), 126.4 (s), 128.7 (s), 138.9 (s), 148.6 (s). ^{19}F NMR (376 MHz, CD_3CN): σ −143.8 (q, 3F, $^{1}J_{BF}$ = 48.7 Hz, B*F*$_3$). ^{11}B NMR (128 MHz, CD_3CN): σ 3.21 (q, $^{1}J_{BF}$ = 50.8 Hz). HRMS (FAB), *m*/*z*: calcd. for $C_6H_4NO_2BF_3K_2^+$ 267.9556 $[M + K]^+$; found 267.9566. Elemental analysis calcd. for $C_6H_4NO_2BF_3K$: C, 31.47; H, 1.76; N, 6.12; found: C, 31.15; H, 1.88; N, 6.14.

Potassium (meta-ethoxycarbonylphenyl)trifluoroborate (K[*m*-$CO_2EtC_6H_4BF_3$]):

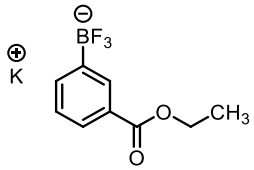

Yield: 97 %, white solid. ^{1}H NMR (400 MHz, CD_3CN): σ 1.32 (t, 3H, $^{3}J_{HH}$ = 7.1 Hz, $CO_2CH_2CH_3$), 4.27 (q, 2H, $^{3}J_{HH}$ = 7.0 Hz, $CO_2CH_2CH_3$), 7.25 (t, 1H, J = 7.6 Hz, arom. H), 7.64 (d, 1H, $^{3}J_{HH}$ = 7.3 Hz, arom. H), 7.73 (d, 1H, $^{3}J_{HH}$ = 7.8 Hz, arom. H), 8.04 (s, 1H, arom. H). ^{13}C NMR (100 MHz, CD_3CN): σ 14.6 (s), 61.2 (s), 127.5 (s), 127.7 (s), 129.6 (s), 133.2 (s), 137.1 (s), 168.5 (s). ^{19}F NMR (376 MHz, CD_3CN): σ −143.2 (d, 3F, $^{1}J_{BF}$ = 49.8 Hz, B*F*$_3$). ^{11}B NMR (128 MHz, CD_3CN): σ 3.54 (d, $^{1}J_{BF}$ = 52.8 Hz). HRMS (FAB), *m*/*z*: calcd. for $C_9H_9O_2BF_3K_2^+$ 294.9916 $[M + K]^+$; found 294.9916. Elemental analysis calcd. for $C_9H_9O_2BF_3K$: C, 42.21; H, 3.54; found: C, 41.38; H, 3.60.

Potassium (meta-carbamoylphenyl)trifluoroborate (K[*m*-$CONH_2C_6H_4BF_3$]):

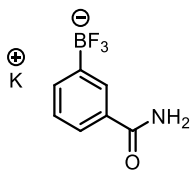

Yield: 70 %, white solid. ^{1}H NMR (400 MHz, DMSO-*d*^{6}): σ 7.00 (s, 1H, CON*H*$_2$), 7.14 (t, 1H, J = 7.6 Hz, arom. H), 7.45 (d, 1H, $^{3}J_{HH}$ = 7.3 Hz, arom. H), 7.54 (d, 1H, $^{3}J_{HH}$ = 7.8 Hz, arom.

H), 7.76 (s, 1H, CONH_2), 7.85 (s, 1H, arom. H). ^{13}C NMR (100 MHz, DMSO-d^6): σ 124.4 (s), 125.9 (s), 130.5 (s), 132.2 (s), 134.3 (s), 169.5 (s, *C*ONH$_2$). ^{19}F NMR (376 MHz, DMSO-d^6): σ −141.5 (br, 3F, BF_3). ^{11}B NMR (128 MHz, DMSO-d^6): σ 3.77 (br). HRMS (FAB), *m*/*z*: calcd. for $C_7H_6NOBF_3K_2^+$ 265.9763 [M + K]$^+$; found 265.9769.

Potassium (meta-methoxyphenyl)trifluoroborate (K[*m*-OMeC$_6$H$_4$BF$_3$]):

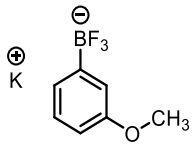

Yield: 94 %, white solid. ^{1}H NMR (400 MHz, CD$_3$CN): σ 3.72 (s, 3H, OCH_3), 6.66 (d, 1H, $^3J_{HH}$ = 7.6 Hz, arom. H), 7.00–7.02 (m, 2H, arom. H), 7.08 (t, 1H, *J* = 7.8 Hz, arom. H). ^{13}C NMR (100 MHz, CD$_3$CN): σ 55.3 (s, O*C*H$_3$), 112.3 (s), 117.3 (s), 124.8 (s), 128.7 (s), 159.7 (s). ^{19}F NMR (376 MHz, CD$_3$CN): σ −142.8 (d, 3F, $^1J_{BF}$ = 56.2 Hz, BF_3). ^{11}B NMR (128 MHz, CD$_3$CN): σ 3.86 (d, $^1J_{BF}$ = 46.9 Hz). HRMS (FAB), *m*/*z*: calcd. for $C_7H_7OBF_3K_2^+$ 252.9811 [M + K]$^+$; found 252.9818. Elemental analysis calcd. for $C_7H_7OBF_3K$: C, 39.28; H, 3.30; found: C, 38.71; H, 3.27.

Potassium (meta-ethoxyphenyl)trifluoroborate (K[*m*-OEtC$_6$H$_4$BF$_3$]):

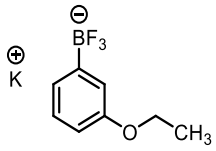

Yield: 87 %, white solid. ^{1}H NMR (400 MHz, CD$_3$CN): σ 1.30 (t, 3H, $^3J_{HH}$ = 7.1 Hz, OCH$_2$CH_3), 3.97 (q, 2H, $^3J_{HH}$ = 7.1 Hz, OCH_2CH$_3$), 6.64 (d, 1H, $^3J_{HH}$ = 8.4 Hz, arom. H), 6.98–7.01 (m, 2H, arom. H), 7.07 (t, 1H, *J* = 7.8 Hz, arom. H). ^{13}C NMR (100 MHz, CD$_3$CN): σ 15.3 (s, OCH$_2$*C*H$_3$), 63.6 (s, O*C*H$_2$CH$_3$), 113.0 (s), 117.9 (s), 124.7 (s), 128.7 (s), 159.0 (s). ^{19}F NMR (376 MHz, CD$_3$CN): σ −142.7 (br, 3F, BF_3). ^{11}B NMR (128 MHz, CD$_3$CN): σ 4.02 (br). HRMS (FAB), *m*/*z*: calcd. for $C_8H_9OBF_3K_2^+$ 266.9967 [M + K]$^+$; found 266.9975. Elemental analysis calcd. for $C_8H_9OBF_3K$: C, 42.13; H, 3.98; found: C, 42.00; H, 3.98.

Potassium (meta-*n*-propoxyphenyl)trifluoroborate (K[*m*-O^{n}PrC$_6$H$_4$BF$_3$]):

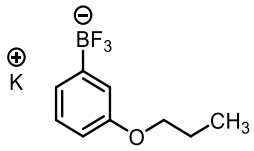

Yield: 90 %, white solid. ^{1}H NMR (400 MHz, CD_3CN): σ 0.98 (t, 3H, $^{3}J_{HH}$ = 7.3 Hz, $OCH_2CH_2CH_3$), 1.71 (m, 2H, J = 7.1 Hz, $OCH_2CH_2CH_3$), 3.88 (t, 2H, $^{3}J_{HH}$ = 6.4 Hz, $OCH_2CH_2CH_3$), 6.66 (d, 1H, $^{3}J_{HH}$ = 6.9 Hz, arom. H), 7.00–7.02 (m, 2H, arom. H), 7.08 (t, 1H, J = 7.6 Hz, arom. H). ^{13}C NMR (100 MHz, CD_3CN): σ 10.9 (s, $OCH_2CH_2CH_3$), 23.5 (s, $OCH_2CH_2CH_3$), 69.8 (s, $OCH_2CH_2CH_3$), 113.0 (s), 118.0 (s), 124.7 (s), 128.8 (s), 159.2 (s). ^{19}F NMR (376 MHz, CD_3CN): σ −142.7 (br, 3F, BF_3). ^{11}B NMR (128 MHz, CD_3CN): σ 4.09 (br). HRMS (FAB), *m*/*z*: calcd. for $C_9H_{11}OBF_3K_2^+$ 281.0124 $[M + K]^+$; found 281.0133. Elemental analysis calcd. for $C_9H_{11}OBF_3K$: C, 44.65; H, 4.58; found: C, 44.43; H, 4.57.

Potassium (meta-*iso*-propoxyphenyl)trifluoroborate (K[*m*-O^{i}PrC$_6$H$_4$BF$_3$]):

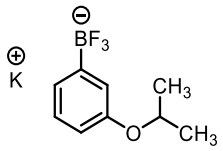

Yield: 74 %, white solid. ^{1}H NMR (400 MHz, CD_3CN): σ 1.23 (d, 6H, $^{3}J_{HH}$ = 6.0 Hz, $OCH(CH_3)_2$), 4.54 (m, 1H, J = 6.1 Hz, $OCH(CH_3)_2$), 6.65 (td, 1H, $^{3}J_{HH}$ = 7.8 Hz, ^{4}J = 1.4 Hz, arom. H), 6.97–7.01 (m, 2H, arom. H), 7.07 (t, 1H, J = 7.6 Hz, arom. H). ^{13}C NMR (100 MHz, CD_3CN): σ 22.5 (s, $OCH(CH_3)_2$), 69.9 (s, $OCH(CH_3)_2$), 114.5 (s), 119.6 (s), 124.7 (s), 128.8 (s), 157.9 (s). ^{19}F NMR (376 MHz, CD_3CN): σ −142.7 (br, 3F, BF_3). ^{11}B NMR (128 MHz, CD_3CN): σ 4.08 (br). HRMS (FAB), *m*/*z*: calcd. for $C_9H_{11}OBF_3K_2^+$ 281.0124 $[M + K]^+$; found 281.0131. Elemental analysis calcd. for $C_9H_{11}OBF_3K$: C, 44.65; H, 4.58; found: C, 43.87; H, 4.71.

Potassium (meta-*n*-butoxyphenyl)trifluoroborate (K[*m*-O^{n}BtC$_6$H$_4$BF$_3$]):

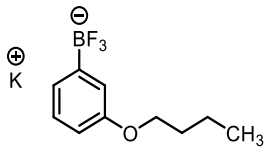

Yield: 73 %, white solid. ^{1}H NMR (400 MHz, CD_3CN): σ 0.93 (t, 3H, $^{3}J_{HH}$ = 7.3 Hz, $OCH_2CH_2CH_2CH_3$), 1.39–1.49 (m, 2H, $OCH_2CH_2CH_2CH_3$), 1.64–1.71 (m, 2H, $OCH_2CH_2CH_2CH_3$), 3.92 (t, 2H, $^{3}J_{HH}$ = 6.6 Hz, $OCH_2CH_2CH_2CH_3$), 6.63 (dd, 1H, $^{3}J_{HH}$ = 7.8 Hz, ^{4}J = 0.92 Hz, arom. H), 6.97–6.99 (m, 2H, arom. H), 7.06 (t, 1H, J = 7.3 Hz, arom. H). ^{13}C NMR (100 MHz, CD_3CN): σ 14.2 (s, $OCH_2CH_2CH_2CH_3$), 20.0 (s, $OCH_2CH_2CH_2CH_3$), 32.3 (s, $OCH_2CH_2CH_2CH_3$), 67.9 (s, $OCH_2CH_2CH_2CH_3$), 112.9 (s), 117.9 (s), 124.7 (s), 128.7 (s), 159.2 (s). ^{19}F NMR (376 MHz, CD_3CN): σ −142.7 (br, 3F, BF_3). ^{11}B NMR (128 MHz, CD_3CN): σ 3.80 (br). HRMS (FAB), *m*/*z*: calcd. for $C_{10}H_{13}OBF_3K_2^+$ 295.0280 $[M + K]^+$; found 295.0296. Elemental analysis calcd. for $C_{10}H_{13}OBF_3K$: C, 46.90; H, 5.12; found: C, 46.87; H, 5.19.

Potassium (meta-*n*-decyloxyphenyl)trifluoroborate (K[*m*-O(CH$_2$)$_9$CH$_3$C$_6$H$_4$BF$_3$]):

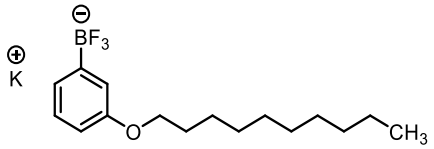

Yield: 46 %, white solid. ^{1}H NMR (400 MHz, CD$_3$CN): σ 0.85 (t, 3H, $^3J_{HH}$ = 6.9 Hz, O(CH$_2$)$_9$C*H$_3$*), 1.26–1.44 (m, 14H, OCH$_2$CH$_2$(C*H$_2$*)$_7$CH$_3$), 1.65–1.72 (m, 2H, OCH$_2$C*H$_2$*(CH$_2$)$_7$CH$_3$), 3.90 (t, 2H, $^3J_{HH}$ = 6.4 Hz, OC*H$_2$*(CH$_2$)$_8$CH$_3$), 6.62 (dd, 1H, $^3J_{HH}$ = 8.0 Hz, ^4J = 2.4 Hz, arom. H), 6.95–6.98 (m, 2H, arom. H), 7.05 (t, 1H, J = 7.6 Hz, arom. H). ^{13}C NMR (100 MHz, CD$_3$CN): σ 14.4 (s, O(CH$_2$)$_9$*C*H$_3$), 23.4 (s, O(CH$_2$)$_8$*C*H$_2$CH$_3$), 26.8 (s, O(CH$_2$)$_7$*C*H$_2$CH$_2$CH$_3$), 30.0–30.4 (m, 5C, OCH$_2$CH$_2$(*C*H$_2$)$_5$CH$_2$CH$_2$CH$_3$), 32.6 (s, OCH$_2$*C*H$_2$(CH$_2$)$_7$CH$_3$), 68.2 (s, O*C*H$_2$(CH$_2$)$_8$CH$_3$), 112.8 (s), 117.9 (s), 124.7 (s), 128.6 (s), 159.2 (s). ^{19}F NMR (376 MHz, CD$_3$CN): σ −142.7 (br, 3F, B*F$_3$*). ^{11}B NMR (128 MHz, CD$_3$CN): σ 3.88 (br). HRMS (FAB), *m*/*z*: calcd. for C$_{16}$H$_{25}$OBF$_3$K$_2^+$ 379.1219 [M + K]$^+$; found 379.1217. Elemental analysis calcd. for C$_{16}$H$_{25}$OBF$_3$K: C, 56.48; H, 7.41; found: C, 56.18; H, 7.61.

Potassium (meta-(2-methoxyethoxy)phenyl)trifluoroborate (K[*m*-O(CH$_2$)$_2$OCH$_3$C$_6$H$_4$BF$_3$]):

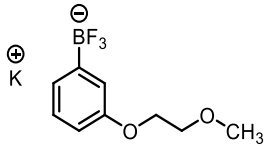

Yield: 47 %, white solid. ^{1}H NMR (400 MHz, CD$_3$CN): σ 3.32 (s, 3H, O(CH$_2$)$_2$OC*H$_3$*), 3.63 (t, 2H, $^3J_{HH}$ = 64.8 Hz, OCH$_2$C*H$_2$*OCH$_3$), 4.03 (t, 2H, $^3J_{HH}$ = 4.8 Hz, OC*H$_2$*CH$_2$OCH$_3$), 6.64 (dd, 1H, $^3J_{HH}$ = 7.8 Hz, ^4J = 2.3 Hz, arom. H), 6.97–7.00 (m, 2H, arom. H), 7.06 (t, 1H, J = 7.8 Hz, arom. H). ^{13}C NMR (100 MHz, CD$_3$CN): σ 59.0 (s), 67.6 (s), 72.0 (s), 112.9 (s), 117.7 (s), 125.0 (s), 128.7 (s), 158.8 (s). ^{19}F NMR (376 MHz, CD$_3$CN): σ −142.8 (d, 3F, $^1J_{BF}$ = 53.2 Hz, B*F$_3$*). ^{11}B NMR (128 MHz, CD$_3$CN): σ 3.71 (d, $^1J_{BF}$ = 46.9 Hz). HRMS (FAB), *m*/*z*: calcd. for C$_9$H$_{11}$O$_2$BF$_3$K$_2^+$ 297.0073 [M + K]$^+$; found 297.0084.

Cesium phenyltrifluoroborate (Cs[PhBF$_3$]):

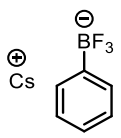

Yield: 89 %, white solid. ^{1}H NMR (400 MHz, CD$_3$CN): σ 7.09 (t, 1H, J = 8.0 Hz, arom. H), 7.15 (t, 2H, J = 7.3 Hz, arom. H), 7.41 (d, 2H, $^3J_{HH}$ = 6.9 Hz, arom. H). ^{13}C NMR (100 MHz,

CD_3CN): σ 126.5 (s), 127.7 (s), 132.3 (s). ^{19}F NMR (376 MHz, CD_3CN): σ −139.0 (q, 3F, $^1J_{BF}$ = 51.4 Hz, B*F*$_3$). ^{11}B NMR (128 MHz, CD_3CN): σ 3.81 (q, $^1J_{BF}$ = 56.2 Hz). HRMS (FAB), *m*/*z*: calcd. for $C_6H_5BF_3Cs_2^+$ 410.8540 $[M + Cs]^+$; found 410.8548. Elemental analysis calcd. for $C_6H_5BF_3Cs$: C, 25.94; H, 1.81; found: C, 25.27; H, 2.04.

Cesium (meta-trifluoromethylphenyl)trifluoroborate (Cs[*m*-$CF_3C_6H_4BF_3$]):

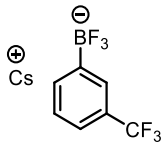

Yield: 99 %, white solid. ^1H NMR (400 MHz, CD_3CN): σ 7.33 (t, 1H, *J* = 7.5 Hz, arom. H), 7.41 (d, 1H, $^3J_{HH}$ = 7.8 Hz), 7.66–7.70 (m, 2H, arom. H). ^{13}C NMR (100 MHz, CD_3CN): σ 123.1 (s), 126.4 (q, $^1J_{CF}$ = 269.8 Hz, *C*F$_3$), 128.1 (s), 128.4 (s), 129.0 (q, $^2J_{CF}$ = 29.6 Hz, *C*CF$_3$), 136.1 (s). ^{19}F NMR (376 MHz, CD_3CN): σ −140.1 (br, 3F, B*F*$_3$), −63.1 (s, 3F, C*F*$_3$). ^{11}B NMR (128 MHz, CD_3CN): σ 3.46 (q, $^1J_{BF}$ = 51.8 Hz). HRMS (FAB), *m*/*z*: calcd. for $C_7H_4BF_6Cs_2^+$ 478.8414 $[M + Cs]^+$; found 478.8412. Elemental analysis calcd. for $C_6H_4BF_4Cs$: C, 24.31; H, 1.17; found: C, 24.10; H, 1.18.

Cesium (meta-fluorophenyl)trifluoroborate (Cs[*m*-$FC_6H_4BF_3$]):

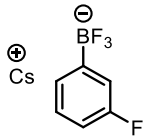

Yield: 99 %, white solid. ^1H NMR (400 MHz, CD_3CN): σ 6.78–6.83 (m, 1H, arom. H), 7.08–7.22 (m, 3H, arom. H). ^{13}C NMR (100 MHz, CD_3CN): σ 112.8 (d, $^2J_{CF}$ = 21.0 Hz), 118.0 (d, $^2J_{CF}$ = 16.2 Hz), 128.0 (s), 129.4 (d, $^3J_{CF}$ = 5.7 Hz), 163.5 (d, $^1J_{CF}$ = 240.3 Hz, *C*F). ^{19}F NMR (376 MHz, CD_3CN): σ −139.8 (q, 3F, $^1J_{BF}$ = 48.4 Hz, B*F*$_3$), −118.1 (s, 1F, 3-*F*). ^{11}B NMR (128 MHz, CD_3CN): σ 3.37 (q, $^1J_{BF}$ = 52.8 Hz). HRMS (FAB), *m*/*z*: calcd. for $C_6H_4BF_4Cs_2^+$ 428.8446 $[M + Cs]^+$; found 428.8453. Elemental analysis calcd. for $C_6H_4BF_4Cs$: C, 24.36; H, 1.36; found: C, 23.73; H, 1.60.

Cesium (meta-trifluoromethoxyphenyl)trifluoroborate (Cs[*m*-$OCF_3C_6H_4BF_3$]):

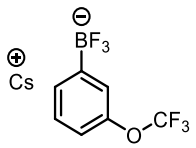

Yield: 62 %, white solid. ^1H NMR (400 MHz, CD_3CN): σ 7.00 (d, 1H, $^3J_{HH}$ = 8.0 Hz, arom. H),

7.24 (t, 1H, J = 7.8 Hz, arom. H), 7.28 (s, 1H, arom. H), 7.40 (d, 1H, $^{3}J_{HH}$ = 7.3 Hz, arom. H). ^{13}C NMR (100 MHz, CD_3CN): σ 119.0 (s), 121.7 (q, $^{1}J_{CF}$ = 252.4 Hz, O*C*F$_3$), 124.1 (s), 129.3 (s), 131.1 (s), 149.5 (s). ^{19}F NMR (376 MHz, CD_3CN): σ −139.8 (q, 3F, $^{1}J_{BF}$ = 57.8 Hz, B*F$_3$*), −58.6 (s, 3F, OC*F$_3$*). ^{11}B NMR (128 MHz, CD_3CN): σ 3.35 (q, $^{1}J_{BF}$ = 50.8 Hz). HRMS (FAB), *m*/*z*: calcd. for $C_7H_4OBF_6Cs_2^+$ 494.8363 [M + Cs]$^+$; found 494.8367. Elemental analysis calcd. for $C_7H_4OBF_6Cs$: C, 23.24; H, 1.11; found: C, 23.07; H, 1.14.

Cesium (meta-methylthiophenyl)trifluoroborate (Cs[*m*-SMeC$_6$H$_4$BF$_3$]):

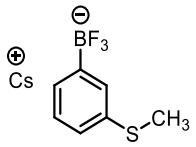

Yield: 94 %, pale brown solid. ^{1}H NMR (400 MHz, CD_3CN): σ 2.41 (s, 3H, SC*H$_3$*), 7.02 (dd, 1H, $^{3}J_{HH}$ = 7.8 Hz, ^{4}J = 0.92 Hz, arom. H), 7.10 (t, 1H, J = 7.3 Hz, arom. H), 7.20 (d, 1H, $^{3}J_{HH}$ = 6.9 Hz, arom. H), 7.33 (s, 1H, arom. H). ^{13}C NMR (100 MHz, CD_3CN): σ 16.0 (s, S*C*H$_3$), 125.0 (s), 128.4 (s), 129.3 (s), 130.6 (s), 136.8 (s). ^{19}F NMR (376 MHz, CD_3CN): σ −139.2 (br, 3F, B*F$_3$*). ^{11}B NMR (128 MHz, CD_3CN): σ 3.60 (q, $^{1}J_{BF}$ = 52.5 Hz). HRMS (FAB), *m*/*z*: calcd. for $C_7H_7SBF_3Cs_2^+$ 456.8417 [M + Cs]$^+$; found 456.8427. Elemental analysis calcd. for $C_7H_7SBF_3Cs$: C, 25.96; H, 2.18; found: C, 26.18; H, 2.27.

Cesium (meta-ethoxyphenyl)trifluoroborate (Cs[*m*-OEtC$_6$H$_4$BF$_3$]):

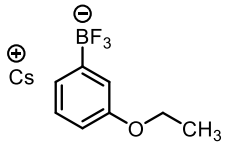

Yield: 96 %, white solid. ^{1}H NMR (400 MHz, CD_3CN): σ 1.30 (t, 3H, $^{3}J_{HH}$ = 7.1 Hz, OCH$_2$C*H$_3$*), 3.98 (q, 2H, $^{3}J_{HH}$ = 6.9 Hz, OC*H$_2$*CH$_3$), 6.62 (d, 1H, $^{3}J_{HH}$ = 7.8 Hz, arom. H), 6.95–6.98 (m, 2H, arom. H), 7.06 (t, 1H, J = 7.6 Hz, arom. H). ^{13}C NMR (100 MHz, CD_3CN): σ 15.3 (s, OCH$_2$*C*H$_3$), 63.6 (s, O*C*H$_2$CH$_3$), 112.9 (s), 117.7 (s), 124.7 (s), 128.7 (s), 159.0 (s). ^{19}F NMR (376 MHz, CD_3CN): σ −138.7 (br, 3F, B*F$_3$*). ^{11}B NMR (128 MHz, CD_3CN): σ 3.70 (d, $^{1}J_{BF}$ = 48.9 Hz). HRMS (FAB), *m*/*z*: calcd. for $C_8H_9OBF_3Cs_2^+$ 454.8802 [M + Cs]$^+$; found 454.8814. Elemental analysis calcd. for $C_8H_9OBF_3Cs$: C, 29.85; H, 2.82; found: C, 29.55; H, 2.97.

Cesium (meta-*n*-propoxyphenyl)trifluoroborate (Cs[*m*-O^{n}PrC$_6$H$_4$BF$_3$]):

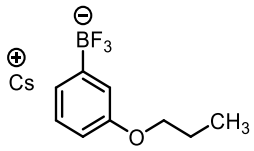

Yield: 96 %, white solid. ^{1}H NMR (400 MHz, CD_3CN): σ 0.97 (t, 3H, $^3J_{HH}$ = 7.3 Hz, $OCH_2CH_2CH_3$), 1.71 (m, 2H, J = 7.1 Hz, $OCH_2CH_2CH_3$), 3.88 (t, 2H, $^3J_{HH}$ = 6.6 Hz, $OCH_2CH_2CH_3$), 6.63 (dd, 1H, $^3J_{HH}$ = 8.0 Hz, ^4J = 1.6 Hz, arom. H), 6.95–6.98 (m, 2H, arom. H), 7.06 (t, 1H, J = 7.6 Hz, arom. H). ^{13}C NMR (100 MHz, CD_3CN): σ 10.8 (s, $OCH_2CH_2CH_3$), 23.5 (s, $OCH_2CH_2CH_3$), 69.7 (s, $OCH_2CH_2CH_3$), 112.9 (s), 117.8 (s), 124.7 (s), 128.7 (s), 159.2 (s). ^{19}F NMR (376 MHz, CD_3CN): σ −138.5 (br, 3F, BF_3). ^{11}B NMR (128 MHz, CD_3CN): σ 3.72 (d, $^1J_{BF}$ = 48.9 Hz). HRMS (FAB), *m*/*z*: calcd. for $C_9H_{11}OBF_3Cs_2^+$ 468.8959 $[M + Cs]^+$; found 468.8966. Elemental analysis calcd. for $C_9H_{11}OBF_3Cs$: C,32.18; H, 3.30; found: C, 31.49; H, 3.22.

Potassium (ortho-fluorophenyl)trifluoroborate (K[*o*-FC$_6$H$_4$BF$_3$]):

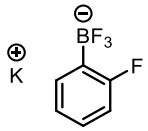

Yield: 79 %, white solid. ^{1}H NMR (400 MHz, CD_3CN): σ 6.83 (t, 1H, J = 8.9 Hz, arom. H), 6.97 (t, 1H, J = 7.3 Hz, arom. H), 7.10–7.15 (m, 1H, arom. H), 7.42 (t, 1H, J = 6.2 Hz, arom. H). ^{13}C NMR (100 MHz, CD_3CN): σ 114.7 (d, $^2J_{CF}$ = 25.9 Hz), 123.9 (s), 128.8 (d, $^3J_{CF}$ = 7.7 Hz), 135.0 (d, $^3J_{CF}$ = 10.5 Hz), 167.0 (d, $^1J_{BF}$ = 237.6 Hz). ^{19}F NMR (376 MHz, CD_3CN): σ −140.8 (q, 3F, $^1J_{BF}$ = 49.6 Hz, BF_3), −110.8 (s, 1F, 2-*F*). ^{11}B NMR (128 MHz, CD_3CN): σ 3.18 (q, $^1J_{BF}$ = 51.3 Hz). HRMS (FAB), *m*/*z*: calcd. for $C_6H_4BF_4K_2^+$ 240.9611 $[M + K]^+$; found 240.9613. Elemental analysis calcd. for $C_6H_4BF_4K$: C, 35.68; H, 2.00; found: C, 34.92; H, 1.99.

Potassium (ortho-trifluoromethoxyphenyl)trifluoroborate (K[*o*-OCF$_3$C$_6$H$_4$BF$_3$]):

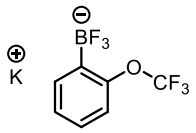

Yield: 80 %, white solid. ^{1}H NMR (400 MHz, CD_3CN): σ 7.07 (d, 1H, $^3J_{HH}$ = 7.8 Hz, arom. H), 7.12–7.20 (m, 2H, arom. H), 7.53 (d, 1H, $^3J_{HH}$ = 6.9 Hz, arom. H). ^{13}C NMR (100 MHz, CD_3CN): σ 119.9 (s), 121.9 (q, $^1J_{CF}$ = 253.9 Hz, OCF_3), 126.7 (s), 128.4 (s), 135.3 (s), 153.5 (s). ^{19}F NMR (376 MHz, CD_3CN): σ −141.0 (q, 3F, $^1J_{BF}$ = 48.9 Hz, BF_3), −56.5 (s, 3F, OCF_3). ^{11}B NMR (128 MHz, CD_3CN): σ 2.99 (q, $^1J_{BF}$ = 50.8 Hz). HRMS (FAB), *m*/*z*: calcd. for $C_7H_4OBF_6K_2^+$ 306.9528 $[M + K]^+$; found 306.9535. Elemental analysis calcd. for $C_7H_4OBF_6K$:

C, 31.37; H, 1.50; found: C, 30.91; H, 1.71.

Potassium (ortho-methylthiophenyl)trifluoroborate (K[*o*-SMeC$_6$H$_4$BF$_3$]):

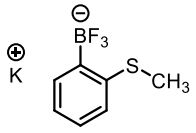

Yield: 70 %, white solid. ^{1}H NMR (400 MHz, CD_3CN): σ 2.32 (s, 3H, SC*H*$_3$), 6.91 (t, 1H, J = 7.6 Hz, arom. H), 7.02–7.10 (m, 2H, arom. H), 7.40 (d, 1H, $^3J_{HH}$ = 6.9 Hz, arom. H). ^{13}C NMR (100 MHz, CD_3CN): σ 15.6 (s, S*C*H$_3$), 123.9 (s), 124.1 (s), 127.5 (s), 133.1 (s), 142.6 (s). ^{19}F NMR (376 MHz, CD_3CN): σ −140.4 (q, 3F, $^1J_{BF}$ = 52.4 Hz, B*F*$_3$). ^{11}B NMR (128 MHz, CD_3CN): σ 3.37 (q, $^1J_{BF}$ = 53.7 Hz). HRMS (FAB), *m*/*z*: calcd. for $C_7H_7SBF_3K_2^+$ 268.9582 [M + K]$^+$; found 268.9586. Elemental analysis calcd. for $C_7H_7SBF_3K$: C, 36.54; H, 3.07; found: C, 36.27; H, 3.12.

Potassium (ortho-methoxyphenyl)trifluoroborate (K[*o*-OMeC$_6$H$_4$BF$_3$]):

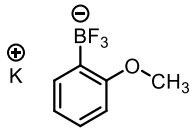

Yield: 84%, white solid. ^{1}H NMR (400 MHz, CD_3CN): σ 3.68 (s, 3H, OC*H*$_3$), 6.74–6.77 (m, 2H, arom. H), 7.08 (dt, 1H, J = 7.8 Hz, ^4J = 1.8 Hz, arom. H), 7.36 (d, 1H, $^3J_{HH}$ = 6.4 Hz, arom. H). ^{13}C NMR (100 MHz, DMSO-d^6): σ 54.7 (s, O*C*H$_3$), 109.6 (s), 119.1 (s), 126.7 (s), 133.2 (s), 162.5 (s). ^{19}F NMR (376 MHz, CD_3CN): σ −140.6 (q, 3F, $^1J_{BF}$ = 53.0 Hz, B*F*$_3$). ^{11}B NMR (128 MHz, CD_3CN): σ 3.43 (d, $^1J_{BF}$ = 54.2 Hz). HRMS (FAB), *m*/*z*: calcd. for $C_7H_7OBF_3K_2^+$ 252.9811 [M + K]$^+$; found 252.9818. Elemental analysis calcd. for $C_7H_7OBF_3K$: C, 39.28; H, 3.30; found: C, 39.15; H, 3.32.

Potassium (ortho-ethoxyphenyl)trifluoroborate (K[*o*-OEtC$_6$H$_4$BF$_3$]):

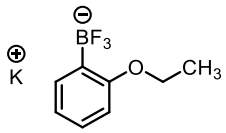

Yield: 82 %, white solid. ^{1}H NMR (400 MHz, CD_3CN): σ 1.28 (t, 3H, $^3J_{HH}$ = 7.1 Hz, OCH$_2$C*H*$_3$), 3.99 (q, 2H, $^3J_{HH}$ = 7.1 Hz, OC*H*$_2$CH$_3$), 6.75–6.79 (m, 2H, arom. H), 7.08 (dt, 1H, J = 7.8 Hz, ^4J = 1.9 Hz, arom. H), 7.38 (dd, 1H, J = 7.2 Hz, ^4J = 1.2 Hz, arom. H). ^{13}C NMR (100 MHz, CD_3CN): σ 15.3 (s, OCH$_2$*C*H$_3$), 64.3 (s, O*C*H$_2$CH$_3$), 112.5 (s), 120.8 (s), 128.3 (s), 134.4 (s), 162.7 (s). ^{19}F NMR (376 MHz, CD_3CN): σ −140.4 (d, 3F, $^1J_{BF}$ = 58.9 Hz, B*F*$_3$). ^{11}B NMR (128 MHz, CD_3CN): σ 3.67 (d, $^1J_{BF}$ = 48.8 Hz). HRMS (FAB), *m*/*z*: calcd. for $C_8H_9OBF_3K_2^+$

266.9967 [M + K]$^+$; found 266.9979. Elemental analysis calcd. for $C_8H_9OBF_3K$: C, 42.13; H, 3.98; found: C, 41.89; H, 3.82.

Potassium (ortho-nitrophenyl)trifluoroborate (K[*o*-$NO_2C_6H_4BF_3$]):

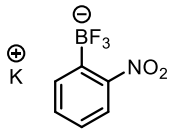

Yield: 82 %, gray solid. ^{1}H NMR (400 MHz, CD_3CN): σ 7.27 (dt, 1H, J = 7.7 Hz, ^4J = 1.3 Hz, arom. H), 7.39–7.45 (m, 2H, arom. H), 7.64 (d, 1H, $^3J_{HH}$ = 7.3 Hz, arom. H). ^{13}C NMR (100 MHz, CD_3CN): σ 122.5 (s), 127.9 (s), 131.5 (s), 135.2 (s), 156.0 (s). ^{19}F NMR (376 MHz, CD_3CN): σ −141.8 (q, 3F, $^1J_{BF}$ = 46.3 Hz, B*F*$_3$). ^{11}B NMR (128 MHz, CD_3CN): σ 2.76 (q, $^1J_{BF}$ = 48.4 Hz). HRMS (FAB), *m*/*z*: calcd. for $C_6H_4NO_2BF_3K_2^+$ 267.9556 [M + K]$^+$; found 267.9566. Elemental analysis calcd. for $C_6H_4NO_2BF_3K$: C, 31.47; H, 1.76; N, 6.12; found: C, 31.47; H, 2.07; N, 6.11.

Potassium (ortho-acetylphenyl)trifluoroborate (K[*o*-$COCH_3C_6H_4BF_3$]):

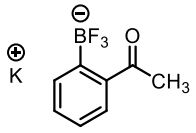

Yield: 55 %, white solid. ^{1}H NMR (400 MHz, CD_3CN): σ 2.45 (s, 3H, COC*H*$_3$), 7.13–7.15 (m, 2H, arom. H), 7.21–7.25 (m, 1H, arom. H), 7.53 (d, 1H, $^3J_{HH}$ = 7.2 Hz, arom. H). ^{13}C NMR (100 MHz, CD_3CN): σ 31.3 (s, CO*C*H$_3$), 125.6 (s), 126.5 (s), 129.3 (s), 133.7 (s), 146.9 (s), 210.2 (s, *C*OCH$_3$). ^{19}F NMR (376 MHz, CD_3CN): σ −138.5 (q, 3F, $^1J_{BF}$ = 51.0 Hz, B*F*$_3$). ^{11}B NMR (128 MHz, CD_3CN): σ 3.44 (q, $^1J_{BF}$ = 53.2 Hz). HRMS (FAB), *m*/*z*: calcd. for $C_8H_7OBF_3K_2^+$ 264.9811 [M + K]$^+$; found 264.9819. Elemental analysis calcd. for $C_8H_7OBF_3K$: C, 42.51; H, 3.12; found: C, 42.60; H, 3.18.

Potassium (2-fluoro-5-methoxyphenyl)trifluoroborate (K[2-F-5-$OMeC_6H_3BF_3$]):

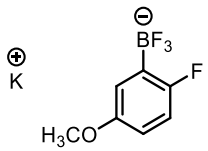

Yield: 90 %, white solid. ^{1}H NMR (400 MHz, CD_3CN): σ 3.96 (s, 3H, OC*H*$_3$), 6.60–6.65 (m, 1H, arom. H), 6.75 (t, 1H, J = 8.7 Hz, arom. H), 6.93–6.95 (m, 1H, arom. H). ^{13}C NMR (100 MHz, CD_3CN): σ 56.0 (s, O*C*H$_3$), 113.5 (d, $^3J_{CF}$ = 9.6 Hz), 115.3 (d, $^2J_{CF}$ = 29.7 Hz), 119.3 (d, $^3J_{CF}$ = 12.9 Hz), 156.1 (s), 161.3 (d, $^1J_{CF}$ = 229.9 Hz). ^{19}F NMR (376 MHz, CD_3CN): σ −141.0

(d, 3F, $^{1}J_{BF}$ = 53.2 Hz, B*F*$_3$), −122.7 (s, 1F, 2-*F*). ^{11}B NMR (128 MHz, CD_3CN): σ 3.06 (d, $^{1}J_{BF}$ = 48.8 Hz). HRMS (FAB), *m*/*z*: calcd. for $C_7H_6OBF_4K_2^+$ 270.9716 $[M + K]^+$; found 270.9727. Elemental analysis calcd. for $C_7H_6OBF_4K$: C, 36.24; H, 2.61; found: C, 36.08; H, 2.82.

Potassium (2-chloro-5-trifluoromethylphenyl)trifluoroborate (K[2-Cl-5-$CF_3C_6H_3BF_3$]):

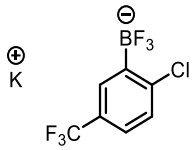

Yield: 85 %, white solid. ^{1}H NMR (400 MHz, DMSO-*d*^{6}): σ 7.36 (d, 1H, $^{3}J_{HH}$ = 8.2 Hz, arom. H), 7.42 (dd, 1H, $^{3}J_{HH}$ = 8.2 Hz, ^{4}J = 2.3 Hz, arom. H), 7.70 (s, 1H, arom. H). ^{13}C NMR (100 MHz, DMSO-*d*^{6}): σ 124.0 (q, $^{3}J_{CF}$ = 3.3 Hz), 124.8 (q, $^{1}J_{CF}$ = 270.5 Hz, *C*F$_3$), 125.8 (q, $^{2}J_{CF}$ = 30.3 Hz), 129.0 (s), 130.1 (q, $^{3}J_{CF}$ = 3.1 Hz), 141.9 (s). ^{19}F NMR (376 MHz, DMSO-*d*^{6}): σ −142.2 (br, 3F, B*F*$_3$), −63.3 (s, 3F, C*F*$_3$). ^{11}B NMR (128 MHz, DMSO-*d*^{6}): σ 2.59 (d, $^{1}J_{BF}$ = 45.0 Hz). HRMS (FAB), *m*/*z*: calcd. for $C_7H_3ClBF_6K_2^+$ 324.9189 $[M + K]^+$; found 324.9191. Elemental analysis calcd. for $C_7H_3ClBF_6K$: C, 29.35; H, 1.06; found: C, 29.80; H, 1.26.

Potassium (3-methoxycarbonyl-5-nitrophenyl)trifluoroborate (K[3-CO_2Me-5-$NO_2C_6H_3BF_3$]):

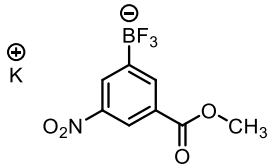

Yield: 73%, white solid. ^{1}H NMR (400 MHz, DMSO-*d*^{6}): σ 3.91 (s, 3H, CO_2CH_3), 8.35 (br, 2H, arom. H), 8.44 (s, 1H, arom. H). ^{13}C NMR (100 MHz, DMSO-*d*^{6}): σ 52.5 (s, CO_2CH_3), 121.0 (s), 129.4 (s), 129.5 (s), 138.1 (s), 147.1 (s), 165.6 (s, CO_2CH_3). ^{19}F NMR (376 MHz, DMSO-*d*^{6}): σ −143.3 (br, 3F, B*F*$_3$). ^{11}B NMR (128 MHz, DMSO-*d*^{6}): σ 2.87 (br). HRMS (FAB), *m*/*z*: calcd. for $C_8H_6NO_4BF_3K_2^+$ 325.9611 $[M + K]^+$; found 325.9612. Elemental analysis calcd. for $C_8H_6NO_4BF_3K$: C, 33.48; H, 2.11; N, 4.88; found: C, 33.32; H, 2.36; N, 6.03.

Potassium 3-thienyltrifluoroborate (K[3-$C_4H_3SBF_3$]):

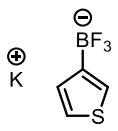

Yield: 97 %, gray solid ^{1}H NMR (400 MHz, DMSO-*d*^{6}): σ 6.97–7.00 (m, 2H, arom. H), 7.16–7.18 (m, 1H, arom. H). ^{13}C NMR (100 MHz, DMSO-*d*^{6}): σ 122.5 (s), 124.2 (s), 131.9 (s). ^{19}F

NMR (376 MHz, DMSO-d^6): σ −138.0 (q, 3F, $^1J_{BF}$ = 52.0 Hz, BF_3). ^{11}B NMR (128 MHz, DMSO-d^6): σ 2.96 (q, $^1J_{BF}$ = 50.8 Hz). HRMS (FAB), *m*/*z*: calcd. for $C_4H_3SBF_3K_2^+$ 228.9269 $[M + K]^+$; found 228.9282. Elemental analysis calcd. for $C_4H_3SBF_3K$: C, 25.28; H, 1.59; found: C, 25.08; H, 1.85.

Potassium 1-naphthyltrifluoroborate (K[1-NaphBF$_3$]):

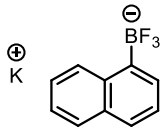

Yield: 81 %, pale brown solid ^{1}H NMR (400 MHz, DMSO-d^6): σ 7.26–7.32 (m, 3H, arom. H), 7.55–7.59 (m, 2H, arom. H), 7.70–7.72 (m, 1H, arom. H), 8.39 (d, 1H, $^3J_{HH}$ = 8.7 Hz). ^{13}C NMR (100 MHz, DMSO-d^6): σ 123.5 (s), 124.0 (s), 125.0 (s), 125.3 (s), 127.5 (s), 128.6 (d, J_{CF} = 2.9 Hz), 130.3 (s), 133.0 (s), 136.6 (s). ^{19}F NMR (376 MHz, DMSO-d^6): σ −137.7 (d, 3F, $^1J_{BF}$ = 44.8 Hz, BF_3). ^{11}B NMR (128 MHz, DMSO-d^6): σ 4.12 (d, $^1J_{BF}$ = 46.9 Hz). HRMS (FAB), *m*/*z*: calcd. for $C_{10}H_7BF_3K_2^+$ 272.9862 $[M + K]^+$; found 272.9868. Elemental analysis calcd. for $C_{10}H_7BF_3K$: C, 51.31; H, 3.01; found: C, 50.56; H, 2.90.

Chapter 2 Physicochemical Properties for Room Temperature Ionic Liquids with Phenyltrifluoroborate Anion

2.1. Introduction

Room temperature ionic liquids (RTILs) are a subset of molten salts that possess unique features, such as negligible vapor pressures, incombustibility, wide electrochemical windows (EWs), and relatively high ionic conductivities.[1, 64-72] The features of RTILs, except for the handling temperatures, are very similar to those of molten salts. In the past several decades, numerous cations and anions have been used to prepare various functional RTILs as shown in General Introduction.[7, 8] The physicochemical properties of RTILs strongly depend on the combination of the cation and anion.[12-16, 73, 74] Thus, RTILs with $[ArBF_3]^-$ synthesized in Chapter 1 are likely to have favorable physicochemical properties because of the distinctive anion structure.[75-83] In this chapter, in order to observe the influence of different organic cation's structures on the properties of RTILs, the author produced undiscovered RTILs by combining different onium cations, e.g., imidazolium, pyridinium, pyrrolidinium, piperidinium, and quaternary ammonium, with the phenyltrifluoroborate ($[PhBF_3]^-$) anion, which has the simplest structure among the $[ArBF_3]^-$ anions. The physicochemical properties of the resulting $[PhBF_3]^-$-based salts were examined. The factors controlling their properties were explored via systematic data gathering.

2.2. Experimental

2.2.1. Preparation of phenyltrifluoroborate-based RTILs

Seven kinds of onium salts, 1-ethyl-3-methylimidazolium chloride ($[C_2mim]Cl$) (Tokyo Chemical Industry Co., Ltd.), 1-butyl-3-methylimidazolium chloride ($[C_4mim]Cl$) (Kanto Chemical Co., Inc.), 1-butylpyridinium chloride ($[C_4py]Cl$) (Tokyo Chemical Industry Co., Ltd.), 1-butyl-1-methylpyrrolidinium chloride ($[C_4mpyr]Cl$) (Sigma-Aldrich, Inc.), 1-butyl-1-methylpiperidinium chloride ($[C_4mpip]Cl$) (Tokyo Chemical Industry Co., Ltd.), trimethylpropylammonium bromide ($[N_{1,1,1,3}]Br$) (Tokyo Chemical Industry Co., Ltd.), and tributylmethylammonium chloride ($[N_{4,4,4,1}]Cl$) (Sigma-Aldrich, Inc.) were used as the cationic species for the preparation of the $[PhBF_3]^-$-based organic salts. $K[PhBF_3]$ prepared via the almost same protocols described in Chapter 1 was used as the anion source. The synthesis of

the $[PhBF_3]^-$-based organic salts was performed using the metathesis protocol explained below. $K[PhBF_3]$ (40 mmol) was added to a solution of an onium halide (40 mmol) in acetonitrile (60 mL), and the mixture was stirred for 1 h at ambient temperature. After the reaction, the mixture was filtered to remove the precipitated by-product, KCl or KBr, and the filtrate was condensed under vacuum. The crude product was extracted by CH_2Cl_2 and rinsed with ultrapure water several times to remove the unreacted halides and by-product. The organic layer was concentrated in vacuo. The resultant onium phenyltrifluoroborate was dried at 373 K under vacuum for 12 h. The final product was confirmed by NMR spectroscopy, mass spectrometry, and elemental analysis. 1-Butyl-3-methylimidazolium tetrafluoroborate ($[C_4mim][BF_4]$) was purchased from Kanto Chemical Co. and used for comparison and was thoroughly vacuum dried for 24 h before use to remove any residual water.

2.2.2. Thermal and physicochemical property measurements

Thermal properties for phenyltrifluoroborate-based salts were measured in the same manner described in Chapter 1. Thermogravimetric (TG) analyses were performed using a Bruker TG-DTA2000SA instrument and differential scanning calorimetry (DSC) was conducted using a Bruker DSC3100SA instrument. These two instruments were controlled with a Bruker MTC1000SA workstation utilizing the Bruker WS003 software.

Density measurements were conducted using a Kyoto Electronics Manufacturing DA-640 resonant frequency oscillation density/specific gravity meter in the range of 298–353 K. The viscosity was measured using a Kyoto Electronics Manufacturing EMS-1000 electromagnetically spinning viscometer in the range of 298–353 K. Ionic conductivity measurements were performed using a Horiba DS-51 digital conductivity meter in the range of 303–353 K with a glass conductivity cell after the cell was calibrated with a 0.1 M KCl aqueous solution. All the measurements, except the viscosity, were performed in an argon-filled glove box (Vacuum Atmospheres Co., Omni-Lab, O_2 and $H_2O < 1$ ppm). The viscosity measurements were performed using the special airtight cells for the electromagnetically spinning viscometer.

2.2.3. Electrochemical measurements

The electrochemical measurements were conducted with an IVIUM Technologies CompactStat portable electrochemical analyzer. All electrochemical experiments were performed in a three-electrode cell. The working electrode was a glassy carbon disk (diameter of 1.6 mm), which was polished with an alumina suspension (diameter of 0.06 μm) prior to use. A platinum wire (diameter of 0.5 mm) was used as the counter electrode, and the reference electrode was constructed by placing a 1.0 mm diameter Ag wire into a 6 mm diameter Vycor® glass tube filled with a $[C_4mim][N(SO_2CF_3)_2]$ RTIL containing 0.05 M $Ag[N(SO_2CF_3)_2]$. The measurements were performed in an abovementioned argon-filled glove box.

2.2.4. Computational methods

The Gaussian 09 program[36] was used for the molecular orbital calculations. The author used the basis sets implemented in the Gaussian program. All the ion structures used in this study were optimized at the HF/6-311G(d,p) level. The ionic volumes of the cations and anions were calculated at the B3LYP/6-31G+(d) level.[16] The author determined the ionic volume using the average value from 10 calculations.

2.3. Results and discussion

2.3.1. General characteristics

The chemical structures of the organic salts prepared in this study are summarized in Figure 2-1 with their abbreviations. The author successfully synthesized seven types of $[PhBF_3]^-$-based organic salts. All the salts, except $[N_{1,1,1,3}][PhBF_3]$, were liquid salts at room temperature. $K[PhBF_3]$ has a melting point of 568 K, but the cation exchange of K^+ for the organic cations caused a sudden drop in the melting point due to the larger cation size and the asymmetric

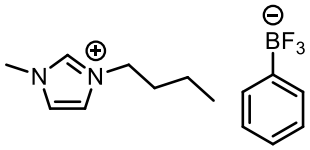

1-butyl-3-methylimidazolium phenyltrifluoroborate ($[C_4mim][PhBF_3]$)

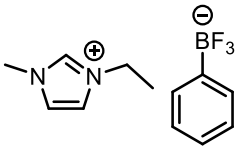

1-ethyl-3-methylimidazolium phenyltrifluoroborate ($[C_2mim][PhBF_3]$)

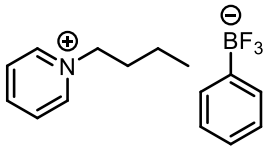

1-butylpyridinium phenyltrifluoroborate ($[C_4py][PhBF_3]$)

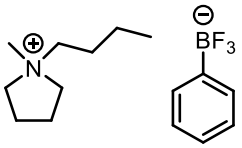

1-butyl-1-methylpyrrolidinium phenyltrifluoroborate ($[C_4mpyr][PhBF_3]$)

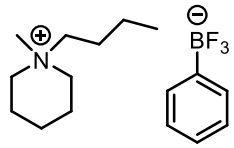

1-butyl-1-methylpiperidinium phenyltrifluoroborate ($[C_4mpip][PhBF_3]$)

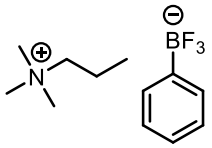

trimethylpropylammonium phenyltrifluoroborate ($[N_{1,1,1,3}][PhBF_3]$)

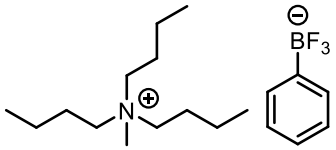

tributylmethylammonium phenyltrifluoroborate ($[N_{4,4,4,1}][PhBF_3]$)

Figure 2-1. Chemical structures of $[PhBF_3]^-$-based RTILs with different organic cations and their abbreviations.

structure of the organic cations. The resulting organic salts were stable in air without any undesirable reactions with oxygen and moisture even though they were moderately hygroscopic. All the salts had a lower water miscibility than the salts with $[BF_4]^-$, and the hydrophobic phenyl group in $[PhBF_3]^-$ causes this characteristics.

2.3.2. Thermal behavior

The TG analysis results for the $[PhBF_3]^-$-based salts are shown in Figure 2-2 along with the results for $[C_4mim][BF_4]$ as a comparison. The thermal degradation temperatures determined at a 5 wt% loss are given in Table 2-1. All the salts exhibited clear weight losses at temperatures in the range from 477–514 K, and their thermal stabilities were inferior to that of $[C_4mim][BF_4]$. This result is attributed to the $[PhBF_3]^-$ anion containing a B–C bond because the bond dissociation energy of the B–C bond (92 kcal·mol^{-1}) is smaller than that of the B–F bond (181 kcal·mol^{-1}) in $[BF_4]^-$.[84] The TG curves also indicated that the thermal degradation reaction proceeds via multiple steps, whereas $[C_4mim][BF_4]$ showed a simple one-step curve. As expected, the weight losses observed for the first one or two steps were very close to the wt% of the $[PhBF_3]^-$ in the original RTILs, e.g., 51 wt% in $[C_4mim][PhBF_3]$ and 56 wt% in $[C_2mim][PhBF_3]$. The DSC curves for the same RTILs are given in Figure 2-3. Almost all the salts showed a glass-transition temperature (T_g) at 208–228 K, but they did not show significant crystallization or melting behaviors, except for $[N_{1,1,1,3}][PhBF_3]$, which showed a sharp

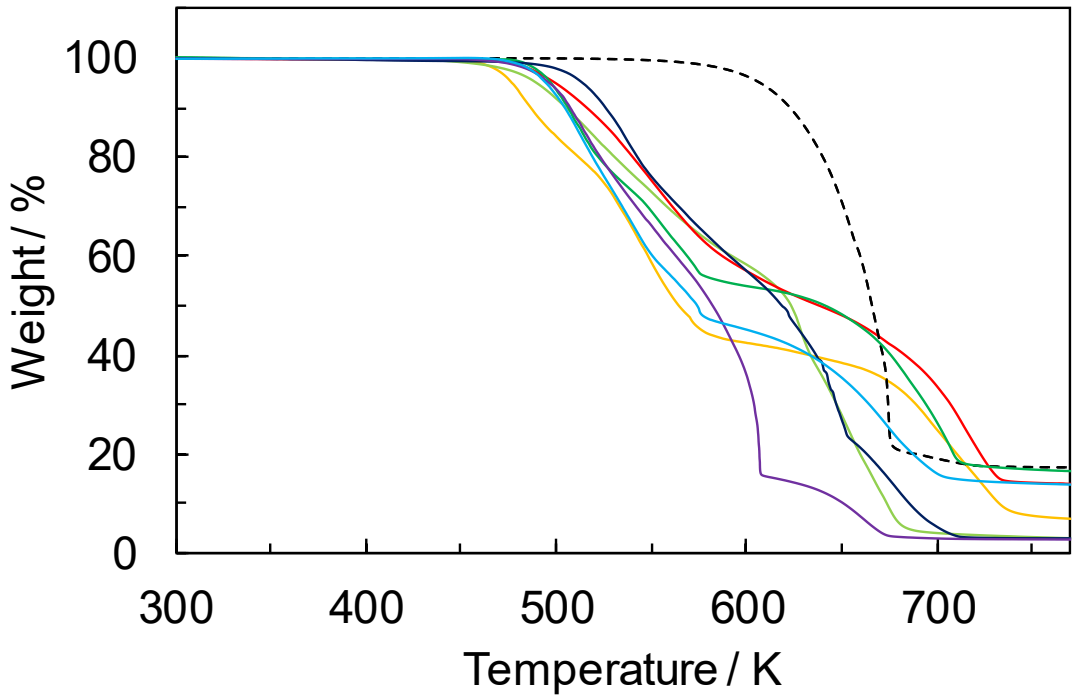

Figure 2-2. Results of the TG analysis for (---) $[C_4mim][BF_4]$, (—) $[C_4mim][PhBF_3]$, (—) $[C_2mim][PhBF_3]$, (—) $[C_4py][PhBF_3]$, (—) $[C_4mpyr][PhBF_3]$, (—) $[C_4mpip][PhBF_3]$, (—) $[N_{1,1,1,3}][PhBF_3]$, and (—) $[N_{4,4,4,1}][PhBF_3]$. The measurements were conducted at a rate of 5 K·min^{-1}.

exothermic peak in the cooling process at ca. 313 K and a noticeable endothermic peak in the heating process at 353 K without any glass-transition behavior (Figure 2-3g). In the case of [C_4mpy][$PhBF_3$] and [$N_{4,4,4,1}$][$PhBF_3$], small crystallization and melting behaviors were observed (Fig. 3e and h). These behaviors are induced by the very slow dynamics derived from the unique properties of RTILs.[85, 86] Unfortunately, certain information about such phase transitions could only be obtained using a specially manufactured DSC at this time.[87]

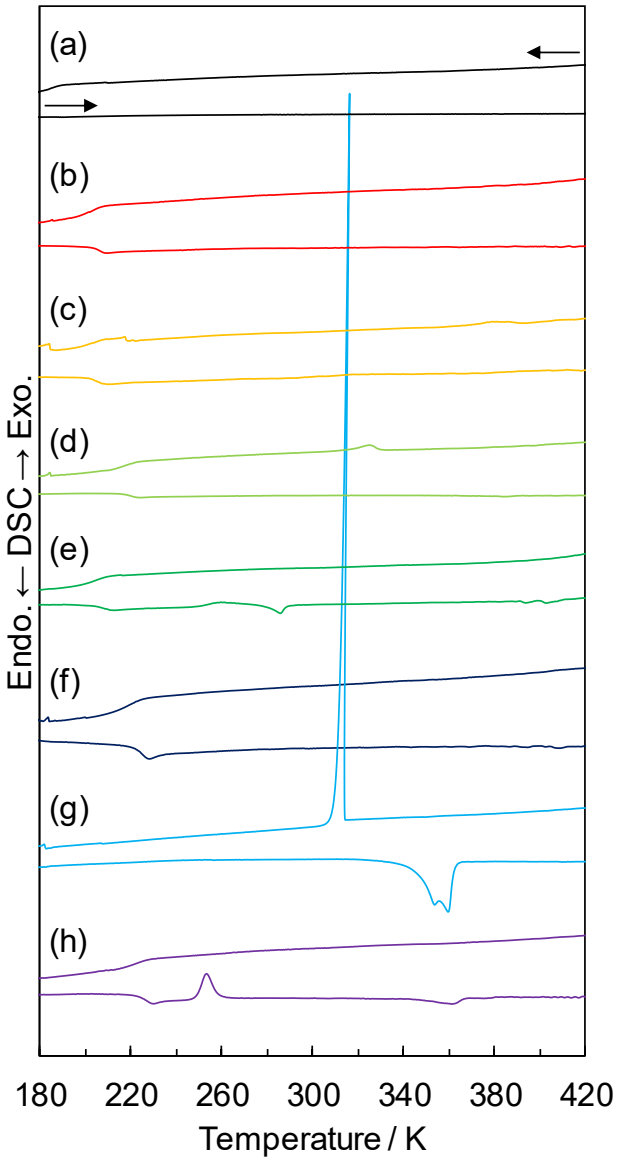

Figure 2-3. DSC curves of (a) [C_4mim][BF_4], (b) [C_4mim][$PhBF_3$], (c) [C_2mim][$PhBF_3$], (d) [C_4py][$PhBF_3$], (e) [C_4mpyr][$PhBF_3$], (f) [C_4mpip][$PhBF_3$], (g) [$N_{1,1,1,3}$][$PhBF_3$], and (h) [$N_{4,4,4,1}$][$PhBF_3$]. The measurements were conducted at a rate of 5 $K \cdot min^{-1}$.

Table 2-1. Physicochemical properties of $[PhBF_3]^-$-based RTILs and salt

RTILs and salt	FW [a]	T_g [b] / K	T_m [c] / K	T_d [d] / K	d [e] / g·cm^{-3}	η [f] / mPa·s	σ [g] / mS·cm^{-1}	Λ [h] / S·cm^2·mol^{-1}	V_{cation} [i] / nm^3	V_{anion} [j] / nm^3
$[C_4mim][BF_4]$	226	190	—	611	1.201	101	4.21	0.795	0.207	0.072
$[C_4mim][PhBF_3]$	284	209	—	492	1.145	115	2.42	0.602	0.207	0.164
$[C_2mim][PhBF_3]$	255	210	—	477	1.192	60	7.09	1.54	0.160	0.164
$[C_4py][PhBF_3]$	281	224	—	490	1.151	131	2.20	0.539	0.203	0.164
$[C_4mpyr][PhBF_3]$	287	208	—	497	1.114	241	1.44	0.371	0.211	0.164
$[C_4mpip][PhBF_3]$	301	228	—	514	1.108	1150	0.328	0.0895	0.231	0.164
$[N_{1,1,1,3}][PhBF_3]$	274	—	350	495	—	—	—	—	0.160	0.164
$[N_{4,4,4,1}][PhBF_3]$	345	227	—	496	1.028	1870	0.112	0.0377	0.319	0.164

[a] Formula weight. [b] Glass-transition temperature. [c] Melting point. [d] Thermal degradation temperature at 5 wt% loss. [e] Density at 298 K. [f] Viscosity at 298 K. [g] Ionic conductivity at 303 K. [h] Equivalent conductivity at 303 K. [i] Volume of the cation. [j] Volume of the anion. The ionic volume was calculated with the Gaussian 09 program using a B3LYP/6–31G+(d) level calculation.

2.3.3. Physicochemical properties

The density data for the $[PhBF_3]^-$-based RTILs at 298 K are given in Table 2-1 along with other physicochemical properties. The temperature dependence of the density (d) of the $[PhBF_3]^-$-based RTILs is shown in Figure 2-4. The solid lines depicted in the figure are straight lines that were calculated using the least-squares method. In general, density can be represented as a function of absolute temperature by the following equation:

$$d = a + bT \tag{2-1}$$

where a is the density at 0 K ($g \cdot cm^{-3}$), b is a volume expansion coefficient ($g \cdot cm^{-3} \cdot K^{-1}$), and T is the absolute temperature (K). The results fitted by the least-squares method are summarized in Table 2-2. The correlation coefficient ($|R|$) indicates the precision of the fitting. The densities of the $[PhBF_3]^-$-based liquid salts were 1.028–1.192 $g \cdot cm^{-3}$ at 298 K (Table 2-1), and these values were closely related to the cationic volume. The ascending order of the cation volume based on the B3LYP/6-31G+(d) level calculations using the Gaussian 09 program[36] is $[C_2mim]^+$ (0.160 nm^3) < $[C_4py]^+$ (0.203 nm^3) < $[C_4mim]^+$ (0.207 nm^3) < $[C_4mpyr]^+$ (0.211 nm^3) < $[C_4mpip]^+$ (0.231 nm^3) < $[N_{4,4,4,1}]^+$ (0.319 nm^3), and this order coincides with the descending order of the density. Several research groups have concluded that the molecular volumes of

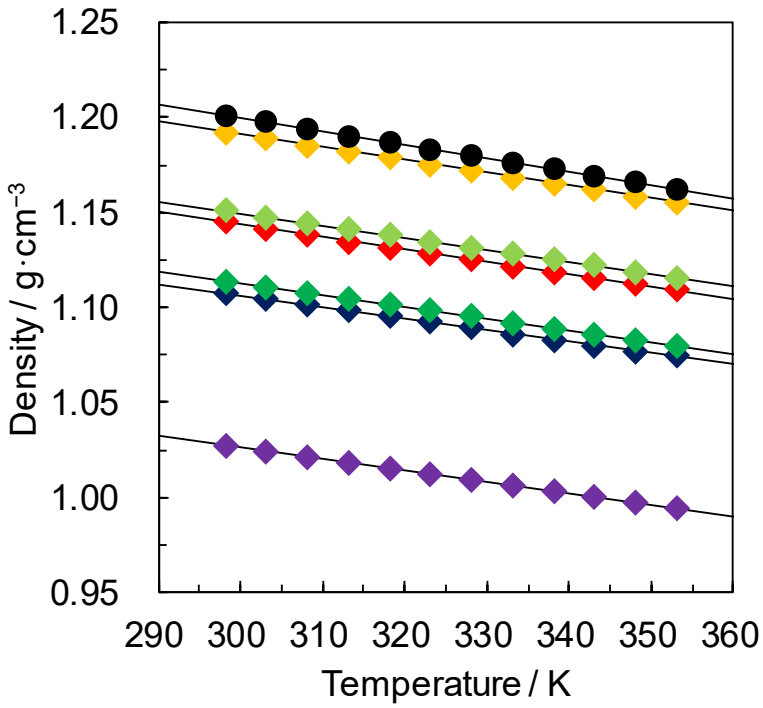

Figure 2-4. Temperature dependence of the density for (●) $[C_4mim][BF_4]$, (◆) $[C_4mim][PhBF_3]$, (◆) $[C_2mim][PhBF_3]$, (◆) $[C_4py][PhBF_3]$, (◆) $[C_4mpyr][PhBF_3]$, (◆) $[C_4mpip][PhBF_3]$, and (◆) $[N_{4,4,4,1}][PhBF_3]$. The solid lines depicted on each plot are the approximate lines calculated using the least-square method.

RTILs are related to some of their physicochemical parameters, e.g., density, viscosity, melting point, and dielectric constant.[88-90] As the author will discuss later, a similar relationship was also observed in my RTILs.

Table 2-2. Fitted parameters for the density of the RTILs with various cations

RTILs	a / g·cm^{-3}	$b \times 10^4$ / g·cm^{-3}·K^{-1}	$\|R\|$
[C$_4$mim][BF$_4$]	1.413	−7.113	> 0.9999
[C$_4$mim][PhBF$_3$]	1.339	−6.510	> 0.9999
[C$_2$mim][PhBF$_3$]	1.392	−6.711	> 0.9999
[C$_4$py][PhBF$_3$]	1.340	−6.362	> 0.9999
[C$_4$mpyr][PhBF$_3$]	1.297	−6.136	> 0.9999
[C$_4$mpip][PhBF$_3$]	1.288	−6.048	> 0.9999
[N$_{4,4,4,1}$][PhBF$_3$]	1.207	−6.020	> 0.9999

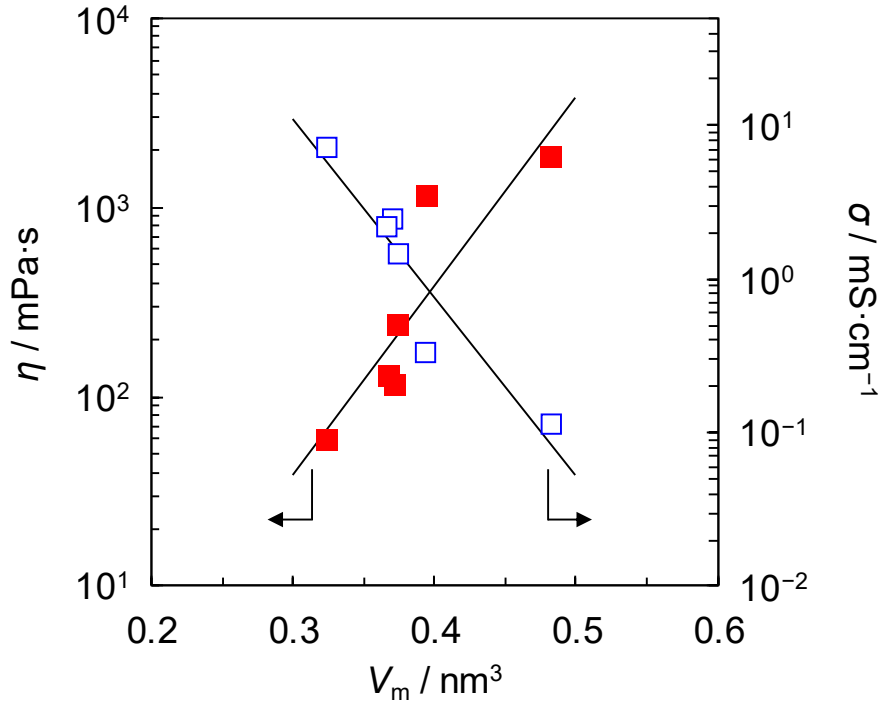

Figure 2-5. Correlation between the (■) ionic pair volume and viscosity at 298 K and the (□) ionic pair volume and ionic conductivity at 303 K. The original data are given in Table 2-1.

The $[PhBF_3]^-$-based RTILs showed viscosities (η) ranging from 60 to 1870 mPa·s at 298 K and ionic conductivities (σ) ranging from 0.112 to 7.09 mS·cm^{-1} at 303 K (Table 2-1). The RTILs with aromatic cations, i.e., $[C_4mim]^+$, $[C_2mim]^+$, and $[C_4py]^+$, had favorable transport properties. Most RTILs with a π-conjugated cation show a similar tendency.[91, 92] The compact volume of aromatic cations, not the liquid structure of RTILs, contributes to the transport properties, as shown in Figure 2-5, and this indicates that the molecular volume is related to the viscosity and conductivity. The following equations proposed by Krossing et al. were used to fit the data.[90]

$$\eta = a_1 e^{b_1 V_m} \tag{2-2}$$

$$\sigma = a_2 e^{-b_2 V_m} \tag{2-3}$$

where a_1 (mPa·s) and a_2 (mS·cm^{-1}) are the empirical pre-exponential factors, b_1 (nm^{-3}) and b_2 (nm^{-3}) are the empirical constants, and V_m (nm^3) is the molecular volume of each organic cation and the $[PhBF_3]^-$ anion in the RTILs. Their volumes were estimated using quantum chemical calculations, and the data are summarized in Table 2-1. The fitting parameters for eq. 2-2 and 2-3 are $a_1 = 4.00 \times 10^{-2}$, $b_1 = 22.9$, $a_2 = 3.48 \times 10^4$, and $b_2 = 26.8$. Interestingly, even though $[C_4mpip][PhBF_3]$ has some deviations, the plots for all the RTILs agree well with the equations, suggesting that the cation volume is an important factor in the $[PhBF_3]^-$-based RTIL system. The obtained slopes, b_1 and b_2, were larger than those for the other anions, e.g., $[BF_4]^-$, $[N(CN)_2]^-$, and $[N(SO_2CF_3)_2]^-$.[90] The values for b_1 are related to the strength of the intermolecular interactions in the RTILs, and the same applies to b_2. In the $[PhBF_3]^-$-based

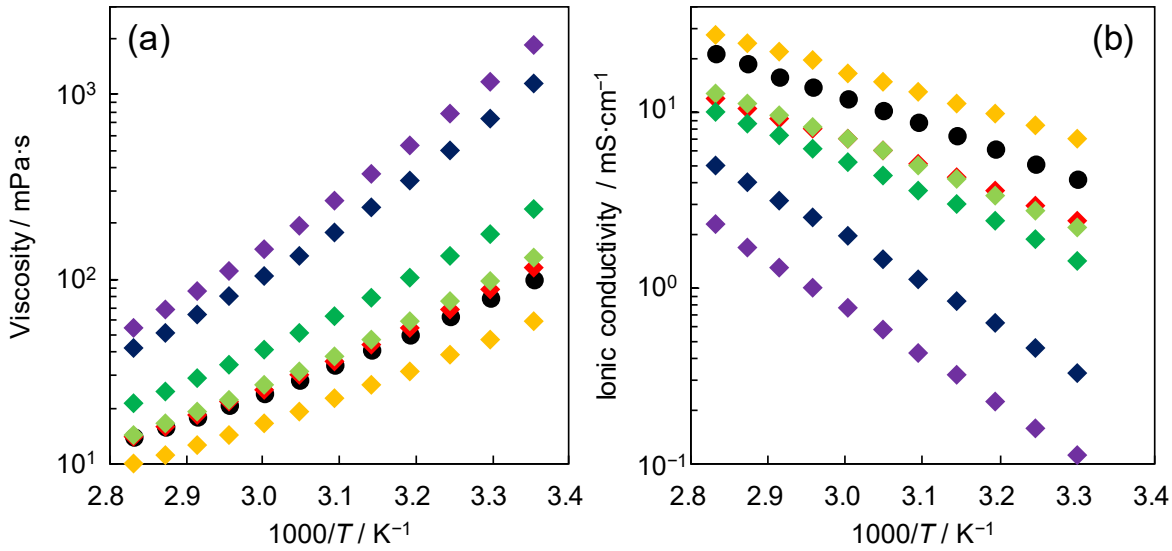

Figure 2-6. Arrhenius plots of the (a) viscosities and (b) ionic conductivities for (●) $[C_4mim][BF_4]$, (◆) $[C_4mim][PhBF_3]$, (◆) $[C_2mim][PhBF_3]$, (◆) $[C_4py][PhBF_3]$, (◆) $[C_4mpyr][PhBF_3]$, (◆) $[C_4mpip][PhBF_3]$, and (◆) $[N_{4,4,4,1}][PhBF_3]$.

RTILs, a stronger interaction was observed compared to the RTILs with other anions, which was contrary to my expectation that the interionic interaction energy would decrease due to the electron-withdrawing phenyl group on the anion. The unexpected behavior could be due to the extra interaction induced by the dynamic contact resistance between the organic cation and the bulky phenyl group on $[PhBF_3]^-$.

Arrhenius plots of the viscosity and ionic conductivity for the RTILs with $[PhBF_3]^-$ are shown in Figure 2-6a and b, respectively. Each plot shows gentle curves, and the curves are common for glass-forming RTILs. In general, the activation energies of the transport properties, viscosity and ionic conductivity can be discussed using Arrhenius plots. However, using the plots to discuss the temperature dependence of glass-forming liquids is difficult because of the complex system generated by the super-Arrhenius behavior.[93] In this case, the Vogel–Tammann–Fulcher (VTF) equation, as expressed below, can be used to fit the transport properties. Eq. 2-4 and 2-5 show the VTF equation for the viscosity and the equivalent ionic conductivity (Λ / S·cm^2·mol^{-1}), respectively.[94, 95]

$$\ln \eta = \frac{k_\eta}{T - T_0} + \frac{1}{2}\ln T - \ln A_\eta \tag{2-4}$$

$$-\ln \Lambda = \frac{k_\Lambda}{T - T_0} + \frac{1}{2}\ln T - \ln A_\Lambda \tag{2-5}$$

where k_η (K) is a constant related to the Arrhenius activation energy for the viscous behavior, k_Λ (K) is a constant related to the conduction behavior, T_0 (K) is an ideal glass-transition temperature, A_η is a scaling factor for the viscosity, and A_Λ is a scaling factor for the equivalent ionic conductivity. The experimental results for the specific ionic conductivity can be converted to the equivalent conductivity using the following equation.

$$\Lambda = \sigma M / d \tag{2-6}$$

where M is the formula weight (g·mol^{-1}) and d is the density (g·cm^{-3}). The fitted parameters obtained from eq. 2-4 and 2-5 are summarized in Table 2-3. The temperature-dependent activation energies for the viscosity ($E_{a,\eta}$) and the equivalent conductivity ($E_{a,\Lambda}$) are given by the following equations, which involve the partial differentiation of eq. 2-4 and 2-5, respectively, with respect to temperature.[94, 95]

$$E_{a,\eta} = -RT^2\left(\frac{\partial \ln \eta}{\partial T}\right) = \frac{Rk_\eta T^2}{(T - T_0)^2} - \frac{RT}{2} \tag{2-7}$$

$$E_{a,\Lambda} = RT^2\left(\frac{\partial \ln \Lambda}{\partial T}\right) = \frac{Rk_\Lambda T^2}{(T - T_0)^2} - \frac{RT}{2} \tag{2-8}$$

The resulting plots of $E_{a,\eta}$ and $E_{a,\Lambda}$ versus the absolute temperature are shown in Figure 2-7. The ionic transport activation energies of the RTILs strongly depended on the cation volume and temperature. The RTILs with larger cations had higher activation energies, and this suggests that the cation structure has a large effect on the activation energy, which directly influences the transport properties. The activation energies decreased as the temperature increased, and almost all the $E_{a,\eta}$ values were higher than the $E_{a,\Lambda}$ values at each temperature.[15, 16, 96] Given that the differential capacitance measured via an AC impedance technique is different from the capacitance estimated using the static method because of the ultra-slow response to the electric double layer formation,[97] the observed differences between the $E_{a,\eta}$ and $E_{a,\Lambda}$ values may be due to the AC impedance method used to perform the ionic conductivity measurement.

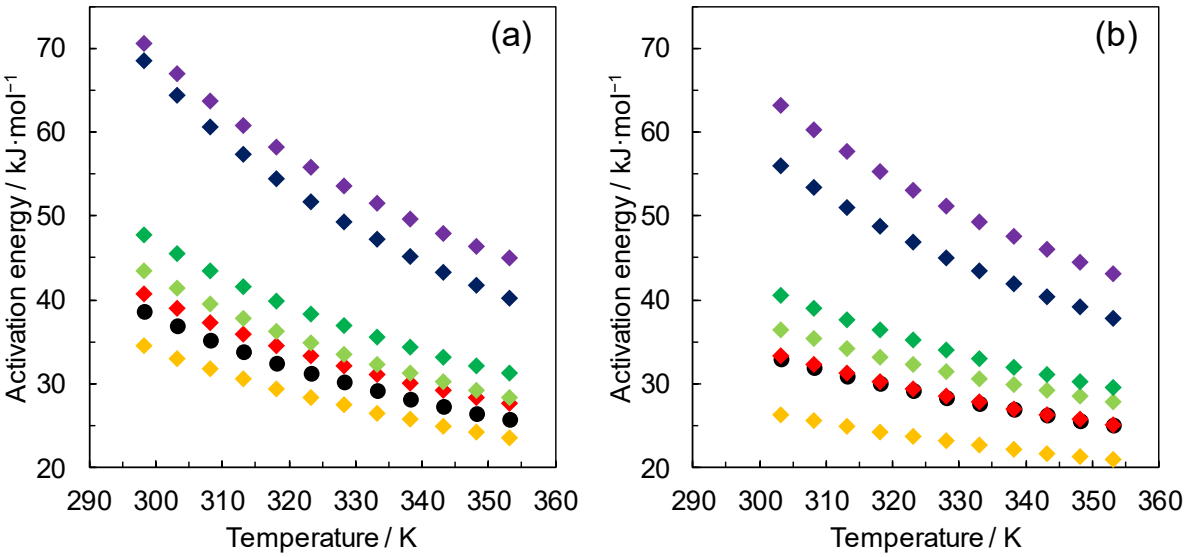

Figure 2-7. Temperature-dependent activation energies for the (a) viscosity and (b) equivalent conductivity for (●) [C4mim][BF4], (◆) [C4mim][PhBF3], (◆) [C2mim][PhBF3], (◆) [C4py][PhBF3], (◆) [C4mpyr][PhBF3], (◆) [C4mpip][PhBF3], and (◆) [N4,4,4,1][PhBF3].

Table 2-3. Fitted parameters for the VTF equations for the viscosity and equivalent conductivity of the $[PhBF_3]^-$-based RTILs

RTILs	Parameters derived from the viscosity				Parameters derived from the equivalent conductivity			
	T_0 / K	k_η / K	ln A_η	$\|R\|$	T_0 / K	k_Λ / K	ln A_Λ	$\|R\|$
$[C_4mim][BF_4]$	171	8.71×10^2	5.08	0.9999	148	2.70×10^3	13.2	0.9999
$[C_4mim][PhBF_3]$	168	9.61×10^2	5.48	0.9999	152	1.04×10^3	9.21	0.9999
$[C_2mim][PhBF_3]$	166	8.45×10^2	5.15	0.9999	132	1.41×10^3	10.6	0.9999
$[C_4py][PhBF_3]$	176	9.03×10^2	5.37	0.9999	148	1.19×10^3	9.90	0.9999
$[C_4mpyr][PhBF_3]$	176	9.89×10^2	5.46	0.9999	162	1.09×10^3	9.62	0.9999
$[C_4mpip][PhBF_3]$	195	1.00×10^3	5.53	0.9999	180	2.78×10^3	14.5	0.9999
$[N_{4,4,4,1}][PhBF_3]$	182	1.31×10^3	6.59	0.9999	178	4.14×10^3	17.2	0.9999

The Walden plot method and pulsed-field-gradient spin-echo (PGSE) NMR[98] spectroscopy are often used to estimate the dissociation degree of RTILs, i.e., the ionicity. Here, to investigate the ionicity of the $[PhBF_3]^-$-based RTILs at each temperature, the author evaluated the degree of the ionic dissociation using the Walden plot method that requires data on the equivalent ionic conductivity and the reciprocal of the viscosity.[15, 16, 99] In Figure 2-8, the Walden plots of the $[PhBF_3]^-$-based RTILs are shown, and the plots of $[C_4mim][BF_4]$ are included for comparison. The diagonal line in the figure is an ideal line for an 1 M KCl aqueous solution that is regarded as an ideal dissociation state. If there are partially associated ion pairs in RTILs, the plots deviate from the ideal line, and the degree of ionic dissociation can be visually estimated based on the deviation. Interestingly, the plots of most of the $[PhBF_3]^-$-based RTILs and $[C_4mim][BF_4]$ were close to the ideal line. The small gaps between the ideal line and the plots imply that the RTILs have favorable dissociation degrees. In terms of the ionicity, the introduction of the phenyl group to BF_3 did not have a large influence.

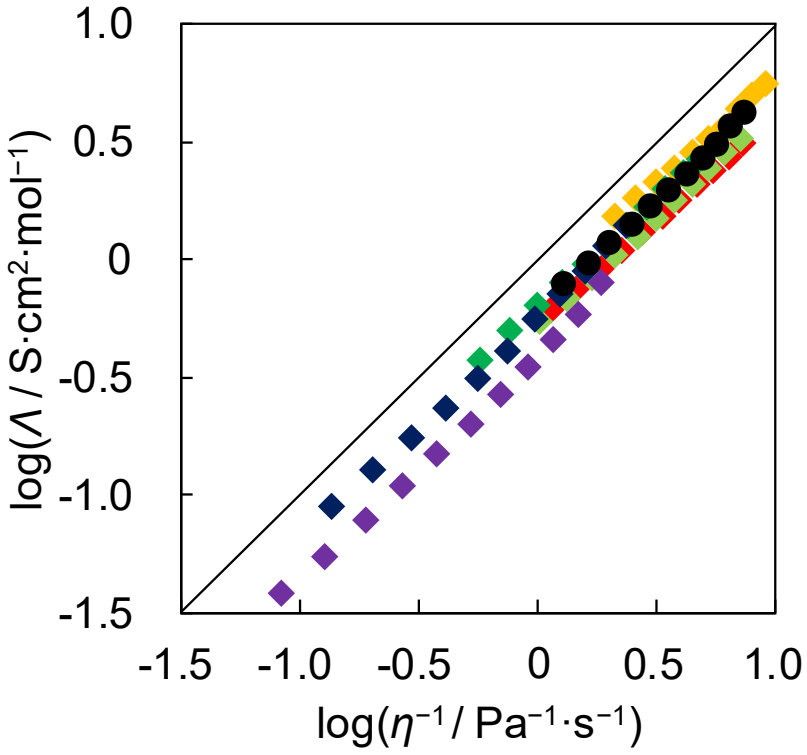

Figure 2-8. Walden plots for (●) $[C_4mim][BF_4]$, (◆) $[C_4mim][PhBF_3]$, (◆) $[C_2mim][PhBF_3]$, (◆) $[C_4py][PhBF_3]$, (◆) $[C_4mpyr][PhBF_3]$, (◆) $[C_4mpip][PhBF_3]$, and (◆) $[N_{4,4,4,1}][PhBF_3]$. The solid line in the figure is an ideal line constructed from the data for an 1 M KCl aqueous solution.

2.3.4. Electrochemical analysis

The electrochemical stability, which is generally called the EW,[100] of the RTILs with $[PhBF_3]^-$ was examined via linear sweep voltammetry. The obtained voltammograms are shown in Figure 2-9. Each scan was initiated from the open circuit potential, and all the cathodic limiting potentials (E_c), the anodic limiting potentials (E_a), and the EWs ($EW = E_a - E_c$) were estimated from Figure 2-9. The electrochemical data are summarized in Table 2-4. The ascending order of the RTIL EWs is $[C_4py][PhBF_3]$ (2.42 V) < $[C_2mim][PhBF_3]$ (3.71 V) < $[C_4mim][PhBF_3]$ (3.78 V) < $[N_{4,4,4,1}][PhBF_3]$ (4.40 V) < $[C_4mpip][PhBF_3]$ (4.55 V) < $[C_4mpyr][PhBF_3]$ (4.67 V). The RTILs with a quaternary ammonium cation, which is known to be more electrochemically stable than aromatic cations, showed wider EWs. Typically, the cathodic and anodic limiting reactions in RTILs are the decompositions of the cation and anion, respectively.[75, 79, 81] The anodic limiting potentials of the RTILs with $[PhBF_3]^-$ had relatively similar values of 0.584–0.804 V (vs. Ag(I)/Ag), but the potentials were substantially lower than those with $[BF_4]^-$ (ca. 1.65 V). This was probably due to the oxidizable electron-rich phenyl group in $[PhBF_3]^-$. In contrast, the cathodic stabilities differed based on the cation structure. The quaternary ammonium cations, $[C_4mpyr]^+$, $[C_4mpip]^+$, and $[N_{4,4,4,1}]^+$, had a higher stability than that of the other aromatic cations. $[C_4py]^+$ had the lowest cathodic stability, and the stability difference from $[C_2mim]^+$ was ca. 1.1 V. This is an acceptable potential gap considering the reported values observed in $[C_2mim][AlCl_4]$ and $[C_4py][AlCl_4]$.[101]

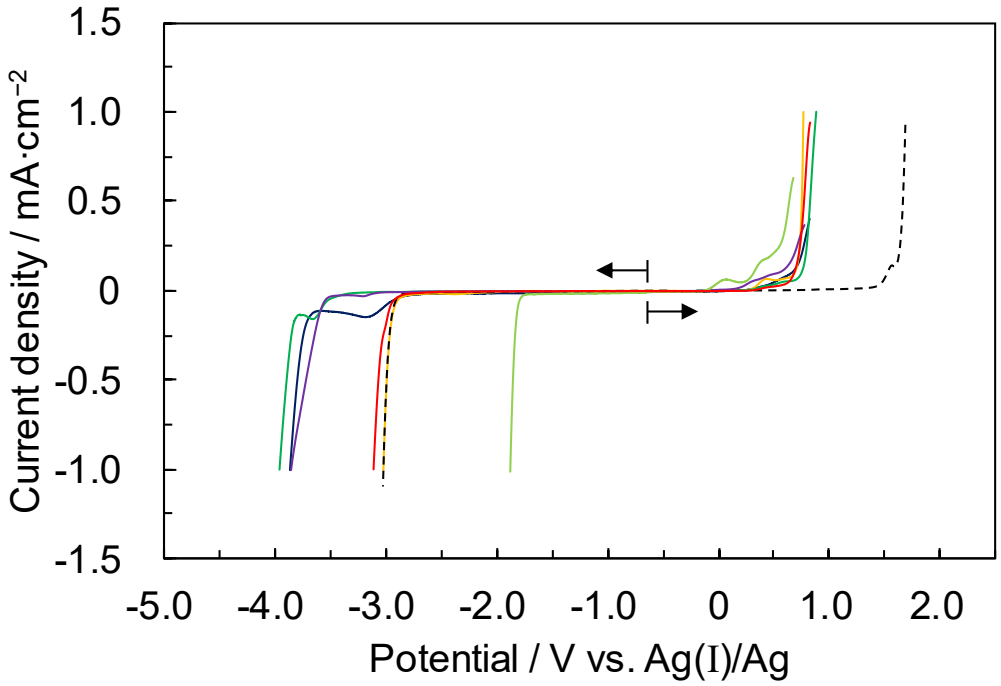

Figure 2-9. Linear sweep voltammograms taken by a glassy carbon electrode in (---) $[C_4mim][BF_4]$, (—) $[C_4mim][PhBF_3]$, (—) $[C_2mim][PhBF_3]$, (—) $[C_4py][PhBF_3]$, (—) $[C_4mpyr][PhBF_3]$, (—) $[C_4mpip][PhBF_3]$, and (—) $[N_{4,4,4,1}][PhBF_3]$ at 298 K. The scan rate was 10 mV·s^{-1}.

Table 2-4. Cathodic and anodic limits and electrochemical windows for the $[PhBF_3]^-$-based RTILs

RTILs	E_c[a] / V vs. Ag(I)/Ag	E_a[b] / V vs. Ag(I)/Ag	EW[c] / V
$[C_4mim][BF_4]$	−2.99	1.65	4.64
$[C_4mim][PhBF_3]$	−3.04	0.745	3.78
$[C_2mim][PhBF_3]$	−2.97	0.739	3.71
$[C_4py][PhBF_3]$	−1.84	0.584	2.42
$[C_4mpyr][PhBF_3]$	−3.86	0.804	4.67
$[C_4mpip][PhBF_3]$	−3.76	0.787	4.55
$[N_{4,4,4,1}][PhBF_3]$	−3.66	0.735	4.40

[a] Cathodic limiting potential at the cut-off current density of −0.3 $mA \cdot cm^{-2}$. [b] Anodic limiting potential at the cut-off current density of 0.3 $mA \cdot cm^{-2}$. [c] Electrochemical window; $EW = E_a - E_c$.

2.4. Summary

The author successfully synthesized six novel RTILs and one organic salt with $[PhBF_3]^-$. Their thermal stabilities are moderate and do not exceed that of the $[BF_4]^-$-based RTILs due to the decomposition of $[PhBF_3]^-$, which has a thermally unstable B–C bond. However, the other physicochemical properties of the $[PhBF_3]^-$-based RTILs were basically favorable even though $[PhBF_3]^-$ is a relatively rigid and large anion compared to the typical anion components in RTILs. Introducing the phenyl group to the BF_3 structure was not problematic. In RTIL systems, the cationic species as well as the anionic ones has a major effect on the physicochemical properties. Several design criteria for RTIL systems were successfully obtained. The fundamental findings reported in this article will be useful for creating currently unknown functional RTILs.

2.5. Characterization data

Characterization of the phenyltrifluoroborate-based salts were conducted in the same condition and manner described in Chapter 1.

1-Butyl-3-methylimidazolium phenyltrifluoroborate ([C$_4$mim][PhBF$_3$]):

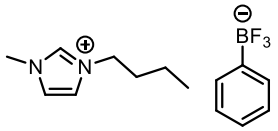

Colorless liquid. ^{1}H NMR (400 MHz, $CDCl_3$): σ 0.884 (t, 3H, $^3J_{HH}$ = 7.3 Hz), 1.17–1.27 (m, 2H), 1.60–1.69 (m, 2H), 3.68 (s, 3H), 3.89 (q, 2H, $^3J_{HH}$ = 5.9 Hz), 7.03 (d, 1H, $^3J_{HH}$ = 2.0 Hz), 7.08 (d, 1H, $^3J_{HH}$ = 1.6 Hz), 7.14 (d, 1H, $^3J_{HH}$ = 7.6 Hz), 7.19 (t, 2H, $^3J_{HH}$ = 7.2 Hz), 7.53 (d, 2H, $^3J_{HH}$ = 5.8 Hz), 8.62 (s, 1H). ^{13}C NMR (100 MHz, $CDCl_3$): σ 13.3 (s), 19.3 (s), 31.8 (s), 36.0 (s), 49.5 (s), 121.8 (s), 123.4 (s), 126.6 (s), 127.0 (s), 131.4 (s), 136.3 (s). ^{19}F NMR (376 MHz, $CDCl_3$): σ −141.7 (s, 3F, B*F*$_3$). ^{11}B NMR (128 MHz, $CDCl_3$): σ 3.72 (d, $^1J_{BF}$ = 43.0 Hz, *B*F$_3$). HRMS (FAB), *m*/*z*: calcd. for $C_{22}H_{35}N_4BF_3^+$ 423.2901 [M + [C$_4$mim]]$^+$; found 423.2897. Elemental analysis calcd. for $C_{14}H_{20}N_2BF_3$: C, 59.18; H, 7.10; N, 9.86; found: C, 57.70; H, 7.42; N, 9.56.

1-Ethyl-3-methylimidazolium phenyltrifluoroborate ([C$_2$mim][PhBF$_3$]):

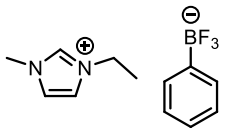

Colorless liquid. ^{1}H NMR (400 MHz, $CDCl_3$): σ 1.39 (t, 3H, $^3J_{HH}$ = 7.3 Hz), 3.72 (s, 3H), 4.00 (q, 2H, $^3J_{HH}$ = 7.6 Hz), 7.06–7.07 (m, 2H), 7.15 (d, 1H, $^3J_{HH}$ = 6.9 Hz), 7.21 (t, 2H, $^3J_{HH}$ = 7.1 Hz), 7.54 (d, 2H, $^3J_{HH}$ = 6.9 Hz), 8.72 (s, 1H). ^{13}C NMR (100 MHz, $CDCl_3$): σ 15.2 (s), 36.1 (s), 45.0 (s), 121.4 (s), 123.3 (s), 126.1 (s), 127.1 (s), 131.4 (s), 136.4 (s). ^{19}F NMR (376 MHz, $CDCl_3$): σ −141.8 (s, 3F, B*F*$_3$). ^{11}B NMR (128 MHz, $CDCl_3$): σ 3.75 (d, $^1J_{BF}$ = 45.0 Hz, *B*F$_3$). HRMS (FAB), *m*/*z*: calcd. for $C_{18}H_{27}N_4BF_3^+$ 367.2275 [M + [C$_2$mim]]$^+$; found 367.2276. Elemental analysis calcd. for $C_{12}H_{16}N_2BF_3$: C, 56.28; H, 6.30; N, 10.94; found: C, 54.51; H, 6.80; N, 10.68.

1-Butylpyridinium phenyltrifluoroborate ([C$_4$py][PhBF$_3$]):

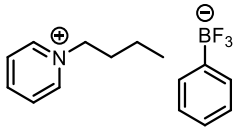

Light brown liquid. ^{1}H NMR (400 MHz, $CDCl_3$): σ 0.882 (t, 3H, $^3J_{HH}$ = 7.2 Hz), 1.24 (m, 2H, $^3J_{HH}$ = 7.6 Hz), 1.77 (m, 2H, $^3J_{HH}$ = 7.7 Hz), 4.39 (t, 2H, $^3J_{HH}$ = 7.6 Hz), 7.11–7.20 (m, 3H), 7.53 (d, 2H, $^3J_{HH}$ = 6.4 Hz), 7.78 (t, 2H, $^3J_{HH}$ = 7.1 Hz), 8.23 (t, 1H, $^3J_{HH}$ = 7.1 Hz), 8.58 (d, 2H, $^3J_{HH}$ = 5.5 Hz). ^{13}C NMR (100 MHz, $CDCl_3$): σ 13.3 (s), 19.1 (s), 33.4 (s), 61.9 (s), 126.2 (s), 127.1 (s), 128.3 (s), 131.6 (s), 144.4 (s), 144.8 (s). ^{19}F NMR (376 MHz, $CDCl_3$): σ −142.2 (s, 3F, B*F*$_3$). ^{11}B NMR (128 MHz, $CDCl_3$): σ 3.73 (s, *B*F$_3$). HRMS (FAB), *m*/*z*: calcd. for

$C_{24}H_{33}N_2BF_3^+$ 417.2683 [M + [C_{4py}]]$^+$; found 417.2681. Elemental analysis calcd. for $C_{15}H_{19}NBF_3$: C, 64.09; H, 6.81; N, 4.98; found: C, 62.69; H, 7.29; N, 4.97.

1-Butyl-1-methylpyrrolidinium phenyltrifluoroborate ([C4mpyr][PhBF3]):

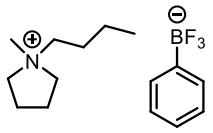

Colorless liquid. ^{1}H NMR (400 MHz, $CDCl_3$): σ 0.888 (t, 3H, $^3J_{HH}$ = 7.3 Hz), 1.24 (m, 2H, $^3J_{HH}$ = 7.4 Hz), 1.45 (m, 2H, $^3J_{HH}$ = 8.0 Hz), 1.95 (m, 4H), 2.68 (s, 3H), 2.97–3.01 (m, 2H), 3.13–3.16 (m, 4H), 7.11 (t, 1H, $^3J_{HH}$ = 7.1 Hz), 7.17 (t, 2H, $^3J_{HH}$ = 7.3 Hz), 7.49 (d, 2H, $^3J_{HH}$ = 6.9 Hz). ^{13}C NMR (100 MHz, $CDCl_3$): σ 13.5 (s), 19.4 (s), 21.2 (s), 25.5 (s), 47.6 (s), 63.8 (s), 126.0 (s), 127.0 (s), 131.4 (s). ^{19}F NMR (376 MHz, $CDCl_3$): σ −142.3 (s, 3F, B*F3*). ^{11}B NMR (128 MHz, $CDCl_3$): σ 3.50 (s, *B*F_3). HRMS (FAB), *m*/*z*: calcd. for $C_{24}H_{45}N_2BF_3^+$ 429.3622 [M + [C_4mpyr]]$^+$; found 429.3632. Elemental analysis calcd. for $C_{15}H_{25}NBF_3$: C, 62.74; H, 8.78; N, 4.88; found: C, 61.11; H, 9.12; N, 4.75.

1-Butyl-1-methylpiperidinium phenyltrifluoroborate ([C4mpip][PhBF3]):

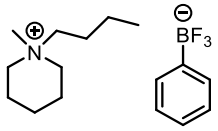

Colorless liquid. ^{1}H NMR (400 MHz, $CDCl_3$): σ 0.899 (t, 3H, $^3J_{HH}$ = 7.1 Hz), 1.25 (m, 2H, $^3J_{HH}$ = 7.3 Hz), 1.39–1.55 (m, 4H), 1.61 (m, 4H), 2.73 (m, 3H), 2.99–3.02 (m, 6H), 7.10 (t, 1H, $^3J_{HH}$ = 6.9 Hz), 7.17 (t, 2H, $^3J_{HH}$ = 7.6 Hz), 7.51 (d, 2H, $^3J_{HH}$ = 7.3 Hz). ^{13}C NMR (100 MHz, $CDCl_3$): σ 13.5 (s), 19.4 (s), 19.7 (s), 20.4 (s), 23.4 (s), 47.1 (s), 60.5 (s), 63.3 (s), 126.0 (s), 126.9 (s), 131.5 (s). ^{19}F NMR (376 MHz, $CDCl_3$): σ −141.6 (s, 3F, B*F3*). ^{11}B NMR (128 MHz, $CDCl_3$): σ 3.54 (s, *B*F3). HRMS (FAB), *m*/*z*: calcd. for $C_{26}H_{49}N_2BF_3^+$ 457.3935 [M + [C_4mpip]]$^+$; found 457.3949. Elemental analysis calcd. for $C_{16}H_{27}NBF_3$: C, 63.80; H, 9.04; N, 4.65; found: C, 62.05; H, 9.29; N, 4.59.

Trimethylpropylammonium phenyltrifluoroborate ([N1,1,1,3][PhBF3]):

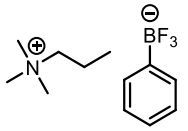

Colorless solid. ^{1}H NMR (400 MHz, $CDCl_3$): σ 0.904 (t, 3H, $^3J_{HH}$ = 7.4 Hz), 1.54–1.63 (m, 2H), 3.00 (s, 9H), 3.06–3.10 (m, 2H), 7.15 (t, 1H, $^3J_{HH}$ = 7.4 Hz), 7.22 (t, 2H, $^3J_{HH}$ = 7.2 Hz), 7.54 (d, 2H, $^3J_{HH}$ = 6.4 Hz). ^{13}C NMR (100 MHz, $CDCl_3$): σ 10.4 (s), 16.4 (s), 53.0 (s), 68.1 (s),

126.2 (s), 127.1 (s), 131.4 (s). ^{19}F NMR (376 MHz, $CDCl_3$): σ −140.3 (s, 3F, B*F*$_3$). ^{11}B NMR (128 MHz, $CDCl_3$): σ 3.73 (s, *B*F_3). HRMS (FAB), *m*/*z*: calcd. for $C_{18}H_{37}N_2BF_3^+$ 349.2996 [M + $[N_{1,1,1,3}]]^+$; found 349.3003. Elemental analysis calcd. for $C_{12}H_{21}NBF_3$: C, 58.33; H, 8.57; N, 5.67; found: C, 58.20; H, 8.79; N, 5.86.

Tributylmethylammonium phenyltrifluoroborate ($[N_{4,4,4,1}][PhBF_3]$):

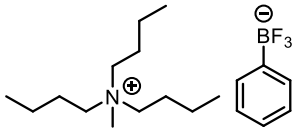

Colorless liquid. ^{1}H NMR (400 MHz, $CDCl_3$): σ 0.895–0.931 (m, 9H), 1.28 (m, 6H), 1.43 (m, 6H), 2.73–2.77 (m, 3H), 2.95–2.99 (m, 6H), 7.08–7.11 (m, 1H), 7.16 (t, 2H, $^3J_{HH}$ = 7.1 Hz), 7.53 (d, 2H, $^3J_{HH}$ = 6.4 Hz). ^{13}C NMR (100 MHz, $CDCl_3$): σ 13.5 (s), 19.4 (s), 23.9 (s), 48.0 (s), 61.1 (s), 125.8 (s), 126.8 (s), 131.6 (s). ^{19}F NMR (376 MHz, $CDCl_3$): σ −142.0 (s, 3F, B*F*$_3$). ^{11}B NMR (128 MHz, $CDCl_3$): σ 3.59 (s, *B*F_3). HRMS (FAB), *m*/*z*: calcd. for $C_{32}H_{65}N_2BF_3^+$ 545.5187 [M + $[N_{4,4,4,1}]]^+$; found 545.5200. Elemental analysis calcd. for $C_{19}H_{35}NBF_3$: C, 66.09; H, 10.22; N, 4.06; found: C, 65.13; H, 10.38; N, 4.03.

Chapter 3 Preparation and Electrochemical Application of Aryltrifluoroborate-Based Room Temperature Ionic Liquids

3.1. Introduction

As mentioned in previous chapters, it is difficult to modify the anion's framework for RTILs although the organic cations are created with ease. Thus, the systematic investigation on RTILs with the diversely functionalized anions is hardly reported until now.[69, 98] If the scheme for introducing any substituent into the anion structure can be established, as is true for organic cations, further advancement of RTIL science and technology will be expected. The author described in Chapter 1 that the preparation of various types of ($[ArBF_3]^-$) anions can be obtained by the easy-to-use scheme. In this chapter, a new family of 1-butyl-3-methylimidazolium ($[C_4mim]^+$)-based RTILs with $[ArBF_3]^-$, whose substituents are methoxy, fluoro, trifluoromethyl, or cyano groups, are synthesized and their physicochemical and electrochemical properties are examined. Several position isomers of disubstituted $[ArBF_3]^-$ anions are also prepared to gain deeper insight into the substituent effects on the physicochemical properties and electrochemical behavior. Additionally, the effects of the anion structure are thoroughly investigated using a computational approach to understand the origin of the substituent effects on the physicochemical behavior of the $[C_4mim][ArBF_3]$ RTILs.

3.2. Experimental

3.2.1. Preparation of aryltrifluoroborate-based RTILs

The synthesis of $[C_4mim][ArBF_3]$ RTILs was carried out by the metathesis protocol expressed below. 1-Butyl-3-methylimidazolium chloride ($[C_4mim]Cl$) (Kanto Chemical Co., Inc.) and the appropriate $K[ArBF_3]$, prepared by the same protocol mentioned in previous chapter, were used as cationic sources and anionic sources, respectively. $K[ArBF_3]$ (40 mmol) was added to the solution of $[C_4mim]Cl$ (40 mmol) in acetonitrile (60 mL), and the mixture was stirred for 1 h at ambient temperature. After the reaction, the mixture was filtered to remove the precipitated KCl, and the filtrate was condensed under vacuum. The crude product extracted by CH_2Cl_2 was rinsed by ultrapure water several times to remove the unreacted precursor and KCl.

The organic layer was concentrated in vacuo. The resultant organic salt was dried at 353 K under vacuum for 12 h. The final product was confirmed by NMR, mass spectrometry, and elemental analysis. 1-Butyl-3-methylimidazolium tetrafluoroborate ([C_4mim][BF_4], Kanto Chemical Co.) was thoroughly vacuum dried for 24 h before use in order to remove residual water.

3.2.2. Thermal and physicochemical property measurements

Thermal an physicochemical properties for [C_4mim][$ArBF_3$] RTILs were measured in the same way described in previous chapter. Thermogravimetric (TG) analysis was performed using a Bruker TG-DTA2000SA and differential scanning calorimetry (DSC) was conducted using a Bruker DSC3100SA. These two instruments were controlled with a Bruker MTC1000SA workstation utilizing the Bruker WS003 software. Density measurements were conducted by a Kyoto Electronics Manufacturing DA-640 resonant frequency oscillation density/specific gravity meter in a range of 298–353 K. Viscosity was measured by a Kyoto Electronics Manufacturing EMS-1000 electromagnetically spinning viscometer in a range of 298–353 K. Ionic conductivity measurements were performed by a Horiba DS-51 digital conductivity meter in a range of 303–353 K using a glass conductivity cell after cell calibration with a 0.1 M KCl aqueous solution. All the measurements except viscosity were carried out in the argon-filled-glove box. Viscosity measurements were carried out using special airtight cells for the electromagnetically spinning viscometer.

3.2.3. Electrochemical measurements

Electrochemical measurements were conducted with an IVIUM Technologies CompactStat portable electrochemical analyzer. All electrochemical experiments were performed in a three-electrode cell. The working electrode was a glassy carbon disk (diameter of 1.6 mm), platinum disk (diameter of 1.6 mm) or platinum plate (10 mm × 10 mm), which was polished with an alumina suspension (diameter of 0.06 μm) before use. Platinum wire (diameter of 0.5 mm) was used as the counter electrode. The reference electrode was constructed by placing an Ag wire (diameter of 1.0 mm) into a glass tube (diameter of 6.0 mm) terminated with Vycor® glass and filling the tube with a 0.05 M Ag[$N(SO_2CF_3)_2$] /[C_4mim][$N(SO_2CF_3)_2$] solution. In the passivation tests, three different types of redox reagents, 1-ethyl-3-methylimidazolium tetrachloroferrate ([C_2mim][$FeCl_4$]), ferrocene ($FeCp_2$), and ferrocenium tetrafluoroborate ([$FeCp_2$][BF_4]), were used to characterize the ion selectivity of the passivation film, and 0.1 M [C_4mim][*p*-$FC_6H_4BF_3$] ionic liquid solutions with the three redox reagents were used as an electrolyte. The passivation films on the Pt electrode surface were prepared by potential sweep in the potential range of −0.5 to 5.0 V vs. Ag(I)/Ag at the scan rate of 10 $mV \cdot s^{-1}$ and were observed by a JEOL JSM-6335F or a Hitachi S-3400N scanning electron microscope (SEM). The composition was determined by an EDAX Octane Prime energy-dispersive X-ray spectroscope (EDX) mounted on the Hitachi S-3400N SEM system. The electrochemical

measurements were carried out in the abovementioned argon-filled-glove box.

3.2.4. Computational methods

The Gaussian 09 program[36] was utilized for the *ab initio* molecular orbital calculations and DFT calculations. The basis sets implemented in the Gaussian program were used. Electron correlation was accounted for by the second-order Møller–Plesset perturbation (MP2) method.[37, 38] The geometries of each ion and ion pair were fully optimized at the HF/6-311G(d,p) level. The ionic volume of the ions was calculated at the B3LYP/6-31G+(d) level.[16] The author determined the final ionic volume from the average of the ionic volumes obtained from ten calculations. The partial atomic charges were obtained from electrostatic potential fitting using the MP2/6-311G(d,p) level calculation. The intermolecular interaction energies (E_{int}) were calculated in the same manner described in Chapter 1. The HOMO energy level of the anion was calculated at the HF/6-311G(d,p) level.

3.3. Results and discussion

3.3.1. General characteristics

Ten types of $[C_4mim]^+$-based RTILs with $[ArBF_3]^-$, each having different substituents on the phenyl ring of the anion, e.g., methoxy (-OMe), fluoro (-F), trifluoromethyl (-CF_3), and cyano (-CN), were successfully prepared in this study. The chemical structures of the synthesized RTILs are depicted in Figure 3-1 with their chemical name and abbreviations. All the RTILs were yielded nearly quantitatively by metathesis reactions. These salts can be handled in open-air conditions without any undesirable reactions; however, they exhibit some hygroscopicity. The $[C_4mim][ArBF_3]$ RTILs with all substituents are immiscible with water, while the alkyl- and alkenyltrifluoroborate-based RTILs, which have an aliphatic chain instead of the aromatic ring, exhibit water-miscibility.[78] The fundamental thermal and physicochemical properties of the $[C_4mim][ArBF_3]$ RTILs are summarized in Table 3-1 along with those for 1-butyl-3-methylimidazolium tetrafluoroborate ($[C_4mim][BF_4]$) and 1-butyl-3-methylimidazolium phenyltrifluoroborate ($[C_4mim][PhBF_3]$) for comparison.[102] Details of their properties will be discussed below.

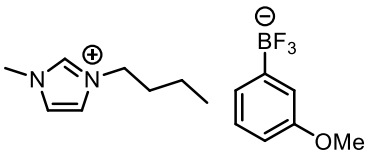

1-butyl-3-methylimidazolium
(*meta*-methoxyphenyl)trifluoroborate
$[C_4mim][m\text{-}OMeC_6H_4BF_3]$

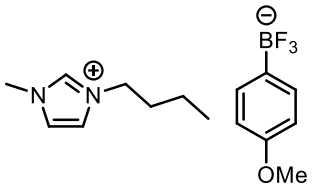

1-butyl-3-methylimidazolium
(*para*-methoxyphenyl)trifluoroborate
$[C_4mim][p\text{-}OMeC_6H_4BF_3]$

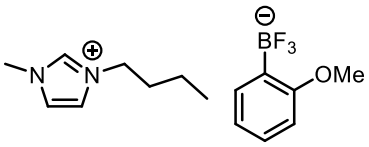

1-butyl-3-methylimidazolium
(*ortho*-methoxyphenyl)trifluoroborate
$[C_4mim][o\text{-}OMeC_6H_4BF_3]$

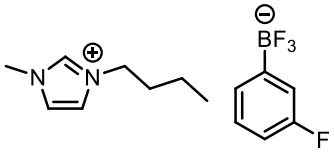

1-butyl-3-methylimidazolium
(*meta*-fluorophenyl)trifluoroborate
$[C_4mim][m\text{-}FC_6H_4BF_3]$

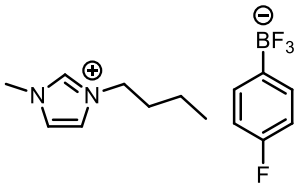

1-butyl-3-methylimidazolium
(*para*-fluorophenyl)trifluoroborate
$[C_4mim][p\text{-}FC_6H_4BF_3]$

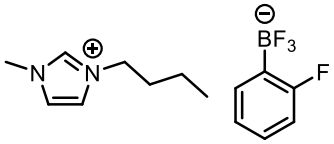

1-butyl-3-methylimidazolium
(*ortho*-fluorophenyl)trifluoroborate
$[C_4mim][o\text{-}FC_6H_4BF_3]$

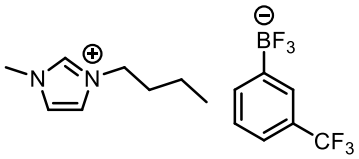

1-butyl-3-methylimidazolium
(*meta*-trifluoromethylphenyl)trifluoroborate
$[C_4mim][m\text{-}CF_3C_6H_4BF_3]$

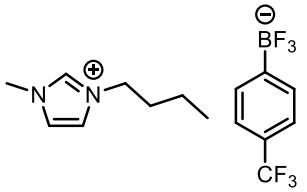

1-butyl-3-methylimidazolium
(*para*-trifluoromethylphenyl)trifluoroborate
$[C_4mim][p\text{-}CF_3C_6H_4BF_3]$

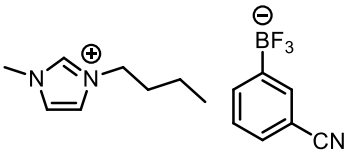

1-butyl-3-methylimidazolium
(*meta*-cyanophenyl)trifluoroborate
$[C_4mim][m\text{-}CNC_6H_4BF_3]$

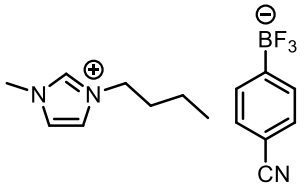

1-butyl-3-methylimidazolium
(*para*-cyanophenyl)trifluoroborate
$[C_4mim][p\text{-}CNC_6H_4BF_3]$

Figure 3-1. Chemical structures of $[C_4mim][ArBF_3]$ RTILs and their abbreviations.

Table 3-1. Fundamental thermal and physicochemical properties of the [C4mim][ArBF3] RTILs

RTILs	FW[a]	T_g[b] / K	T_m[c] / K	T_d[d] / K	d[e] / g·cm^{-3}	η[f] / mPa·s	σ[g] / mS·cm^{-1}	Λ[h] / S·cm^2·mol^{-1}	V_{anion}[i] / nm^3	E_{form}[j] / kcal·mol^{-1}
[C4mim][BF4]	226	190	—	611	1.201	101	4.21	0.795	0.072	−84.8
[C4mim][PhBF3]	284	209	—	492	1.145	115	2.42	0.602	0.164	−85.6
[C4mim][*o*-OMeC6H4BF3]	314	232	—	513	1.182	1870	0.229	0.0611	0.198	−85.9
[C4mim][*m*-OMeC6H4BF3]	314	206	—	528	1.167	261	1.11	0.300	0.192	−83.4
[C4mim][*p*-OMeC6H4BF3]	314	221	—	513	1.170	367	0.767	0.207	0.199	−84.1
[C4mim][*o*-FC6H4BF3]	302	213	—	520	1.200	169	1.82	0.460	0.162	−83.7
[C4mim][*m*-FC6H4BF3]	302	206	—	545	1.188	100	2.60	0.663	0.178	−82.1
[C4mim][*p*-FC6H4BF3]	302	216	—	511	1.192	125	1.99	0.506	0.172	−82.2
[C4mim][*m*-CF3C6H4BF3]	352	208	—	519	1.243	144	1.64	0.466	0.208	−80.4
[C4mim][*p*-CF3C6H4BF3]	352	212	—	521	1.245	167	1.38	0.391	0.201	−79.8
[C4mim][*m*-CNC6H4BF3]	309	217	—	591	1.160	294	1.09	0.292	0.205	−78.9
[C4mim][*p*-CNC6H4BF3]	309	223	—	593	1.162	370	0.861	0.230	0.190	−78.2

[a]Formula weight. [b]Glass-transition temperature. [c]Melting point. [d]Thermal degradation temperature at 5 wt% loss. [e]Density at 298 K. [f]Viscosity at 298 K. [g]Ionic conductivity at 303 K. [h]Equivalent conductivity at 303 K. [i]Volume of anion given by the Gaussian 09 program at the B3LYP/6-31G+(d) level. [j]Formation energy of the ionic pair that is given by the Gaussian 09 program at the MP2/6-311G(d,p) level.

3.3.2. Thermal and physicochemical properties

TG-DTA curves for the [C_4mim][$ArBF_3$] RTILs are shown in Figure 3-2. The author defined the thermal degradation temperature (T_d) as the 5 wt% loss point of the TG curves. As given in Table 3-1, the [C_4mim][$ArBF_3$] RTILs showed a T_d of 511–593 K. These values are slightly higher than that of non-substitutive [C_4mim][$PhBF_3$] (T_d: 492 K). All the TG curves exhibit a two-step weight loss behavior. The mild bond dissociation energies of B–C, C–OMe, C–F, etc., compared to the C–C bonding energies, can possibly result in anion decomposition.[103, 104] The introduction of the cyano group, -CN, to the phenyl moiety, makes the $[ArBF_3]^-$ anion inactive in the thermal degradation reaction. The results of the DSC experiments for the same RTILs are shown in Figure 3-3. Only the glass-transition behavior based on the second-order phase change is clearly observed at 206–232 K in the [C_4mim][$ArBF_3$] RTILs. All have glass-transition temperatures (T_g).

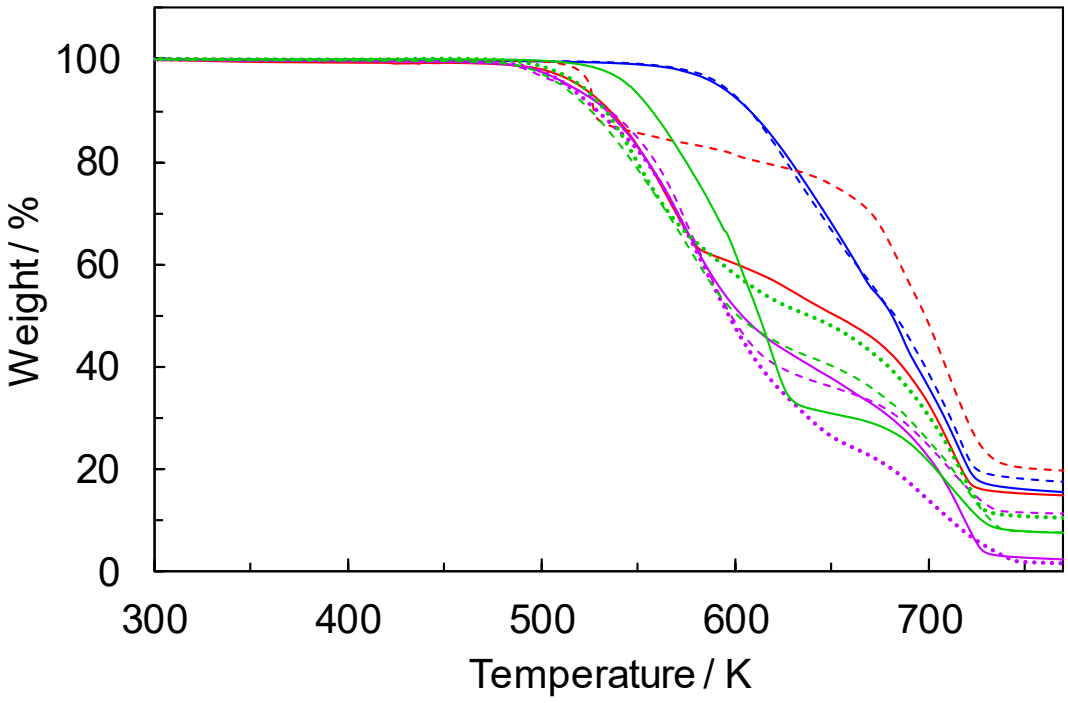

Figure 3-2. Results of the TG analysis for (····) [C_4mim][*o*-$OMeC_6H_4BF_3$], (—) [C_4mim][*m*-$OMeC_6H_4BF_3$], (---) [C_4mim][*p*-$OMeC_6H_4BF_3$], (····) [C_4mim][*o*-$FC_6H_4BF_3$], (—) [C_4mim][*m*-$FC_6H_4BF_3$], (---) [C_4mim][*p*-$FC_6H_4BF_3$], (—) [C_4mim][*m*-$CF_3C_6H_4BF_3$], (---) [C_4mim][*p*-$CF_3C_6H_4BF_3$], (—) [C_4mim][*m*-$CNC_6H_4BF_3$], (---) [C_4mim][*p*-$CNC_6H_4BF_3$]. The measurements were conducted at 5 $K \cdot min^{-1}$.

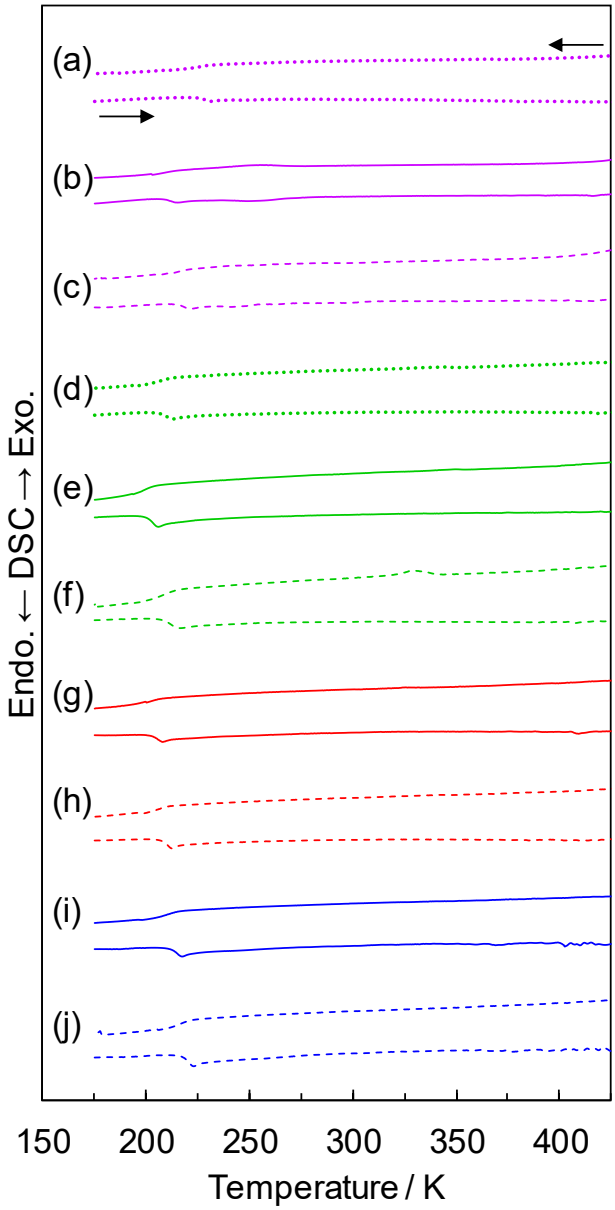

Figure 3-3. DSC curves of (a) [C_4mim][*o*-$OMeC_6H_4BF_3$], (b) [C_4mim][*m*-$OMeC_6H_4BF_3$], (c) [C_4mim][*p*-$OMeC_6H_4BF_3$], (d) [C_4mim][*o*-$FC_6H_4BF_3$], (e) [C_4mim][*m*-$FC_6H_4BF_3$], (f) [C_4mim][*p*-$FC_6H_4BF_3$], (g) [C_4mim][*m*-$CF_3C_6H_4BF_3$], (h) [C_4mim][*p*-$CF_3C_6H_4BF_3$], (i) [C_4mim][*m*-$CNC_6H_4BF_3$], and (j) [C_4mim][*p*-$CNC_6H_4BF_3$]. The measurements were conducted at 5 $K \cdot min^{-1}$.

The temperature dependences of density (d) for the [C_4mim][$ArBF_3$] RTILs are shown in Figure 3-4. The linear correlation was given from the plots of density versus absolute temperature in the figure. Density can be explained as a function of the absolute temperature with the equation $d = a + bT$, where a is the density at 0 K ($g \cdot cm^{-3}$), b is the volume expansion coefficient ($g \cdot cm^{-3} \cdot K^{-1}$), and T is the absolute temperature. The fitting results using the least-square method are displayed in Table 3-2. Each fitting line in the figure exhibited a good correlation coefficient ($|R|$) of > 0.9999. The [C_4mim][$ArBF_3$] RTILs, especially those with the fluoro and trifluoromethyl group, showed higher densities than [C_4mim][$PhBF_3$] because of the dense packing structure, as discussed below.

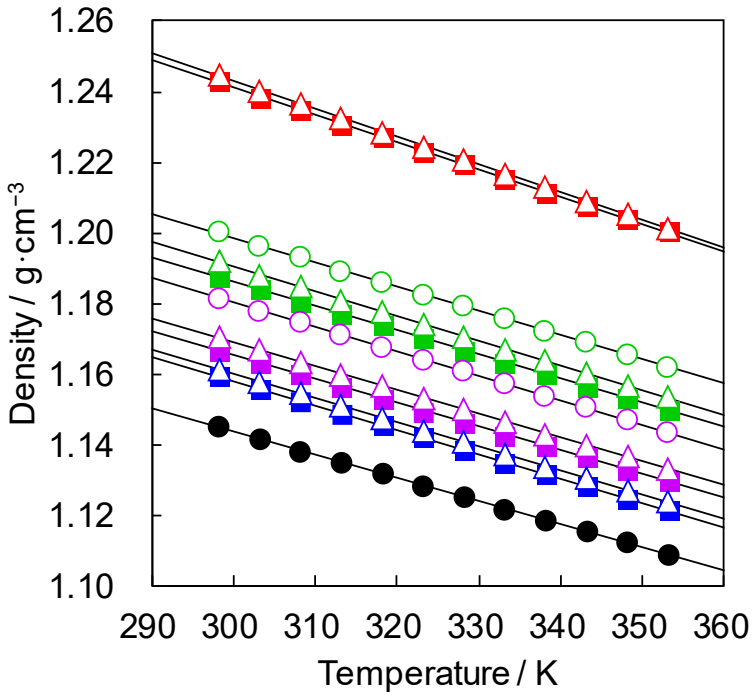

Figure 3-4. Temperature dependences of the density for (○) [C_4mim][o-$OMeC_6H_4BF_3$], (■) [C_4mim][m-$OMeC_6H_4BF_3$], (△) [C_4mim][p-$OMeC_6H_4BF_3$], (○) [C_4mim][o-$FC_6H_4BF_3$], (■) [C_4mim][m-$FC_6H_4BF_3$], (△) [C_4mim][p-$FC_6H_4BF_3$], (■) [C_4mim][m-$CF_3C_6H_4BF_3$], (△) [C_4mim][p-$CF_3C_6H_4BF_3$], (■) [C_4mim][m-$CNC_6H_4BF_3$], (△) [C_4mim][p-$CNC_6H_4BF_3$], and (●) [C_4mim][$PhBF_3$].

Table 3-2. Fitted parameters for the densities of the [C_4mim][$ArBF_3$] RTILs

RTILs	a / g·cm^{-3}	$b \times 10^4$/ g·cm^{-3}·K^{-1}	$\|R\|$
[C_4mim][BF_4]	1.413	−7.113	> 0.9999
[C_4mim][$PhBF_3$]	1.339	−6.510	> 0.9999
[C_4mim][*o*-$OMeC_6H_4BF_3$]	1.387	−6.891	> 0.9999
[C_4mim][*m*-$OMeC_6H_4BF_3$]	1.366	−6.683	> 0.9999
[C_4mim][*p*-$OMeC_6H_4BF_3$]	1.370	−6.714	> 0.9999
[C_4mim][*o*-$FC_6H_4BF_3$]	1.405	−6.875	> 0.9999
[C_4mim][*m*-$FC_6H_4BF_3$]	1.393	−6.880	> 0.9999
[C_4mim][*p*-$FC_6H_4BF_3$]	1.400	−6.985	> 0.9999
[C_4mim][*m*-$CF_3C_6H_4BF_3$]	1.472	−7.710	> 0.9999
[C_4mim][*p*-$CF_3C_6H_4BF_3$]	1.478	−7.844	> 0.9999
[C_4mim][*m*-$CNC_6H_4BF_3$]	1.365	−6.887	> 0.9999
[C_4mim][*p*-$CNC_6H_4BF_3$]	1.366	−6.855	> 0.9999

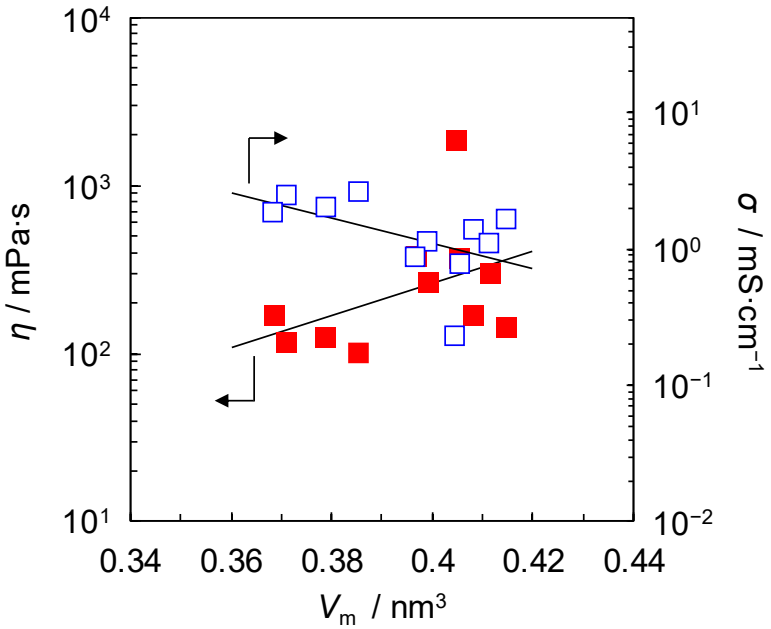

Figure 3-5. Correlation between the (■) ionic pair volume and viscosity at 298 K and the (□) ionic pair volume and ionic conductivity at 303 K. V_m is the sum of V_a and V_c. In this study, V_c, as the volume of [C_4mim]$^+$ is 0.207 nm^3, which is calculated by the Gaussian 09 program at the B3LYP/6-31G+(d) level. The original data are given in Table 3-1.

The basic transport properties, viscosities and ionic conductivities for the [C4mim][ArBF3] RTILs are summarized in Table 3-1. The difference in the group type and the bonding position of the groups greatly impact the properties. Figure 3-5 shows the correlation between the ionic pair volume (V_m) and the transport properties for the [C4mim][ArBF3] RTILs. The author could not obtain a favorable linear relationship between the ion pair volume and transport properties,[89] in contrast to the contents described in Chapter 2 using the same anionic species, $[PhBF_3]^-$, but different cationic species.[102] Therefore, the physicochemical properties of the [C4mim][ArBF3] RTILs are mainly influenced, not by the ionic pair volume, but by the anion structure.[91] In addition, all the RTILs with a group at the meta position exhibit favorable properties relative to the ortho and para counterparts. For example, [C4mim][*m*-FC6H4BF3] shows the highest fluidity and ionic conductivity among the other [C4mim][ArBF3] RTILs.

Arrhenius plots of the viscosity (η) and ionic conductivity (σ) for the [C4mim][ArBF3] RTILs are shown in Figure 3-6a and b, respectively. The plots for the viscosity are convex downward, and those for the ionic conductivity are convex upward. These behaviors are commonly observed in glass-forming RTILs.[93] To discuss the transport properties in detail, the author evaluated the activation energies of the viscosity and equivalent conductivity using the Vogel–Tamman–Fulcher (VTF) equation and its partial differential.[94, 95] The VTF equation can be widely used to fit the transport properties of the glass-forming substances, and the fitted parameters are summarized in Table 3-3. The temperature-dependent activation energies for viscosity ($E_{a,\eta}$) and equivalent conductivity ($E_{a,\Lambda}$) can be obtained from the partial differential

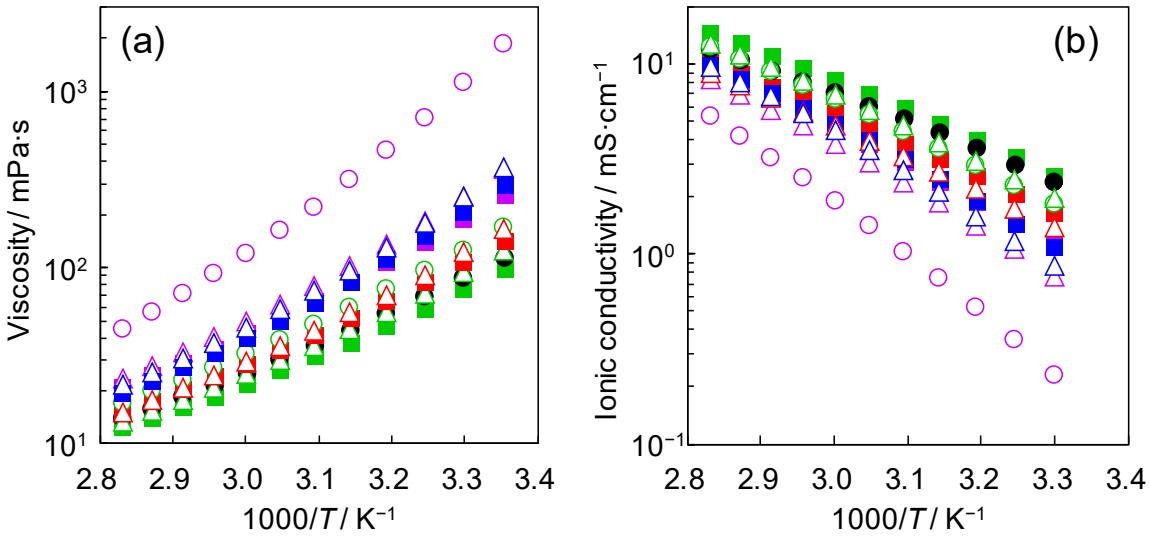

Figure 3-6. Arrhenius plots of (a) viscosities and (b) ionic conductivities for (○) [C4mim][*o*-OMeC6H4BF3], (■) [C4mim][*m*-OMeC6H4BF3], (△) [C4mim][*p*-OMeC6H4BF3], (○) [C4mim][*o*-FC6H4BF3], (■) [C4mim][*m*-FC6H4BF3], (△) [C4mim][*p*-FC6H4BF3], (■) [C4mim][*m*-CF3C6H4BF3], (△) [C4mim][*p*-CF3C6H4BF3], (■) [C4mim][*m*-CNC6H4BF3], (△) [C4mim][*p*-CNC6H4BF3], and (●) [C4mim][PhBF3].

of the VTF equations with respect to temperature.[94, 95] The resulting plots of $E_{a,\eta}$ and $E_{a,\Lambda}$ versus absolute temperature are shown in Figure 3-7, indicating that there is a strong temperature dependence of the activation energies for ionic transport. The activation energies decreased with increasing temperature, and most $E_{a,\eta}$ values were higher than $E_{a,\Lambda}$ at each temperature, as shown in previous reports.[15, 16, 96, 102]

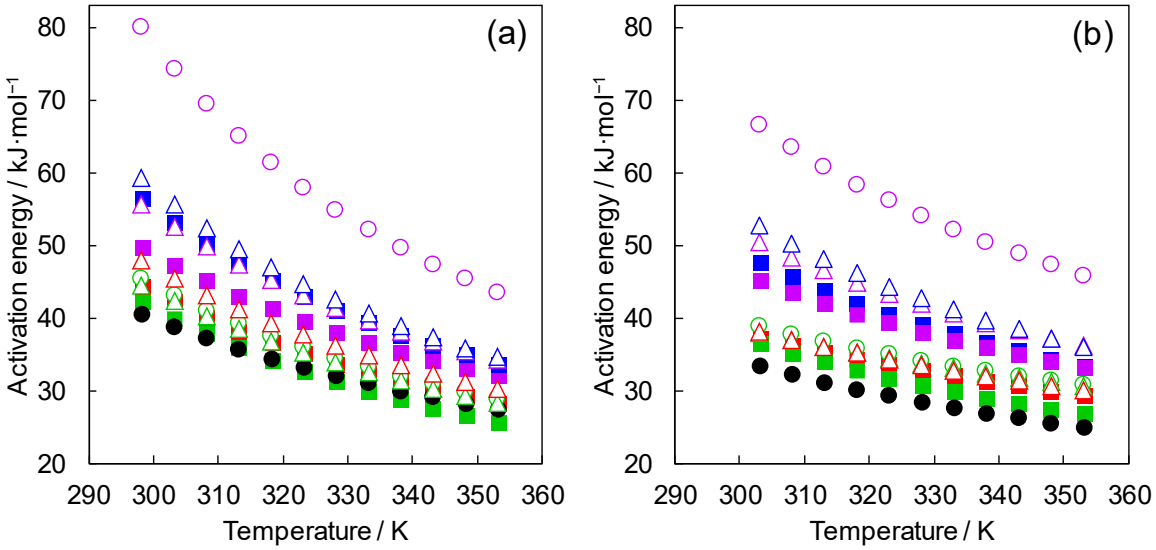

Figure 3-7. Temperature dependences of the activation energies derived from (a) the viscosities and (b) the ionic conductivities for (○) [C4mim][*o*-OMeC6H4BF3], (■) [C4mim][*m*-OMeC6H4BF3], (△) [C4mim][*p*-OMeC6H4BF3], (○) [C4mim][*o*-FC6H4BF3], (■) [C4mim][*m*-FC6H4BF3], (△) [C4mim][*p*-FC6H4BF3], (■) [C4mim][*m*-CF3C6H4BF3], (△) [C4mim][*p*-CF3C6H4BF3], (■) [C4mim][*m*-CNC6H4BF3], (△) [C4mim][*p*-CNC6H4BF3], and (●) [C4mim][PhBF3].

Table 3-3. Fitted parameters for the VTF equations of viscosity and equivalent conductivity for the [C_4mim][$ArBF_3$] RTILs

RTILs	Parameters derived from viscosity				Parameters derived from equivalent conductivity			
	T_0 / K	k_η / K	ln A_η	$\|R\|$	T_0 / K	k_Λ / K	ln A_Λ	$\|R\|$
[C_4mim][BF_4]	171	8.71×10^2	5.08	0.9999	148	2.70×10^3	13.2	0.9999
[C_4mim][$PhBF_3$]	168	9.61×10^2	5.48	0.9999	152	1.04×10^3	9.21	0.9999
[C_4mim][*o*-$OMeC_6H_4BF_3$]	205	9.54×10^2	5.56	0.9999	176	1.44×10^3	11.3	0.9999
[C_4mim][*m*-$OMeC_6H_4BF_3$]	179	9.82×10^2	5.53	0.9999	160	1.25×10^3	10.4	0.9999
[C_4mim][*p*-$OMeC_6H_4BF_3$]	187	9.53×10^2	5.52	0.9999	166	1.27×10^3	10.6	0.9999
[C_4mim][*o*-$FC_6H_4BF_3$]	180	8.83×10^2	5.19	0.9999	136	1.47×10^3	10.9	0.9999
[C_4mim][*m*-$FC_6H_4BF_3$]	187	7.29×10^2	4.80	0.9999	158	1.04×10^3	9.62	0.9999
[C_4mim][*p*-$FC_6H_4BF_3$]	180	8.66×10^2	5.35	0.9999	127	1.59×10^3	11.2	0.9999
[C_4mim][*m*-$CF_3C_6H_4BF_3$]	181	8.50×10^2	5.14	0.9999	137	1.40×10^3	10.5	0.9999
[C_4mim][*p*-$CF_3C_6H_4BF_3$]	182	8.98×10^2	5.46	0.9999	137	1.43×10^3	10.5	0.9999
[C_4mim][*m*-$CNC_6H_4BF_3$]	192	8.81×10^2	5.45	0.9999	171	1.12×10^3	10.1	0.9999
[C_4mim][*p*-$CNC_6H_4BF_3$]	195	8.72×10^2	5.38	0.9999	177	1.13×10^3	10.3	0.9999

The ionicity, defined as the dissociation degree of the RTILs, is often determined by the Walden plot method as well as pulsed-field-gradient spin-echo (PGSE) NMR measurements.[98] Walden plots are constructed from the equivalent conductivity and reciprocal of viscosity. The gap between an ideal line and the obtained Walden plot implies the dissociation degree of RTILs.[15, 16, 99, 102] In Figure 3-8, Walden plots of the [C4mim][ArBF3] RTILs are displayed, including the results of [C4mim][BF4] for comparison. The diagonal line in the figure is an ideal line, which was estimated from an 1 M KCl aqueous solution with an ideal dissociation state. Walden plots of the [C4mim][ArBF3] RTILs are close to the ideal line. The gaps between the ideal line and the plots indicate favorable dissociation degrees comparable to that of a typical RTIL, [C4mim][BF4]. Interestingly, [C4mim][*o*-OMeC6H4BF3] shows similar gaps to those of other ILs; although, it has the lowest ionic conductivity and fluidity among the [C4mim][ArBF3] RTILs.

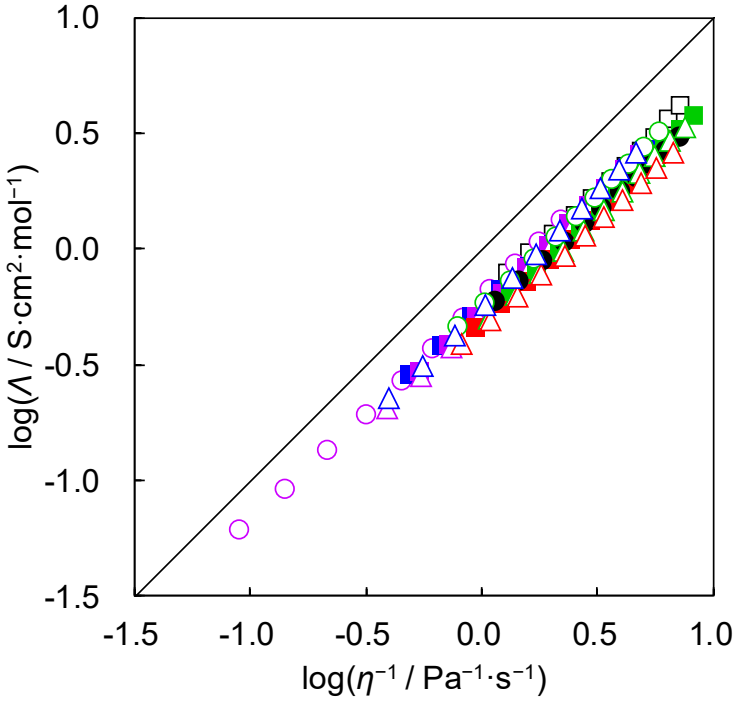

Figure 3-8. Walden plots of (○) [C4mim][*o*-OMeC6H4BF3], (■) [C4mim][*m*-OMeC6H4BF3], (△) [C4mim][*p*-OMeC6H4BF3], (○) [C4mim][*o*-FC6H4BF3], (■) [C4mim][*m*-FC6H4BF3], (△) [C4mim][*p*-FC6H4BF3], (■) [C4mim][*m*-CF3C6H4BF3], (△) [C4mim][*p*-CF3C6H4BF3], (■) [C4mim][*m*-CNC6H4BF3], (△) [C4mim][*p*-CNC6H4BF3], (●) [C4mim][PhBF3], and (□) [C4mim][BF4]. The diagonal line in the figure is an ideal line expected from an 1 M KCl aqueous solution.

3.3.3. Computational analyses

The structures of the $[C_4mim][ArBF_3]$ ion pairs were optimized by *ab initio* calculations for further discussion.[36] The optimized structures of the $[C_4mim][ArBF_3]$ ion pairs are depicted in Figure 3-9 with that of $[C_4mim][BF_4]$ ion pair for comparison. Almost all optimized structures of the ion pairs have similar conformations. In the case of the optimized structure of the $[C_4mim][PhBF_3]$ ion pair, the BF_3 group in the $[PhBF_3]^-$ anion interacts with the hydrogen on the C_2 position of the imidazolium cation, which is the same as with the $[C_4mim][BF_4]$ ion pair. The phenyl ring is in a skew position to the plane of the imidazolium ring. The only exceptions are the $[C_4mim][ArBF_3]$ ion pairs whose anions have -F or -OMe in ortho-substitutes. In the optimized structures for the $[C_4mim][o\text{-}FC_6H_4BF_3]$ and $[C_4mim][o\text{-}OMeC_6H_4BF_3]$ ion pairs, phenyl rings turn to the plane of the imidazolium cation. The steric hindrance between the butyl

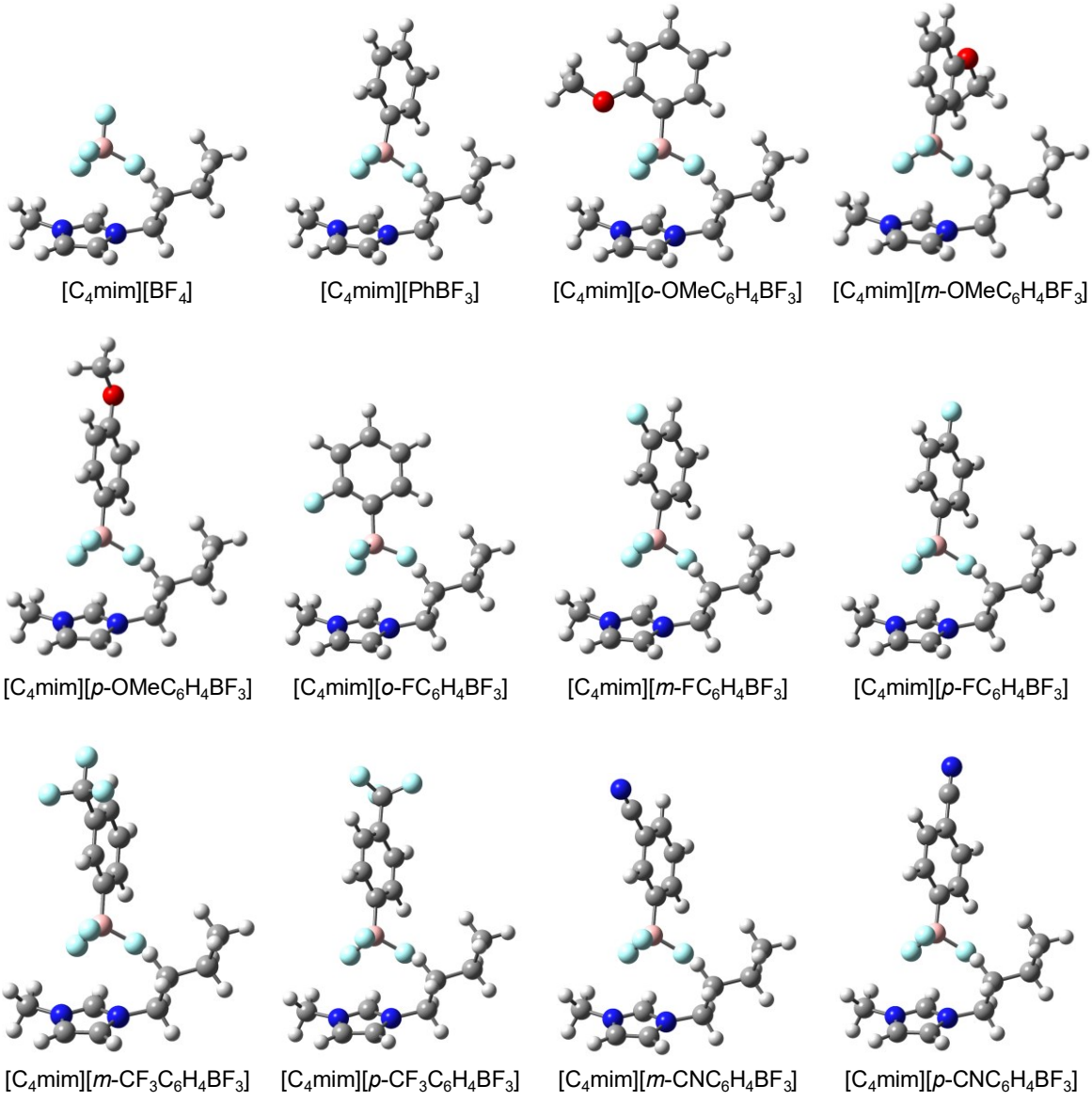

Figure 3-9. Optimized structures of ion pairs consisting of $[C_4mim]^+$ and aryltrifluoroborates with various substituents. The geometries were optimized at the HF/6-311G(d,p) level.

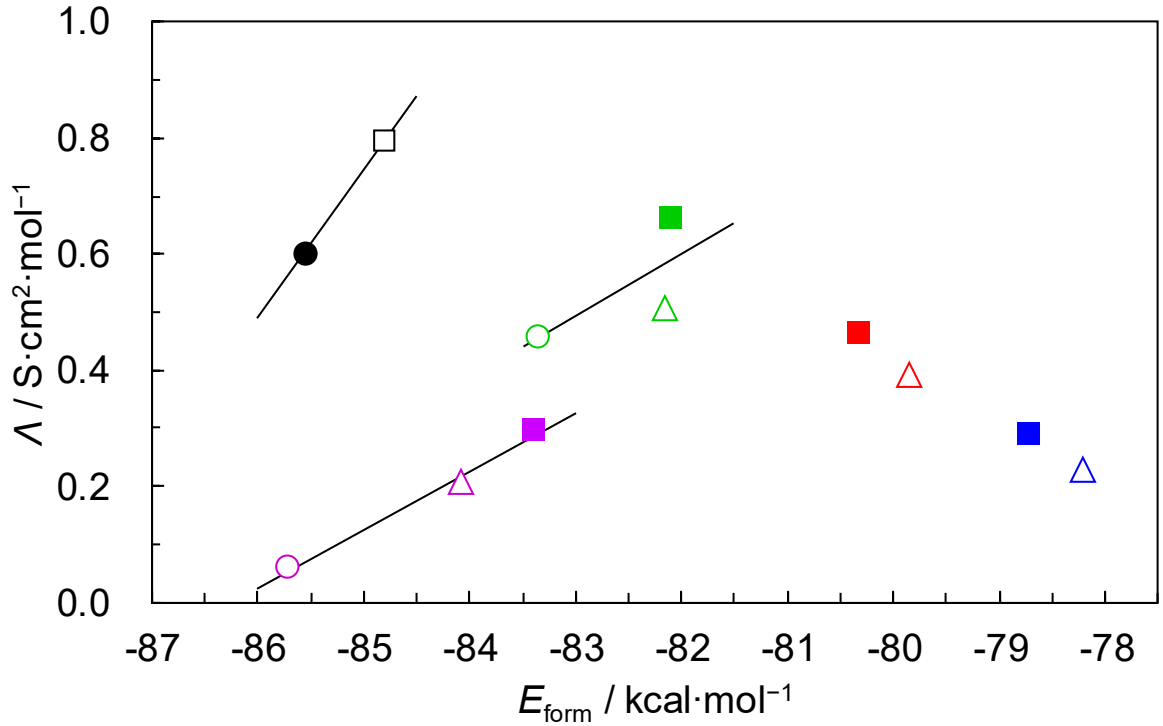

Figure 3-10. Correlations between equivalent conductivity and formation energy of the ionic pairs for (○) [C4mim][*o*-OMeC6H4BF3], (■) [C4mim][*m*-OMeC6H4BF3], (△) [C4mim][*p*-OMeC6H4BF3], (○) [C4mim][*o*-FC6H4BF3], (■) [C4mim][*m*-FC6H4BF3], (△) [C4mim][*p*-FC6H4BF3], (■) [C4mim][*m*-CF3C6H4BF3], (△) [C4mim][*p*-CF3C6H4BF3], (■) [C4mim][*m*-CNC6H4BF3], (△) [C4mim][*p*-CNC6H4BF3], (●) [C4mim][PhBF3], and (□) [C4mim][BF4]. Equivalent conductivity was measured at 303 K. E_{form} was given by Gaussian 09 program at the MP2/6-311G(d,p) level.

group on the cation and the ortho-located group on the anion is the cause of the different conformation of the optimized structures.

To discuss the substituent effects on the interaction between the cation and anion species, the author calculated the stabilization energies (E_{form}) for the ionic pairs.[39, 43, 50] The magnitude of the stabilization energy calculated for an ion pair expresses the degree of interionic interaction between the anion and cation species. The E_{form} calculated for the [C4mim][ArBF3] ion pairs ranges from −78.2 to −85.9 kcal·mol^{-1} (Table 3-1). The ion pairs composed of anions having electron withdrawing groups, such as -F, -CF3, or -CN, have smaller interionic interactions compared with those having the electron donating -OMe. Introduction of the electron donating -OMe group to the phenyl ring increases the negative charge on the -BF3 group, which is also confirmed by the electrostatic potential fitting to the [OMeC6H4BF3]$^-$ anions. Figure 3-10 shows the correlation between equivalent conductivity, Λ, and E_{form} for the [C4mim][ArBF3] RTILs. The Λ increased proportionally with the decrease of E_{form} unless the substituents were CF3 and CN. For reference, [C4mim][BF4], which has a smaller E_{form} than [C4mim][PhBF3], displays a higher equivalent conductivity. The author could not observe a clear correlation between Λ and E_{form} when a -CF3 or -CN group, which are favorable electron withdrawing groups to decrease the interionic interaction, is contained in the anion. One

plausible reason is that the steric hindrance is caused by their relatively large ionic volumes and inflexible structure prevents ionic mobility. It should also be consider that a tetramer-like ion pair, such as ([C_4mim]$_2$[ArBF_3])[ArBF_3], may temporarily form in the RTILs due to the non-negligible interaction between the lone pairs on the -CF_3 and -CN groups and the adjacent cations. In fact, the similar oligomerizing nature is seen in other protic or aprotic RTILs with some hydrogen bonding sites, and the formation is indicated by the molecular orbital calculation and the molecular dynamics simulation.[105-108] If a huge ion pair is partially generated in a short period of time, the fluidity and ionic conductivity would decrease despite having a favorable E_{form}.

3.3.4. Electrochemical measurements

The electrochemically stable potential range, called the electrochemical window (EW),[100] is used to discuss the electrochemical properties of solvents. Electrochemical stability of the [C_4mim][ArBF_3] RTILs was examined by linear sweep voltammetry (Figure 3-11). Table 3-4 summarizes the values for the cathodic limiting potential (E_c), anodic limiting potential (E_a), and EW estimated from the voltammograms. In commonly used RTILs, except Lewis acid-base type RTILs,[109] E_c and E_a are derived from the decomposition of cationic and anionic species,

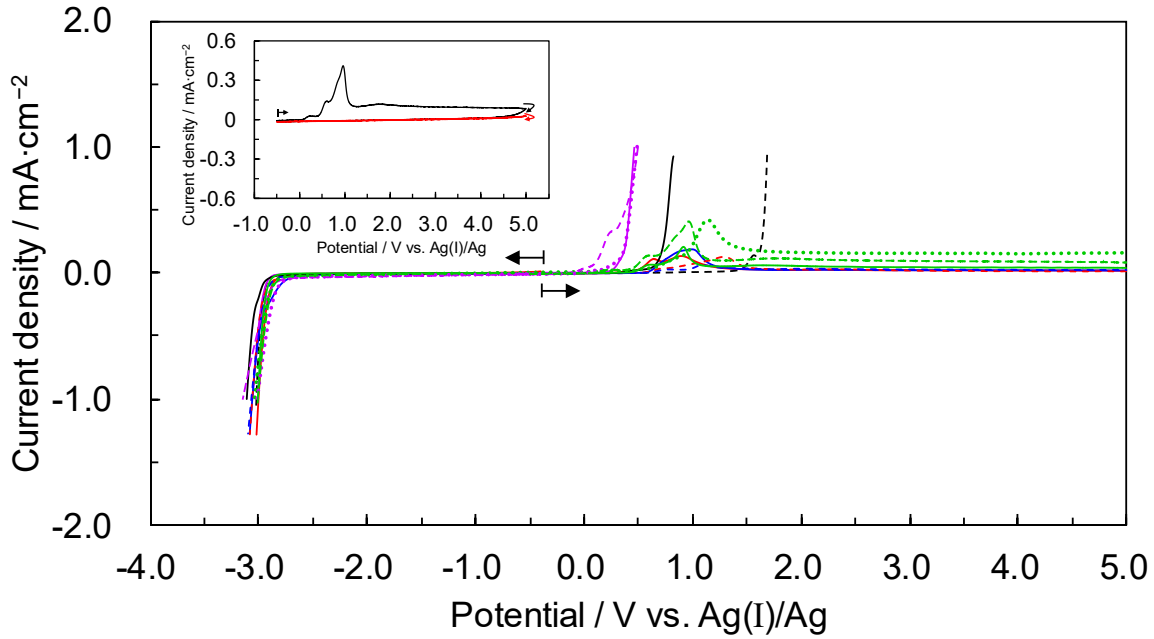

Figure 3-11. Liner sweep voltammograms recorded at a glassy carbon electrode in (····) [C_4mim][*o*-OMe$C_6H_4BF_3$], (—) [C_4mim][*m*-OMe$C_6H_4BF_3$], (---) [C_4mim][*p*-OMe$C_6H_4BF_3$], (····) [C_4mim][*o*-F$C_6H_4BF_3$], (—) [C_4mim][*m*-F$C_6H_4BF_3$], (---) [C_4mim][*p*-F$C_6H_4BF_3$], (—) [C_4mim][*m*-$CF_3C_6H_4BF_3$], (---) [C_4mim][*p*-$CF_3C_6H_4BF_3$], (—) [C_4mim][*m*-CN$C_6H_4BF_3$], (---) [C_4mim][*p*-CN$C_6H_4BF_3$], (—) [C_4mim][PhBF_3], and (---) [C_4mim][BF_4] at 298 K. The scan rate was 10 mV·s^{-1}. (inset) Cyclic voltammograms recorded at a glassy carbon electrode in [C_4mim][*p*-F$C_6H_4BF_3$] at 298 K. (—) First cycle and (—) second cycle. The scan rate was 10 mV·s^{-1}.

respectively. All the [C4mim][ArBF3] RTILs have a similar E_c of −2.80 to −2.96 V vs. Ag(I)/Ag due to the same cationic species. In the anodic region, by contrast, they show different E_a values, suggesting that the decomposition behavior strongly depends on the anionic species. The EWs of the RTILs composed of $[ArBF_3]^-$ with an -OMe group (3.18–3.28 V) are narrower than that of non-substitutive [C4mim][PhBF3] (3.65 V), but ones with electron withdrawing groups, such as -F, -CF3, and -CN, display a wider EW of 3.49–4.06 V. Introducing an electron donating group, such as -OMe, to the $[ArBF_3]^-$ leads to the formation of an easily oxidized electron-rich anion. Furthermore, the electron withdrawing group can cause an anion to become electron poor resulting in the electrochemical oxidation-resistant RTILs. HOMO energy levels of ion pairs obtained by *ab initio* calculations support these results. The data for comparison are given in Table 3-4. Unfortunately, all the [C4mim][ArBF3] RTILs prepared in this study show narrower EWs than [C4mim][BF4] due to the electron-rich phenyl group on the $[ArBF_3]^-$.

Table 3-4. Cathodic and anodic limits, electrochemical windows, and HOMO energy for the [C4mim][ArBF3] RTILs

RTILs	E_c[a] / V vs. Ag(I)/Ag	E_a[b] / V vs. Ag(I)/Ag	EW[c] / V	E_{HOMO}[d] / eV
[C4mim][BF4]	−2.99	1.65	4.64	−9.93
[C4mim][PhBF3]	−3.04	0.745	3.78	−4.94
[C4mim][*o*-OMeC6H4BF3]	−2.89	0.392	3.28	−4.56
[C4mim][*m*-OMeC6H4BF3]	−2.94	0.327	3.26	−4.67
[C4mim][*p*-OMeC6H4BF3]	−2.96	0.218	3.18	−4.55
[C4mim][*o*-FC6H4BF3]	−2.94	1.04	3.98	−5.20
[C4mim][*m*-FC6H4BF3]	−2.80	0.799	3.60	−5.24
[C4mim][*p*-FC6H4BF3]	−2.92	0.855	3.78	−5.09
[C4mim][*m*-CF3C6H4BF3]	−2.88	0.611	3.49	−5.58
[C4mim][*p*-CF3C6H4BF3]	−2.91	1.15	4.06	−5.71
[C4mim][*m*-CNC6H4BF3]	−2.81	0.734	3.54	−5.78
[C4mim][*p*-CNC6H4BF3]	−2.90	1.09[e]	3.99	−5.74

[a]Cathodic limiting potential at the cut-off current density of −0.3 mA·cm^{-2}. [b]Anodic limiting potential at the cut-off current density of 0.3 mA·cm^{-2}. [c]Electrochemical window (EW) = E_a – E_c. [d]HOMO energy of anion given by the Gaussian 09 program at the HF/6-311G(d,p) level. [e]Potential at the maximum current density.

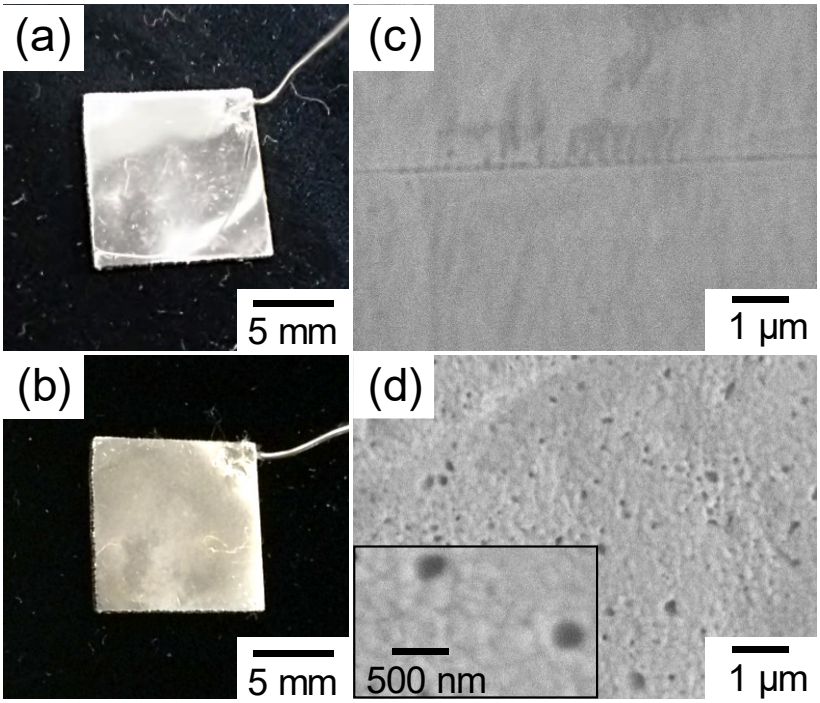

Figure 3-12. (a, b) Pictures and (c, d) FE-SEM images of a Pt electrode (a and c) before and (b and d) after voltammetric experiments.

Surprisingly, unique anodic decomposition behaviors appeared at approximately 0.8 V vs. Ag(I)/Ag in the $[C_4mim][ArBF_3]$ RTILs with electron withdrawing groups. For instance, in $[C_4mim][p\text{-}FC_6H_4BF_3]$, the cyclic voltammogram obtained at the potential range of open circuit potential to 5.0 V changes greatly after two or more cycles (Figure 3-11 (inset)). Analogous electrochemical behavior has already been reported in the RTIL electrolytes with $[N(CN)_2]^-$, $[C(CN)_3]^-$, or $[B(CN)_4]^-$.[110-113] Further investigation was conducted by visual inspection and SEM observation of the electrodes before and after the voltammetry to determine the cause for these results. After the anodic potential sweep, the color of the Pt electrode changed slightly from metallic bright to light yellow (Figure 3-12a and b), and the SEM images reveal the uniform formation of an unknown membrane on the electrode (Figure 3-12c and d). EDX analysis of the deposit indicated that the major components are C, N, and F, and the atomic ratio of the components are greatly different from the ratio in the $[C_4mim][p\text{-}FC_6H_4BF_3]$. To characterize the ionic selectivity of the membrane, electrochemical experiments were performed using the three types of redox reagents, $[FeCp_2][BF_4]$ for cation redox, $FeCp_2$ for neutral redox, and $[C_2mim][FeCl_4]$ for anion redox. When the membrane-modified Pt electrode pretreated by the potential sweep was used as a working electrode, cyclic voltammograms in $[C_4mim][p\text{-}FC_6H_4BF_3]$ changed greatly with the added redox reagent species (Figure 3-13 and Table 3-5). A clear reversible behavior for all the redox reagents is given using a pristine Pt electrode. The peak current for the anion redox reagent, $[FeCl_4]^-$, is hardly observed at the

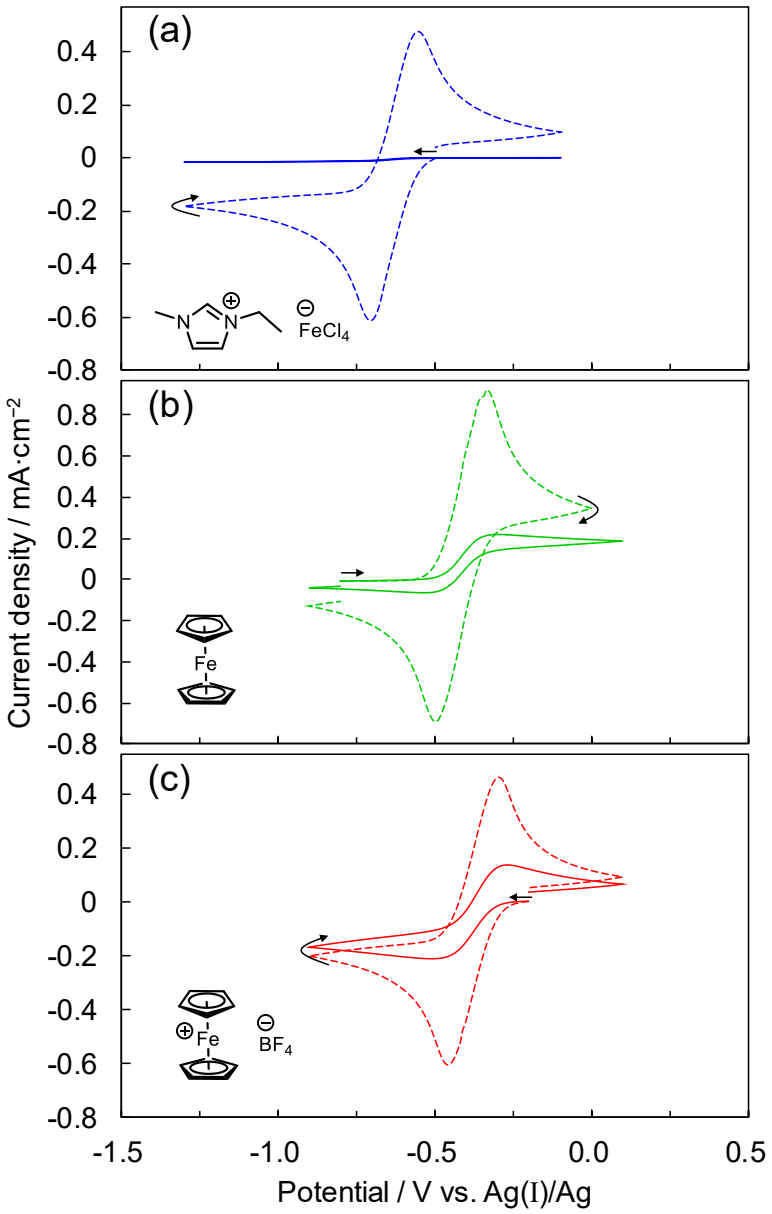

Figure 3-13. Cyclic voltammograms recorded at a (---) pristine Pt electrode or (—) membrane-modified Pt electrode in (a) 0.1 M [C_2mim][$FeCl_4$]/[C_4mim][*p*-$FC_6H_4BF_3$], (b) 0.1 M $FeCp_2$/[C_4mim][*p*-$FC_6H_4BF_3$], and (c) 0.1 M [$FeCp_2$][BF_4]/[C_4mim][*p*-$FC_6H_4BF_3$] at 298 K. The scan rate was 10 $mV \cdot s^{-1}$.

modified electrode; however, using the cation and neutral redox reagents, $[FeCp_2]^+$ and $FeCp_2$, gentle peak currents appear. These results indicate that the formed membrane works as an anion blocking layer. Still the formation mechanism is unknown, but electropolymerization of the $[ArBF_3]^-$ anion may occur on the electrode surface during the anodic potential sweep.[114] This unexpected anion blocking layer can possibly be used as a useful electrode coating for high voltage cathodes in future high-capacity Li-ion batteries to impede solvent decomposition.

Table 3-5. Summary of electrochemical analyses of three redox reagents on a pristine or membrane-modified Pt electrode[a]

Redox reagents	$D_{Pristine}$[b] / $cm^2 \cdot s^{-1}$	Pristine Pt		Membrane-modified Pt		$I_{membrane\text{-}modified}/I_{pristine}$
		I_{pc}[c] / $mA \cdot cm^{-2}$	I_{pa}[d] / $mA \cdot cm^{-2}$	I_{pc}[c] / $mA \cdot cm^{-2}$	I_{pa}[d] / $mA \cdot cm^{-2}$	
$[C_2mim][FeCl_4]$	5.20×10^{-8}	−0.612	0.476	−0.0106	0.00133	0.0173
$FeCp_2$	11.7×10^{-8}	−0.694	0.919	−0.0605	0.214	0.233
$[FeCp_2][BF_4]$	5.07×10^{-8}	−0.604	0.464	−0.201	0.131	0.333

[a]Prepared by the potential scan in $[C_4mim][p\text{-}FC_6H_4BF_3]$ at the potential range of −0.5 to 5.0 V vs. Ag(I)/Ag. [b]Diffusion coefficients of the redox reagents on the pristine Pt given by Randles–Sevcik equation at the scan rate of 10 $mV \cdot s^{-1}$, the redox reagent concentration of 0.1 M, and the I_{pc} for $[FeCl_4]^-$ and $[FeCp_2]^+$ or the I_{pa} for $FeCp_2$. [c]Cathodic peak current density. [d]Anodic peak current density.

3.4. Summary

A series of over 10 types of [C_4mim][$ArBF_3$] RTILs was successfully prepared by a simple, safe and non-hazardous chemical synthesis process. Their physicochemical properties varied with the substituents introduced on the phenyl group in $[ArBF_3]^-$. Notably, [C_4mim][*m*-$FC_6H_4BF_3$] showed favorable fluidity and more ionic conductivity than non-substitutive [C_4mim][$PhBF_3$]. A computational approach revealed that the interionic interaction between $[ArBF_3]^-$ and $[C_4mim]^+$ was closely associated with the transport properties, except for RTILs with $[ArBF_3]^-$ containing CF_3 and CN groups. In addition, if an electron withdrawing group was contained in the $[ArBF_3]^-$ anion, anomalous electrochemical behavior was recognized at the anodic limiting potential, which may correspond to the electropolymerization of the $[ArBF_3]^-$ anion. The formed membrane made an electrochemically active Pt electrode inactive to anionic species but not neutral and cationic ones.

3.5. Characterization data

Characterization of [C_4mim][$ArBF_3$] RTILs was performed in the same conditions and manner described in previous chapter.

1-Butyl-3-methylimidazolium (ortho-methoxyphenyl)trifluoroborate ([C_4mim][*o*-$OMeC_6H_4BF_3$]):

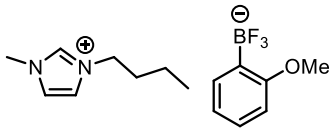

Colorless liquid. ^{1}H NMR (400 MHz, $CDCl_3$): σ 0.899 (t, 3H, $^3J_{HH}$ = 7.4 Hz), 1.27 (m, 2H, $^3J_{HH}$ = 7.7 Hz), 1.72 (m, 2H, $^3J_{HH}$ = 7.8 Hz), 3.75 (s, 3H), 3.84 (s, 3H), 4.02 (t, 2H, $^3J_{HH}$ = 7.6 Hz), 6.77 (d, 1H, $^3J_{HH}$ = 8.0 Hz), 6.84 (t, 1H, $^3J_{HH}$ = 7.2 Hz), 7.11 (d, 1H, $^3J_{HH}$ = 1.6 Hz), 7.15 (dt, 1H, $^3J_{HH}$ = 1.6 Hz, 7.7 Hz), 7.20 (d, 1H, $^3J_{HH}$ = 1.6 Hz), 7.54 (d, 1H, $^1J_{HH}$ = 6.8 Hz), 9.09 (s, 1H). ^{13}C NMR (100 MHz, $CDCl_3$): σ 13.3 (s), 19.3 (s), 31.9 (s), 36.3 (s), 49.8 (s), 55.1 (s), 109.9 (s), 113.8 (s), 120.6 (s), 121.9 (s), 123.5 (s), 129.4 (s), 136.8 (s), 159.4 (s). ^{19}F NMR (376 MHz, $CDCl_3$): σ −139.2 (s, 3F, B*F*$_3$). ^{11}B NMR (128 MHz, $CDCl_3$): σ 3.49 (s, *B*F_3). HRMS (FAB), *m*/*z*: calcd. for $C_{23}H_{37}N_4OBF_3^+$ 453.3007 $[M + [C_4mim]]^+$; found 453.3017. Elemental analysis calcd. for $C_{15}H_{22}N_2OBF_3$: C, 57.35; H, 7.06; N, 8.92; found: C, 56.61; H, 7.27; N, 8.75.

1-Butyl-3-methylimidazolium (meta-methoxyphenyl)trifluoroborate ([C$_4$mim][*m*-OMeC$_6$H$_4$BF$_3$]):

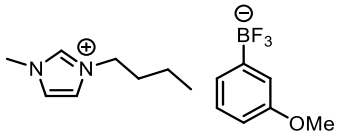

Colorless liquid. ^{1}H NMR (400 MHz, $CDCl_3$): σ 0.910 (t, 3H, $^3J_{HH}$ = 7.4 Hz), 1.27 (m, 2H, $^3J_{HH}$ = 7.7 Hz), 1.71 (m, 2H, $^3J_{HH}$ = 7.7 Hz), 3.77 (s, 3H), 3.78 (s, 3H), 3.97 (t, 2H, $^3J_{HH}$ = 7.4 Hz), 6.68–6.72 (m, 1H), 7.07 (t, 1H, $^3J_{HH}$ = 1.8 Hz), 7.12–7.15 (m, 4H), 8.77 (s, 1H). ^{13}C NMR (100 MHz, $CDCl_3$): σ 13.3 (s), 19.3 (s), 31.9 (s), 36.2 (s), 49.7 (s), 55.1 (s), 113.8 (s), 120.6 (s), 122.0 (s), 123.6 (s), 129.4 (s), 136.4 (s), 159.4 (s). ^{19}F NMR (376 MHz, $CDCl_3$): σ −141.5 (s, 3F, B*F*$_3$). ^{11}B NMR (128 MHz, $CDCl_3$): σ 3.47 (s, *B*F$_3$). HRMS (FAB), *m*/*z*: calcd. for $C_{23}H_{37}N_4OBF_3^+$ 453.3007 [M + [C$_4$mim]]$^+$; found 453.3012. Elemental analysis calcd. for $C_{15}H_{22}N_2OBF_3$: C, 57.35; H, 7.06; N, 8.92; found: C, 56.59; H, 7.17; N, 8.78.

1-Butyl-3-methylimidazolium (para-methoxyphenyl)trifluoroborate ([C$_4$mim][*p*-OMeC$_6$H$_4$BF$_3$]):

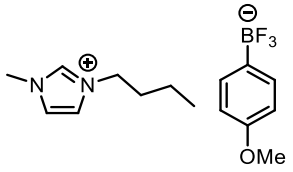

Colorless liquid. ^{1}H NMR (400 MHz, $CDCl_3$): σ 0.911 (t, 3H, $^3J_{HH}$ = 7.2 Hz), 1.27 (m, 2H, $^3J_{HH}$ = 7.7 Hz), 1.71 (m, 2H, $^3J_{HH}$ = 7.7 Hz), 3.76 (s, 3H), 3.79 (s, 3H), 3.98 (t, 2H, $^3J_{HH}$ = 7.4 Hz), 6.78 (d, 2H, $^3J_{HH}$ = 8.4 Hz), 7.08 (t, 1H, $^3J_{HH}$ = 1.8 Hz), 7.13 (t, 1H, $^3J_{HH}$ = 1.8 Hz), 7.49 (d, 2H, $^3J_{HH}$ = 8.4 Hz), 8.85 (s, 1H). ^{13}C NMR (100 MHz, $CDCl_3$): σ 13.3 (s), 19.3 (s), 31.9 (s), 36.2 (s), 49.7 (s), 55.0 (s), 113.8 (s), 122.1 (s), 123.6 (s), 129.4 (s), 136.5 (s), 159.4 (s). ^{19}F NMR (376 MHz, $CDCl_3$): σ −140.6 (s, 3F, B*F*$_3$). ^{11}B NMR (128 MHz, $CDCl_3$): σ 3.71 (s, *B*F$_3$). HRMS (FAB), *m*/*z*: calcd. for $C_{23}H_{37}N_4OBF_3^+$ 453.3007 [M + [C$_4$mim]]$^+$; found 453.3013. Elemental analysis calcd. for $C_{15}H_{22}N_2OBF_3$: C, 57.35; H, 7.06; N, 8.92; found: C, 56.47; H, 7.12; N, 8.87.

1-Butyl-3-methylimidazolium (ortho-fluorophenyl)trifluoroborate ([C$_4$mim][*o*-FC$_6$H$_4$BF$_3$]):

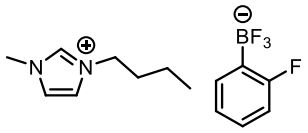

Colorless liquid. ^{1}H NMR (400 MHz, $CDCl_3$): σ 0.854 (t, 3H, $^3J_{HH}$ = 7.3 Hz), 1.22 (m, 2H, $^3J_{HH}$ = 7.6 Hz), 1.69 (m, 2H, $^3J_{HH}$ = 7.5 Hz), 3.79 (s, 3H), 4.00 (t, 2H, $^3J_{HH}$ = 7.6 Hz), 6.80 (t, 1H,

$^{3}J_{HH}$ = 8.7 Hz), 6.97 (t, 1H, $^{3}J_{HH}$ = 7.1 Hz), 7.08–7.14 (m, 1H), 7.18 (t, 1H, $^{3}J_{HH}$ = 1.8 Hz), 7.23 (t, 1H, $^{3}J_{HH}$ = 1.6 Hz), 7.51 (t, 1H, $^{3}J_{HH}$ = 6.9 Hz), 8.83 (s, 1H). ^{13}C NMR (100 MHz, $CDCl_3$): σ 13.2 (s), 19.2 (s), 31.8 (s), 36.0 (s), 49.5 (s), 114.0 (d, $^{2}J_{CF}$ = 24.8 Hz), 121.9 (s), 123.0 (s), 123.5 (s), 128.0 (d, $^{3}J_{CF}$ = 7.6 Hz), 134.1 (d, $^{3}J_{CF}$ = 12.4 Hz), 136.4 (s), 166.0 (d, $^{1}J_{CF}$ = 237.4 Hz). ^{19}F NMR (376 MHz, $CDCl_3$): σ −139.4 (s, 3F, B*F*$_3$), −109.7 (s, 1F, *o*-*F*C_6H_4). ^{11}B NMR (128 MHz, $CDCl_3$): σ 3.02 (s, *B*F_3). HRMS (FAB), *m*/*z*: calcd. for $C_{22}H_{34}N_4BF_4^+$ 441.2807 [M + [C_4mim]]$^+$; found 441.2819. Elemental analysis calcd. for $C_{14}H_{19}N_2BF_4$: C, 55.66; H, 6.34; N, 9.27; found: C, 55.21; H, 6.43; N, 9.15.

1-Butyl-3-methylimidazolium (meta-fluorophenyl)trifluoroborate ([C_4mim][*m*-$FC_6H_4BF_3$]):

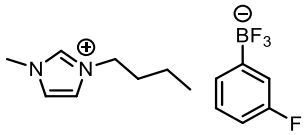

Colorless liquid. ^{1}H NMR (400 MHz, $CDCl_3$): σ 0.926 (t, 3H, $^{3}J_{HH}$ = 7.6 Hz), 1.30 (m, 2H, $^{3}J_{HH}$ = 7.7 Hz), 1.76 (m, 2H, $^{3}J_{HH}$ = 7.6 Hz), 3.85 (s, 3H), 4.04 (t, 2H, $^{3}J_{HH}$ = 7.4 Hz), 6.79–6.84 (m, 1H), 7.10 (t, 1H, $^{3}J_{HH}$ = 2.0 Hz), 7.14 (t, 1H, $^{3}J_{HH}$ = 1.8 Hz), 7.16–7.21 (m, 2H), 7.33 (d, 1H, $^{3}J_{HH}$ = 6.8 Hz), 8.95 (s, 1H). ^{13}C NMR (100 MHz, $CDCl_3$): σ 13.2 (s), 19.2 (s), 31.7 (s), 36.0 (s), 49.5 (s), 112.6 (d, $^{2}J_{CF}$ = 21.0 Hz), 117.3 (d, $^{2}J_{CF}$ = 17.1 Hz), 121.9 (s), 123.4 (s), 126.8 (s), 128.6 (d, $^{3}J_{CF}$ = 6.7 Hz), 136.1 (s), 162.6 (d, $^{1}J_{CF}$ = 242.2 Hz). ^{19}F NMR (376 MHz, $CDCl_3$): σ −142.0 (s, 3F, B*F*$_3$), −116.9 (s, 1F, *m*-*F*C_6H_4). ^{11}B NMR (128 MHz, $CDCl_3$): σ 3.31 (s, *B*F_3). HRMS (FAB), *m*/*z*: calcd. for $C_{22}H_{34}N_4BF_4^+$ 441.2807 [M + [C_4mim]]$^+$; found 441.2815. Elemental analysis calcd. for $C_{14}H_{19}N_2BF_4$: C, 55.66; H, 6.34; N, 9.27; found: C, 55.04; H, 6.39; N, 9.15.

1-Butyl-3-methylimidazolium (para-fluorophenyl)trifluoroborate ([C_4mim][*p*-$FC_6H_4BF_3$]):

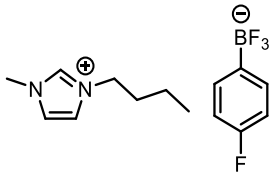

Colorless liquid. ^{1}H NMR (400 MHz, $CDCl_3$): σ 0.849 (t, 3H, $^{3}J_{HH}$ = 7.2 Hz), 1.19 (m, 2H, $^{3}J_{HH}$ = 7.7 Hz), 1.63 (m, 2H, $^{3}J_{HH}$ = 7.6 Hz), 3.69 (s, 3H), 3.89 (t, 2H, $^{3}J_{HH}$ = 7.6 Hz), 6.85 (t, 2H, $^{3}J_{HH}$ = 9.2 Hz), 7.08 (t, 1H, $^{3}J_{HH}$ = 1.8 Hz), 7.12 (t, 1H, $^{3}J_{HH}$ = 2.0 Hz), 7.46 (t, 2H, $^{3}J_{HH}$ = 7.2 Hz), 8.62 (s, 1H). ^{13}C NMR (100 MHz, $CDCl_3$): σ 13.2 (s), 19.2 (s), 31.7 (s), 35.9 (s), 49.4 (s), 113.5 (d, $^{2}J_{CF}$ = 19.2 Hz), 121.9 (s), 123.4 (s), 132.8 (d, $^{3}J_{CF}$ = 5.7 Hz), 136.1 (s), 161.9 (d, $^{1}J_{CF}$ = 242.4 Hz). ^{19}F NMR (376 MHz, $CDCl_3$): σ −141.1 (s, 3F, B*F*$_3$), −118.5 (s, 1F, *p*-*F*C_6H_4). ^{11}B

NMR (128 MHz, $CDCl_3$): σ 3.68 (s, BF_3). HRMS (FAB), *m*/*z*: calcd. for $C_{22}H_{34}N_4BF_4^+$ 441.2807 [M + [C_4mim]]$^+$; found 441.2811. Elemental analysis calcd. for $C_{14}H_{19}N_2BF_4$: C, 55.66; H, 6.34; N, 9.27; found: C, 54.99; H, 6.36; N, 9.13.

1-Butyl-3-methylimidazolium (meta-trifluoromethylphenyl)trifluoroborate ([C_4mim][*m*-$CF_3C_6H_4BF_3$]):

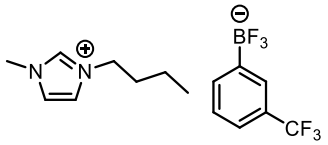

Colorless liquid. ^{1}H NMR (400 MHz, $CDCl_3$): σ 0.874 (t, 3H, $^3J_{HH}$ = 7.6 Hz), 1.24 (m, 2H, $^3J_{HH}$ = 7.7 Hz), 1.70 (m, 2H, $^3J_{HH}$ = 7.5 Hz), 3.80 (s, 3H), 3.99 (t, 2H, $^3J_{HH}$ = 7.6 Hz), 7.11 (t, 1H, $^3J_{HH}$ = 1.6 Hz), 7.15 (t, 1H, $^3J_{HH}$ = 1.8 Hz), 7.31 (t, 1H, $^3J_{HH}$ = 7.4 Hz), 7.39 (d, 1H, $^3J_{HH}$ = 7.6 Hz), 7.72–7.75 (m, 2H), 8.84 (s, 1H). ^{13}C NMR (100 MHz, $CDCl_3$): σ 13.2 (s), 19.2 (s), 31.7 (s), 36.1 (s), 49.7 (s), 121.8 (s), 122.7 (s), 123.3 (s), 125.0 (q, $^1J_{CF}$ = 270.8 Hz, CF_3), 127.2 (s), 127.7 (s), 128.7 (q, $^2J_{CF}$ = 30.5 Hz), 134.9 (s), 136.4 (s). ^{19}F NMR (376 MHz, $CDCl_3$): σ −142.2 (s, 3F, BF_3), −63.1 (s, 3F, CF_3). ^{11}B NMR (128 MHz, $CDCl_3$): σ 3.31 (s, BF_3). HRMS (FAB), *m*/*z*: calcd. for $C_{23}H_{34}N_4BF_6^+$ 491.2775 [M + [C_4mim]]$^+$; found 491.2782. Elemental analysis calcd. for $C_{15}H_{19}N_2BF_6$: C, 51.16; H, 5.44; N, 7.96; found: C, 50.40; H, 5.62; N, 7.88.

1-Butyl-3-methylimidazolium (para-trifluoromethylphenyl)trifluoroborate ([C_4mim][*p*-$CF_3C_6H_4BF_3$]):

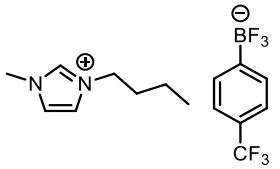

Colorless liquid. ^{1}H NMR (400 MHz, $CDCl_3$): σ 0.871 (t, 3H, $^3J_{HH}$ = 7.4 Hz), 1.18–1.28 (m, 2H), 1.64–1.73 (m, 2H), 3.79 (m, 3H), 3.95–3.99 (m, 2H), 7.09 (d, 1H, $^3J_{HH}$ = 1.2 Hz), 7.13 (d, 1H, $^3J_{HH}$ = 1.6 Hz), 7.44 (d, 2H, $^3J_{HH}$ = 8.0 Hz), 7.64 (d, 2H, $^3J_{HH}$ = 8.0 Hz), 8.82 (d, 1H, $^3J_{HH}$ = 6.0 Hz). ^{13}C NMR (100 MHz, $CDCl_3$): σ 13.2 (s), 19.2 (s), 31.7 (s), 36.1 (s), 49.6 (s), 121.8 (s), 123.3 (s), 123.5 (s), 124.8 (q, $^1J_{CF}$ = 270.3 Hz), 128.0 (q, $^2J_{CF}$ = 31.5 Hz), 131.5 (s), 136.3 (s). ^{19}F NMR (376 MHz, $CDCl_3$): σ −142.3 (s, 3F, BF_3), −63.1 (s, 3F, CF_3). ^{11}B NMR (128 MHz, $CDCl_3$): σ 3.44 (s, BF_3). HRMS (FAB), *m*/*z*: calcd. for $C_{23}H_{34}N_4BF_6^+$ 491.2775 [M + [C_4mim]]$^+$; found 491.2783. Elemental analysis calcd. for $C_{15}H_{19}N_2BF_6$: C, 51.16; H, 5.44; N, 7.96; found: C, 50.58; H, 5.53; N, 7.93.

1-Butyl-3-methylimidazolium (meta-cyanophenyl)trifluoroborate ([C$_4$mim][*m*-CNC$_6$H$_4$BF$_3$]):

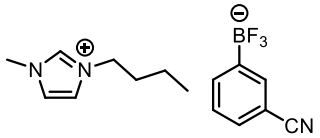

Colorless liquid. ^{1}H NMR (400 MHz, $CDCl_3$): σ 0.889 (t, 3H, $^3J_{HH}$ = 7.3 Hz), 1.27 (m, 2H, $^3J_{HH}$ = 7.6 Hz), 1.74 (m, 2H, $^3J_{HH}$ = 7.6 Hz), 3.86 (s, 3H), 4.06 (t, 2H, $^3J_{HH}$ = 7.3 Hz), 7.21 (m, 1H), 7.24 (m, 1H), 7.30 (t, 1H, $^3J_{HH}$ = 7.8 Hz), 7.42 (d, 1H, $^3J_{HH}$ = 7.3 Hz), 7.77−7.79 (m, 2H), 8.91 (s, 1H). ^{13}C NMR (100 MHz, $CDCl_3$): σ 13.2 (s), 19.3 (s), 31.8 (s), 36.2 (s), 49.8 (s), 110.3 (s), 120.4 (s), 121.9 (s), 123.4 (s), 127.6 (s), 129.7 (s), 135.1 (s), 136.0 (s), 136.4 (s). ^{19}F NMR (376 MHz, $CDCl_3$): σ −142.5 (s, 3F, B*F*$_3$). ^{11}B NMR (128 MHz, $CDCl_3$): σ 3.27 (s, *B*F$_3$). HRMS (FAB), *m*/*z*: calcd. for $C_{23}H_{34}N_5BF_3^+$ 448.2854 [M + [C$_4$mim]]$^+$; found 448.2843. Elemental analysis calcd. for $C_{15}H_{19}N_3BF_3$: C, 58.28; H, 6.20; N, 13.59; found: C, 57.53; H, 6.42; N, 13.49.

1-Butyl-3-methylimidazolium (para-cyanolphenyl)trifluoroborate ([C$_4$mim][*p*-CNC$_6$H$_4$BF$_3$]):

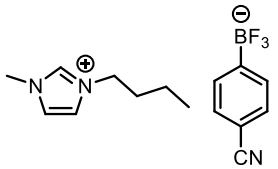

Colorless liquid. ^{1}H NMR (400 MHz, $CDCl_3$): σ 0.890 (t, 3H, $^3J_{HH}$ = 7.3 Hz), 1.27 (m, 2H, $^3J_{HH}$ = 7.1 Hz), 1.74 (m, 2H, $^3J_{HH}$ = 7.3 Hz), 3.85 (s, 3H), 4.03−4.09 (m, 2H), 7.18 (s, 1H), 7.21 (s, 1H), 7.48 (d, 2H, $^3J_{HH}$ = 7.8 Hz), 7.64 (d, 2H, $^3J_{HH}$ = 7.8 Hz), 8.92 (s, 1H). ^{13}C NMR (100 MHz, $CDCl_3$): σ 13.2 (s), 19.2 (s), 31.7 (s), 36.1 (s), 49.6 (s), 109.1 (s), 120.1 (s), 122.0 (s), 123.4 (s), 130.5 (s), 131.9 (s), 136.2 (s). ^{19}F NMR (376 MHz, $CDCl_3$): σ −142.6 (s, 3F, B*F*$_3$). ^{11}B NMR (128 MHz, $CDCl_3$): σ 3.25 (s, *B*F$_3$). HRMS (FAB), *m*/*z*: calcd. for $C_{23}H_{34}N_5BF_3^+$ 448.2854 [M + [C$_4$mim]]$^+$; found 448.2855. Elemental analysis calcd. for $C_{15}H_{19}N_3BF_3$: C, 58.28; H, 6.20; N, 13.59; found: C, 57.40; H, 6.38; N, 13.49.

Conclusions

In this investigation, many types of the novel salts with $[ArBF_3]^-$ were designed and prepared for creating unforeknown low temperature molten salts and RTILs. To use $[ArBF_3]^-$ anion as liquid salt constituent, the first systematical studies on the impact of anionic structure on RTIL's features were achieved. In addition, it was revealed that the several salts with $[ArBF_3]^-$ anion exhibit the unique electrochemical behaviors attributing to the redox reaction for cation or anion. Chapter 1 detailed the synthetic method, property evaluation, and electrochemical application of alkali metal aryltrifluoroborates. A number of $[ArBF_3]^-$ were designed in order to perform the systematical investigations of novel alkali metal salts. The author successfully synthesized approximately 40 kinds of novel alkali metal salts by safe and easy preparation method, and their thermal properties were elucidated. These salts showed lower melting points than those of simple inorganic alkali metal halides due to the larger entropy of anion and the weaker interactions between the alkali metal cations and the $[ArBF_3]^-$ anions. K[*m*-$OEtC_6H_4BF_3$] which can reduce K(I) to K(0) was obtained as a low temperature molten salt electrolyte. In Chapter 2, truly new RTILs with $[PhBF_3]^-$, which is the simplest $[ArBF_3]^-$ were depicted. The author investigated closely the physicochemical properties of $[PhBF_3]^-$-based RTILs with seven types of organic cations. The $[PhBF_3]^-$-based RTILs showed favorable transport properties, e.g., fluidity and ionic conductivity, despite a rigid and bulky aromatic ring on the anion. The remarkable relationship between transport properties and the molecular volume of the RTILs were observed. The electrochemical stability for $[PhBF_3]^-$-based salts were examined. It was revealed that the cation's structure determined the transport and electrochemical properties for the $[PhBF_3]^-$-based RTILs. Chapter 3 described the physicochemical and electrochemical properties of the $[C_4mim][ArBF_3]$ RTILs. A series of $[C_4mim][ArBF_3]$ RTILs with various substituents introduced on the phenyl moiety on the anion were successfully prepared and examined. Various properties were exhibited by modification of anion's structure but the transport properties scarcely depended on the ionic pair volume although the pair volume dependency of the RTIL properties is recognized in Chapter 2. To discuss the electronic and structural effect of groups on anion, the quantum chemical calculations were performed evaluating the cation-anion interaction and HOMO energy level of anion. Unexpected anion selective layer was formed on a Pt electrode by the electrochemical oxidation of $[ArBF_3]^-$ anion with the electron withdrawing groups. These results obtained in this work will provide the novel guidelines of molten salts and RTILs synthesis to existing synthetic strategies. The author firmly considers that the findings lead to further development of molten salt, ionic liquid and electrochemical technology.

References

1. Ito, Y.; Nohira, T., *Electrochim. Acta* **2000,** *45*, 2611–2622.
2. Lovering, D. G., *Molten Salt Technology*. Springer Science+Business Media: New York, 1982.
3. Nohira, T.; Yasuda, K.; Ito, Y., *Nat. Mater.* **2003,** *2*, 397–401.
4. Yasuda, K.; Nohira, T.; Kobayashi, K.; Kani, N.; Tsuda, T.; Hagiwara, R., *Energy Technol.* **2013,** *1*, 245–252.
5. Murakami, T.; Nishikiori, T.; Nohira, T.; Ito, Y., *J. Am. Chem. Soc.* **2003,** *125*, 334–335.
6. Walden, P., Bull. Acad. Imper. Sci. St. Petersburg **1914,** 405–422.
7. Torimoto, T.; Tsuda, T.; Okazaki, K.; Kuwabata, S., *Adv. Mater.* **2010,** *22*, 1196–1221.
8. Kuwabata, S.; Tsuda, T.; Torimoto, T., *J. Phys. Chem. Lett.* **2010,** *1*, 3177–3188.
9. Le, M. L. P.; Tran, N. A.; Ngo, H. P. K.; Nguyen, T. G.; Tran, V. M., *J. Solution Chem.* **2015,** *44*, 2332–2343.
10. Forsyth, S. A.; Frohlich, U.; Goodrich, P.; Gunaratne, H. Q. N.; Hardacre, C.; McKeown, A.; Seddon, K. R., *New J. Chem.* **2010,** *34*, 723–731.
11. Deng, H.; Li, X.; Chu, Y.; He, J.; Cheng, J. P., *J. Org. Chem.* **2012,** *77*, 7291–7298.
12. Matsumoto, K.; Hagiwara, R.; Ito, Y., *J. Fluorine Chem.* **2002,** *115*, 133–135.
13. Sun, J.; Forsyth, M.; MacFarlane, D. R., *J. Phys. Chem. B* **1998,** *102*, 8858–8864.
14. Hagiwara, R.; Matsumoto, K.; Nakamori, Y.; Tsuda, T.; Ito, Y.; Matsumoto, H.; Momota, K., *J. Electrochem. Soc.* **2003,** *150*, D195–D199.
15. Tsuda, T.; Kondo, K.; Baba, M.; Suwa, S.; Ikeda, Y.; Sakamoto, T.; Seino, S.; Yoshida, H.; Ozaki, M.; Imanishi, A.; Kuwabata, S., *Electrochim. Acta* **2013,** *100*, 285–292.
16. Yoshii, K.; Yamaji, K.; Tsuda, T.; Tsunashima, K.; Yoshida, H.; Ozaki, M.; Kuwabata, S., *J. Phys. Chem. B* **2013,** *117*, 15051–15059.
17. Aupoix, A.; Pégot, B.; Vo-Thanh, G., *Tetrahedron* **2010,** *66*, 1352–1356.
18. Baba, K.; Ono, H.; Itoh, E.; Itoh, S.; Noda, K.; Usui, T.; Ishihara, K.; Inamo, M.; Takagi, H. D.; Asano, T., *Chem. Eur. J.* **2006,** *12*, 5328–5333.
19. Crowhurst, L.; Mawdsley, P. R.; Perez-Arlandis, J. M.; Salter, P. A.; Welton, T., *Phys. Chem. Chem. Phys.* **2003,** *5*, 2790–2794.
20. Conte, L.; Gambaretto, G.; Caporiccio, G.; Alessandrini, F.; Passerini, S., *J. Fluorine Chem.* **2004,** *125*, 243–252.
21. Armand, M. Process for synthesis of sulfonylimides. US5072040A, December 10, 1991.
22. Foropoulos, J.; DesMarteau, D. D., *Inorg. Chem.* **1984,** *23*, 3720–3723.
23. Lennox, A. J.; Lloyd-Jones, G. C., *Angew. Chem. Int. Ed.* **2012,** *51*, 9385–9388.
24. Hagiwara, R.; Tamaki, K.; Kubota, K.; Goto, T.; Nohira, T., *J. Chem. Eng. Data* **2008,** *53*, 355–358.
25. Kubota, K.; Nohira, T.; Goto, T.; Hagiwara, R., *Electrochem. Commun.* **2008,** *10*, 1886–

1888.
26. Kubota, K.; Tamaki, K.; Nohira, T.; Goto, T.; Hagiwara, R., *Electrochim. Acta* **2010,** *55*, 1113–1119.
27. Kubota, K.; Nohira, T.; Hagiwara, R., *J. Chem. Eng. Data* **2010,** *55*, 2546–2549.
28. Kubota, K.; Nohira, T.; Hagiwara, R., *J. Chem. Eng. Data* **2010,** *55*, 3142–3146.
29. Van Artsdalen, E. R.; Yaffe, I. S., *J. Phys. Chem.* **1955,** *59*, 118–127.
30. Kubota, K.; Nohira, T.; Goto, T.; Hagiwara, R., *J. Chem. Eng. Data* **2008,** *53*, 2144–2147.
31. Boyarchuk, T. P.; Khailova, E. G.; Cherginets, V. L., *Electrochim. Acta* **1993,** *38*, 1481–1485.
32. Masset, P.; Schoeffert, S.; Poinso, J. Y.; Poignet, J. C., *J. Electrochem. Soc.* **2005,** *152*, A405–A410.
33. Watarai, A.; Kubota, K.; Yamagata, M.; Goto, T.; Nohira, T.; Hagiwara, R.; Ui, K.; Kumagai, N., *J. Power Sources* **2008,** *183*, 724–729.
34. Tu, X.; Chu, Y.; Ma, C., *Ionics* **2009,** *16*, 81–84.
35. Li, G.; Lu, X.; Coyle, C. A.; Kim, J. Y.; Lemmon, J. P.; Sprenkle, V. L.; Yang, Z., *J. Power Sources* **2012,** *220*, 193–198.
36. Frisch, M. J.; Trucks, G. W.; Schlegel, H. B.; Scuseria, G. E.; Robb, M. A.; Cheeseman, J. R.; Scalmani, G.; Barone, V.; Mennucci, B.; Petersson, G. A.; Nakatsuji, H.; Caricato, M.; Li, X.; Hratchian, H. P.; Izmaylov, A. F.; Bloino, J.; Zheng, G.; Sonnenberg, J. L.; Hada, M.; Ehara, M.; Toyota, K.; Fukuda, R.; Hasegawa, J.; Ishida, M.; Nakajima, T.; Honda, Y.; Kitao, O.; Nakai, H.; Vreven, T.; Montgomery Jr., J. A.; Peralta, J. E.; Ogliaro, F.; Bearpark, M. J.; Heyd, J.; Brothers, E. N.; Kudin, K. N.; Staroverov, V. N.; Kobayashi, R.; Normand, J.; Raghavachari, K.; Rendell, A. P.; Burant, J. C.; Iyengar, S. S.; Tomasi, J.; Cossi, M.; Rega, N.; Millam, N. J.; Klene, M.; Knox, J. E.; Cross, J. B.; Bakken, V.; Adamo, C.; Jaramillo, J.; Gomperts, R.; Stratmann, R. E.; Yazyev, O.; Austin, A. J.; Cammi, R.; Pomelli, C.; Ochterski, J. W.; Martin, R. L.; Morokuma, K.; Zakrzewski, V. G.; Voth, G. A.; Salvador, P.; Dannenberg, J. J.; Dapprich, S.; Daniels, A. D.; Farkas, Ö.; Foresman, J. B.; Ortiz, J. V.; Cioslowski, J.; Fox, D. J. *Gaussian 09*, Gaussian, Inc.: Wallingford, CT, 2009.
37. Møller, C.; Plesset, M. S., *Phys. Rev.* **1934,** *46*, 618–622.
38. Head-Gordon, M.; Pople, J. A.; Frisch, M. J., *Chem. Phys. Lett.* **1988,** *153*, 503–506.
39. Tsuzuki, S.; Tokuda, H.; Hayamizu, K.; Watanabe, M., *J. Phys. Chem. B* **2005,** *109*, 16474–16481.
40. Tsuzuki, S.; Hayamizu, K.; Seki, S.; Ohno, Y.; Kobayashi, Y.; Miyashiro, H., *J. Phys. Chem. B* **2008,** *112*, 9914–9920.
41. Ransil, B. J., *J. Chem. Phys.* **1961,** *34*, 2109–2118.
42. Boys, S. F.; Bernardi, F., *Mol. Phys.* **1970,** *19*, 553–566.
43. Tsuzuki, S.; Kubota, K.; Matsumoto, H., *J. Phys. Chem. B* **2013,** *117*, 16212–16218.
44. Finze, M.; Bernhardt, E.; Willner, H.; Lehmann, C. W., *J. Am. Chem. Soc.* **2005,** *127*,

10712–10722.
45. Bredig, M. A.; Bronstein, H. R.; Smith, W. T., *J. Am. Chem. Soc.* **1955,** *77*, 1454–1458.
46. Ginnings, D. C.; Phipps, T. E., *J. Am. Chem. Soc.* **1930,** *52*, 1340–1345.
47. Gramstad, T.; Haszeldine, R. N., *J. Chem. Soc.* **1956,** 173–180.
48. Amini, M.; Fincham, D.; Hockney, R. W., *J. Phys. C: Solid State Phys.* **1979,** *12*, 4707–4720.
49. Furukawa, K., *Discuss. Faraday Soc.* **1961,** *32*, 53–62.
50. Tsuzuki, S.; Umecky, T.; Matsumoto, H.; Shinoda, W.; Mikami, M., *J. Phys. Chem. B* **2010,** *114*, 11390–11396.
51. Bernard, U. L.; Izgorodina, E. I.; MacFarlane, D. R., *J. Phys. Chem. C* **2010,** *114*, 20472–20478.
52. Serp, J.; Konings, R. J. M.; Malmbeck, R.; Rebizant, J.; Scheppler, C.; Glatz, J. P., *J. Electroanal. Chem.* **2004,** *561*, 143–148.
53. Masset, P.; Konings, R. J. M.; Malmbeck, R.; Serp, J.; Glatz, J.-P., *J. Nucl. Mater.* **2005,** *344*, 173–179.
54. Bermejo, M. R.; Gómez, J.; Martínez, A. M.; Barrado, E.; Castrillejo, Y., *Electrochim. Acta* **2008,** *53*, 5106–5112.
55. Sangster, J.; Bale, C. W., *J. Phase Equilib. Diffus.* **1998,** *19*, 67–69.
56. Bard, A. J.; Faulkner, L. R., *Electrochemical Methods: Fundamentals and Applications*. 2nd ed.; John Wiley & Sons, Inc.: New York, 2001.
57. Konishi, H.; Nohira, T.; Ito, Y., *Electrochim. Acta* **2002,** *47*, 3533–3539.
58. Eliaz, N.; Sridhar, T. M.; Gileadi, E., *Electrochim. Acta* **2005,** *50*, 2893–2904.
59. Xu, L.; Guan, H.; Li, D.; Wang, L., *Proc. Inst. Mech. Eng., Part J* **2015,** *229*, 1372–1378.
60. Wibowo, R.; Aldous, L.; Jacobs, R. M. J.; Manan, N. S. A.; Compton, R. G., *Chem. Phys. Lett.* **2011,** *509*, 72–76.
61. Jorné, J.; Tobias, C. W., *J. Appl. Electrochem.* **1975,** *5*, 279–290.
62. Lu, W.; Baranski, A. S., *J. Electroanal. Chem.* **1992,** *335*, 105–122.
63. Oliveira, R. A.; Silva, R. O.; Molander, G. A.; Menezes, P. H., *Magn. Reson. Chem.* **2009,** *47*, 873–878.
64. Tsuda, T.; Hussey, C. L., Electrochemistry of Room-Temperature Ionic Liquids and Melts. In *Modern Aspects of Electrochemistry*, White, R. E., Ed. Springer Science+Business Media: New York, 2009; Vol. 45, pp 63–174.
65. Ohno, H., *Electrochemical Aspects of Ionic Liquids*. John Wiley & Sons, Inc.: New Jersey, 2005.
66. Hagiwara, R.; Ito, Y., *J. Fluorine Chem.* **2000,** *105*, 221–227.
67. Itoh, T., *Chem. Rev.* **2017,** *117*, 10567–10607.
68. Handy, S. T., *Ionic Liquids - Classes and Properties*. InTech: Croatia, 2011.
69. Brennecke, J. F.; Maginn, E. J., *AlChE J.* **2001,** *47*, 2384–2389.
70. Buzzeo, M. C.; Evans, R. G.; Compton, R. G., *ChemPhysChem* **2004,** *5*, 1106–1120.

71. Ueki, T.; Watanabe, M., *Macromolecules* **2008,** *41*, 3739–3749.
72. Kirchner, B., *Topics in Current Chemistry; Ionic Liquids*. Springer Science+Business Media: Heidelberg, Berlin, 2009.
73. Chen, Z. J.; Lee, J. M., *J. Phys. Chem. B* **2014,** *118*, 2712–2718.
74. Chen, Z. J.; Xi, H. W.; Lim, K. H.; Lee, J. M., *Angew. Chem. Int. Ed.* **2013,** *52*, 13392–13396.
75. Zhou, Z.-B.; Matsumoto, H.; Tatsumi, K., *Chem. Eur. J.* **2006,** *12*, 2196–2212.
76. Zhao, D.; Fei, Z.; Ohlin, C. A.; Laurenczy, G.; Dyson, P. J., *Chem. Commun.* **2004,** 2500–2501.
77. Zhou, Z.-B.; Takeda, M.; Ue, M., *J. Fluorine Chem.* **2004,** *125*, 471–476.
78. Zhou, Z.-B.; Matsumoto, H.; Tatsumi, K., *ChemPhysChem* **2005,** *6*, 1324–1332.
79. Matsumoto, H.; Sakaebe, H.; Tatsumi, K., *J. Power Sources* **2005,** *146*, 45–50.
80. Zhou, Z.-B.; Matsumoto, H.; Tatsumi, K., *Chem. Eur. J.* **2004,** *10*, 6581–6591.
81. Zhou, Z.-B.; Matsumoto, H.; Tatsumi, K., *Chem. Eur. J.* **2005,** *11*, 752–766.
82. Zhou, Z.-B.; Matsumoto, H.; Tatsumi, K., *Chem. Lett.* **2004,** *33*, 680–681.
83. Zhou, Z.-B.; Matsumoto, H.; Tatsumi, K., *Chem. Lett.* **2004,** *33*, 886–887.
84. Rablen, P. R.; Hartwig, J. F., *J. Am. Chem. Soc.* **1996,** *118*, 4648–4653.
85. Huddleston, J. G.; Visser, A. E.; Reichert, W. M.; Willauer, H. D.; Broker, G. A.; Rogers, R. D., *Green Chem.* **2001,** *3*, 156–164.
86. Nishikawa, K.; Wang, S.; Katayanagi, H.; Hayashi, S.; Hamaguchi, H. O.; Koga, Y.; Tozaki, K., *J. Phys. Chem. B* **2007,** *111*, 4894–4900.
87. Shimizu, Y.; Fujii, K.; Imanari, M.; Nishikawa, K., *J. Phys. Chem. B* **2015,** *119*, 12552–12560.
88. Jenkins, H. D. B.; Roobottom, H. K.; Passmore, J.; Glasser, L., *Inorg. Chem.* **1999,** *38*, 3609–3620.
89. Krossing, I.; Slattery, J. M.; Daguenet, C.; Dyson, P. J.; Oleinikova, A.; Weingartner, H., *J. Am. Chem. Soc.* **2006,** *128*, 13427–13434.
90. Slattery, J. M.; Daguenet, C.; Dyson, P. J.; Schubert, T. J.; Krossing, I., *Angew. Chem. Int. Ed.* **2007,** *46*, 5384–5388.
91. Tsuzuki, S., *ChemPhysChem* **2012,** *13*, 1664–1670.
92. Tokuda, H.; Ishii, K.; Susan, M. A.; Tsuzuki, S.; Hayamizu, K.; Watanabe, M., *J. Phys. Chem. B* **2006,** *110*, 2833–2839.
93. Angell, C. A.; Xu, W.; Yoshizawa, M.; Hayashi, A.; Belieres, J.-P.; Lucas, P.; Videa, M., Physical Chemistry of Ionic Liquids, Inorganic and Organic, Protic and Aprotic. In *Electrochemical Aspects of Ionic Liquids*, Ohno, H., Ed. a John Wiley & Sons, Inc.: New Jersey, 2005; pp 5–26.
94. Angell, C. A., *J. Phys. Chem.* **1964,** *68*, 1917–1929.
95. Moynihan, C. T.; Angell, C. A., *J. Phys. Chem.* **1970,** *74*, 736–742.
96. Chen, P.-Y.; Hussey, C. L., *Electrochim. Acta* **2004,** *49*, 5125–5138.

97. Nishi, N.; Hashimoto, A.; Minami, E.; Sakka, T., *Phys. Chem. Chem. Phys.* **2015,** *17*, 5219–5226.
98. Tokuda, H.; Hayamizu, K.; Ishii, K.; Susan, M. A. B. H.; Watanabe, M., *J. Phys. Chem. B* **2004,** *108*, 16593–16600.
99. Xu, W.; Cooper, E. I.; Angell, C. A., *J. Phys. Chem. B* **2003,** *107*, 6170–6178.
100. Matsumoto, H., Electrochemical Windows of Room-Temperature Ionic Liquids. In *Electrochemical Aspects of Ionic Liquids*, Ohno, H., Ed. John Wiley & Sons, Inc.: New Jersey, 2005; pp 35–54.
101. Hussey, C. L., The Electrochemistry of Room-Temperature Haloaluminate Molten Salts. In *Chemistry of Nonaqueous Solutions*, Mamantov, G.; Popov, A. I., Eds. VCH Publishers: New York, 1994; pp 227–275.
102. Iwasaki, K.; Yoshii, K.; Tsuda, T.; Kuwabata, S., *J. Mol. Liq.* **2017,** *246*, 236–243.
103. Blanksby, S. J.; Ellison, G. B., *Acc. Chem. Res.* **2003,** *36*, 255–263.
104. Dean, J. A., Properties of Atoms, Radicals, and Bonds. In *Lange's Handbook of Chemistry*, fifteenth ed.; McGraw-Hill, Inc.: USA, 1998; pp 4.1–4.84.
105. Carlson, P. J.; Bose, S.; Armstrong, D. W.; Hawkins, T.; Gordon, M. S.; Petrich, J. W., *J. Phys. Chem. B* **2012,** *116*, 503–512.
106. Fumino, K.; Peppel, T.; Geppert-Rybczynska, M.; Zaitsau, D. H.; Lehmann, J. K.; Verevkin, S. P.; Kockerling, M.; Ludwig, R., *Phys. Chem. Chem. Phys.* **2011,** *13*, 14064–14075.
107. Peppel, T.; Roth, C.; Fumino, K.; Paschek, D.; Kockerling, M.; Ludwig, R., *Angew. Chem. Int. Ed.* **2011,** *50*, 6661–6665.
108. Kempter, V.; Kirchner, B., *J. Mol. Struct.* **2010,** *972*, 22–34.
109. Tsuda, T.; Stafford, G. R.; Hussey, C. L., *J. Electrochem. Soc.* **2017,** *164*, H5007–H5017.
110. MacFarlane, D. R.; Forsyth, S. A.; Golding, J.; Deacon, G. B., *Green Chem.* **2002,** *4*, 444–448.
111. MacFarlane, D. R.; Golding, J.; Forsyth, S.; Forsyth, M.; Deacon, G. B., *Chem. Commun.* **2001,** 1430–1431.
112. Yoshida, Y.; Muroi, K.; Otsuka, A.; Saito, G.; Takahashi, M.; Yoko, T., *Inorg. Chem.* **2004,** *43*, 1458–1462.
113. Seki, S.; Serizawa, N.; Hayamizu, K.; Tsuzuki, S.; Umebayashi, Y.; Takei, K.; Miyashiro, H., *J. Electrochem. Soc.* **2012,** *159*, A967–A971.
114. Yang, X.; Kirsch, J.; Zhang, Y.; Fergus, J.; Simonian, A., J. Electrochem. Soc. 2014, 161, E3036–E3041.

Acknowledgements

The author would like to express his greatest gratitude to Prof. Susumu Kuwabata at Department of Applied Chemistry, Graduate School of Engineering, Osaka University who provided carefully considered feedback, kind suggestions, valuable comments, and encouragement throughout this work. The author would like to thank to Prof. Nobuhito Imanaka and Prof. Ken-ichi Machida at Department of Applied Chemistry, Graduate School of Engineering, Osaka University for their careful reviews and beneficial comments. The author also wishes to make a grateful acknowledgement to Associate Prof. Tetsuya Tsuda at Department of Applied Chemistry, Graduate School of Engineering, Osaka University who provided continuous discussion, kind guidance, and helpful suggestion throughout this work. The author would like show his deeply appreciation to Dr. Seiji Tsuzuki at Research Center for Computational Design of Advanced Functional Materials, National Institute of Advanced Industrial Science and Technology for his valuable discussion and guidance for the computational simulations throughout this thesis. The author is grateful to Cross-Appointment Associate Prof. Hajime Matsumoto at Department of Energy and Environment, Research Institute of Electrochemical Energy, National Institute of Advanced Industrial Science and Technology who gives fruitful advices and kind encouragement. The author would like to thank Assistant Prof. Taro Uematsu at Department of Applied Chemistry, Graduate School of Engineering, Osaka University for his helpful comments. The author would like to appreciate Ms. Michiko Ebukuro, secretary of Applied Electrochemistry Laboratory, for her grateful help throughout life in the laboratory. The author is grateful to Dr. Eiko Mochizuki, Dr. Kazuki Yoshii, and Dr. Hiro Minamimoto for their intelligent comments and sincere encouragements. The author is also grateful to all members of Applied Electrochemistry Laboratory for their warm support and invaluable memories. The author gratefully appreciates Fostering Program of Human Resources in Chemistry from the Japan Chemical Industry Association for their scholarship supports. The author would also like to express his sincere gratitude to his father, Kenichi Iwasaki, his mother, Maki Iwasaki, his late paternal grandfather, Iwao Iwasaki, his paternal grandmother, Masako Iwasaki, his maternal grandfather, Tomoo Shimada, and his late maternal grandmother, Masayo Shimada, for their moral support and warm encouragements.

Kazuki Iwasaki
January 2018